Performance of Complex Snow Cover Descriptions in a Distributed Hydrological Model System and Simulation of Future Snow Cover and Discharge Characteristics

A Case Study for the High Alpine Terrain of the Berchtesgaden Alps

Dissertation zur Erlangung des Doktorgrades an der
Fakultät für Angewandte Informatik der
Universität Augsburg

vorgelegt von
Dipl.-Geogr. Michael Warscher
2014

Erstgutachter: Prof. Dr. Harald Kunstmann
Zweitgutachter: Prof. Dr. Jucundus Jacobeit
Externer Gutachter: Prof. Dr. Ulrich Strasser

Tag der mündlichen Prüfung: 30.07.2015

Acknowledgments

First of all, I would like to thank the core team of the project WaterNPB. These are my supervisors Harald Kunstmann and Ulrich Strasser, as well as Thomas Marke, Helmut Franz and my PhD-colleague Gabi Kraller without whom I would not have been able to accomplish this work. Many thanks also go to the extended project team including Daniela Kilian, Florian Hanzer, and Stefanie Vogl who all have made major contributions to this work.

I gratefully acknowledge the continuous support of Helmut Franz and Michael Vogel from the Berchtesgaden National Park Administration who initiated and financed this project.

I would like to thank all my colleagues at the IMK-IFU not only for their scientific and technical support but also for keeping the mood great. I want to express my special appreciations to Sven Wagner for being a perfect office companion, to Christof Lorenz for being the most reliable coffee break partner, to Christian Chwala for all the inspiring prework-ski-outings, to Joachim Fallmann for reactivating my long gone and forgotten passion for soccer, and to Ralf Sussmann for the numerous adventures in the mountains which helped to reset the brain from time to time, and more important to all of them for becoming friends.

A big thank you goes to the Mamas and Papas / Omas and Opas (Ingrid, Susi, Inge, Peter, Werner, Harry) who intensely supported me in general and especially by being the best and most flexible childcare service on the planet.

And last but by far the most important my gratitude goes to my beloved three ladies Iris, Nora und Johanna for showing me the real important things in life every day.

Contents

List of Figures

List of Tables

List of Symbols

A	$W \cdot m^{-2}$	advective energy flux by precipitation
C_{wind}	-	wind correction factor
D_{grav}	mm	gravitational deposition
D_{lim}	mm	upper deposition limit
$D_{max,grav}$	mm	maximum gravitational deposition
$D_{max,wind}$	mm	maximum wind-driven deposition
E	$W \cdot m^{-2}$	latent heat flux
F_{NB}	mm	mass flow in neighboring cell NB
G	$W \cdot m^{-2}$	ground / soil heat flux
M	mm	melting rate per time step
M_{ae}	$W \cdot m^{-2}$	energy surplus available for snowmelt
M_{in}	mm	incoming mass from neighboring cells
M_{out}	mm	total outflowing mass of a cell
P_{rain}	mm	liquid precipitation (rainfall)
P_{snow}	mm	solid precipitation (snowfall)
Q	$W \cdot m^{-2}$	short-wave and long-wave radiation balance
Q_0	-	scaling factor for baseflow
Q_B	mm	baseflow
S	mm	(re)sublimation rate per time step
SVF_{dir}	-	directed sky view factor
SWE	mm	snow water equivalent
T	K	air temperature
$T_{0,m}$	K	lower temperature limit for snowmelt
$T_{R/S}$	K	temperature for 50 % snowfall fraction
T_s	K	snow surface temperature
T_{trans}	K	temperature transition range for precipitation phase
W	$m \cdot s^{-1}$	wind speed

Ψ	m	hydraulic head
Θ	$m^3 \cdot m^{-3}$	water content
c_0	$mm \cdot K^{-1} \cdot d^{-1}$	temperature-dependent ablation factor
c_{lw}	$J \cdot kg^{-1} \cdot K^{-1}$	specific heat capacity of liquid water
c_m	$J \cdot g^{-1}$	latent heat of melting
c_{sw}	$J \cdot kg^{-1} \cdot K^{-1}$	specific heat capacity of ice
c_s	$J \cdot g^{-1}$	latent heat of sublimation
d_r	m^{-1}	drainage density
e	-	elevation factor
e_l	$mbar$	water vapor partial pressure at measurement level
e_l	$mbar$	water vapor saturation pressure at the snow surface
f_{NB}	-	draining fraction for neighboring cell NB
$f_{erosion}$	-	erosion factor
h_{GW}	m	groundwater table
$h_{geo,0}$	m	geodetic altitude of the soil surface
i	$^\circ\,(deg)$	local inclination
$i_{erosion}$	$^\circ\,(deg)$	lower inclination limit for snow erosion
i_{lim}	$^\circ\,(deg)$	upper inclination limit for deposition of sliding snow
k	$m \cdot s^{-1}$	hydraulic conductivity
k_B	m	outflow constant for baseflow
k_D	-	recession constant for direct flow
k_I	-	recession constant for interflow
k_s	$m \cdot s^{-1}$	saturated hydraulic conductivity
k_{rec}	-	recession parameter for saturated hydraulic conductivity
p_{snow}	-	fraction of snow in total precipitation
q	$m \cdot s^{-1}$	specific water flux
q_{ifl}	mm	interflow
t	$s/h/d$	time
z	m	vertical coordinate / depth

Abbreviations and Acronyms

AMUNDSEN	Alpine Multiscale Numerical Distributed Simulation Engine
AR4	Fourth Assessment Report of the IPCC
CDF	Cumulative distribution function
DEM	Digital elevation model
DWD	Deutscher Wetterdienst / German Weather Service
EB	Energy balance
ECHAM	GCM ECHAM - ECMWF / MPI Hamburg
ESCIMO	Energy Balance Snow Cover Integrated Model
GCM	General circulation / global climate model
HABITALP	Project "Alpine Habitat Diversity"
HM	Hydrological model
IDL	Interactive Data Language
IDW	Inverse distance weighting
IPCC	Intergovernmental Panel on Climate Change
IUCN	International Union for Conservation of Nature
LAI	Leaf area index
Landsat ETM+	Landsat Enhanced Thematic Mapper
LWZ	Lawinenwarnzentrale Bayern / Bavarian avalanche warning service
NASA	National Aeronautics and Space Administration
NDSI	Normalized Difference Snow Index
NPV	Nationalparkverwaltung Berchtesgaden / Administration Berchtesgaden National Park
NS	Nash-Sutcliffe coefficient

OpenMP	Open Multi-Processing
QM	Quantile mapping
RCM	Regional circulation / regional climate model
SRES	Special Report on Emission Scenarios
SVF	Sky view factor
SWE	Snow water equivalent
TI	Temperature index
UNESCO	United Nations Educational, Scientific and Cultural Organization
WRF	Weather Research and Forecasting Model

Abstract

The water balance in high Alpine regions in its full complexity is so far insufficiently understood. Large altitudinal gradients, a strong variability of meteorological variables in time and space, complex hydrogeological settings, and heterogeneous snow cover dynamics result in high uncertainties in the quantification of the water flux and storage terms. In this study, the deterministic model system WaSiM-ETH was complemented with physically based formulations to describe high Alpine specific snow processes. To enhance the reproduction of snow deposition and ablation processes, the new system calculates the energy balance of the snow cover considering the terrain-dependent radiation fluxes, as well as lateral snow transport processes induced by wind and gravitation. Test site for the study is the *Berchtesgaden National Park* (Bavarian Alps, Germany) which is characterized by extreme topography and climate conditions. The performance of the enhanced model system is analyzed and validated via measurements of the snow water equivalent and snow depths, satellite-based remote sensing data, and runoff gauge data. The model has proven to work stable in reproducing seasonal snow cover development over a wide range of elevations. It was able to reproduce the general spatial patterns and most of the fine scale details of snow coverage. With increasing snow model complexity, model efficiency (Nash-Sutcliffe coefficient) for simulated runoff increases from 0.57 to 0.68 in a high Alpine headwater catchment and from 0.62 to 0.64 in total. To assess possible impacts of a changing climate on the regional hydrology, the optimized model system was forced with dynamically downscaled climate simulations. Model results are compared between the control period 1971 - 2000 and the scenario period 2021 - 2050. The projected future precipitation characteristics are the main driver for the consequent changes in the regional hydrology. Mean snow cover duration decreases significantly (-19 d/year), whereas the absolute changes in seasonal snowmelt and runoff amounts are projected to remain relatively small.

Summary

The water balance in high Alpine regions in its full complexity is so far insufficiently understood. Large altitudinal gradients, a strong variability of meteorological variables in time and space, complex hydrogeological settings, unquantified lateral snow transport processes and heterogeneous snow cover dynamics result in high uncertainties in the quantification of the water flux and storage terms. A method to investigate and quantify these processes and terms is the application of distributed hydrological model systems. Modeling hydrological processes in such complex regions is a major challenge because of the mentioned large heterogeneities on different spatial and temporal scales. Additionally, the measurement networks that are necessary to develop, run and validate the models are usually more limited the more complex the terrain gets. Exactly opposing to this trend, the need for a dense station network rises with terrain complexity. On top of that, many hydrological processes are still not included in state of the art model systems, e.g. small scale snow cover dynamics including lateral transport. To enable reasonable and robust hydrological model results in complex mountainous terrain, the deterministic hydrological model WaSiM-ETH is complemented with physically based formulations to describe high Alpine specific snow processes within this study. The integration of the new snow module is done to improve the modeling of water fluxes influenced by the dynamics of the snow cover, which strongly affect the water cycle in high Alpine regions. To enhance the reproduction of snow deposition and ablation processes, the new approach calculates the energy balance of the snow cover considering the terrain-dependent radiation fluxes, as well as lateral snow transport processes induced by wind and gravitation. Test site for the study is the *Berchtesgaden National Park* (Bavarian Alps, Germany) which is characterized by extreme topography and climate conditions. The mountain ranges cover an altitude from 607 to 2713 m a.s.l. About one quarter of the investigated catchment area, which comprises 433 km^2 in total, is terrain steeper than 35°. The catchment is equipped with a dense network

of meteorological stations which forms a solid base for the presented modeling study.

Runoff generation in Alpine regions is typically affected by snow processes. Snow accumulation, storage, redistribution, and ablation control the availability of water. In this study, several robust algorithms and parameterizations describing snow processes in Alpine environments are implemented in a fully distributed, physically based hydrological model. Snow cover development is simulated using different methods from a simple temperature index approach, followed by an energy balance scheme, to additionally accounting for gravitational and wind-driven lateral snow redistribution. The performance of the model system in reproducing snow cover dynamics and the resulting discharge generation is analyzed and validated via measurements of the snow water equivalent (SWE) and snow depths, satellite-based remote sensing data, and runoff gauge data. The implemented approach for calculating the energy balance of the snow cover is validated using point measurements of SWE and snow depths. The model proves to work stable in reproducing seasonal snow cover development over a wide range of elevations. The model's performance on the catchment scale is evaluated using satellite-based remote sensing data. The model is able to reproduce the general pattern and most of the fine scale details of snow coverage. Spatial numerical performance indices show a satisfying result. With increasing snow model complexity, model efficiency (Nash-Sutcliffe coefficient) for simulated runoff increases from 0.57 to 0.68 in a high Alpine headwater catchment and from 0.62 to 0.64 in total. In particular, the results show that the introduction of the energy balance scheme reproduces daily fluctuations in the snowmelt rates that trace down to the channel stream. These daily cycles measured in snowmelt and the resulting runoff rates can not be reproduced by using the temperature index approach. In addition, accounting for lateral snow transport changes the seasonal distribution of modeled snowmelt amounts, which leads to a higher accuracy in modeling runoff characteristics.

To assess possible impacts of a changing climate on the hydrology and water balance of the region, dynamically downscaled climate simulations are used. The hydrological model system is forced with scenario data of a regional climate model (RCM: WRF 7 km, GCM: ECHAM5-MPI/OM T63/L32, Scenario A1B). Model results are

compared between the control period 1971 - 2000 and the future period 2021 - 2050. As the RCM model data has shown to be biased, it is corrected using a Quantile Mapping approach before forcing the hydrological model. A mean rise in air temperature of +0.94 $°C$ is projected for the catchment of the *Berchtesgadener Ache* that is accompanied by a slight increase in precipitation by +1.3 %. This increase in precipitation is valid only for rainfall (+6.1 %), whereas snowfall is projected to decrease significantly (-6.6 %). This change in precipitation characteristics is the main driver for the consequent changes in the regional hydrology which are quantified by using the enhanced hydrological model system. Snow cover duration decreases significantly (-19 d/year) depending on elevation. Consequently, annual snowmelt amounts are projected to decrease by -8.2 %. Mean annual evapotranspiration is projected to increase by +2.4 %. Despite this finding, the mean annual runoff is projected to increase as well by +2.8 % due to the increases in rainfall amounts. The absolute changes in seasonal snowmelt and runoff amounts and distributions are projected to remain relatively small. The frequency histogram of hourly discharge rates reveals a future intensification and accumulation of extreme runoff rates on both sides of the spectrum (low and high flow events) at the expense of mid-range river discharge rates.

Zusammenfassung

Der Wasserhaushalt in hochalpinen Einzugsgebieten ist in seiner gesamten Komplexität noch nicht verstanden. Extreme Topographie, heterogene klimatische Bedingungen und oft unbekannte hydrogeologische Gegebenheiten führen zu großen Unsicherheiten in der Quantifizierung der Wasserbilanz alpiner Einzugsgebiete. Der Wasserhaushalt im Gebiet des Nationalparks Berchtesgaden ist dabei stark geprägt von der Dynamik der Schneedecke und von karsthydrologischen Prozessen. Zur Quantifizierung der Wasserhaushaltskomponenten wird in dieser Studie das flächendifferenzierte, physikalisch-basierte Modellsystem WaSiM-ETH eingesetzt. Um die komplexen schneehydrologischen Prozesse der Region hochaufgelöst im Modell zu berücksichtigen, werden im Rahmen dieser Arbeit neue Methoden basierend auf einem hochgebirgsspezifischen Schneedeckenmodell in das hydrologische Modell implementiert. Die Entwicklung der Schneedecke hängt insbesondere im Gebirge stark von Strahlungsprozessen und lateralen Schneeumverteilungsmechanismen ab. Zur Verbesserung der Simulation der Schneedeckendynamik werden deshalb Verfahren angewandt und entwickelt, die zum einen die Energiebilanz der Schneedecke zur Bestimmung von Schmelze und (Re)-Sublimation berechnen, und zum anderen laterale Schneetransportprozesse berücksichtigen. Letztere setzen sich zusammen aus gravitativen Rutschungen, die explizit modelliert werden, und aus windgetriebener Umverteilung, die durch eine Geländeanalyse dynamisch parametrisiert wird. Das Testgebiet für die Studie ist der Nationalpark Berchtesgaden, der charakterisiert ist durch sein komplexes alpines Gelände und die daraus resultierenden stark heterogenen klimatischen Bedingungen. Das Gebiet umfasst einen Höhenbereich von 607 bis 2713 m ü. NN. Das untersuchte Einzugsgebiet der Berchtesgadener Ache (433 km^2) besteht aus Gelände, von dem etwa ein Viertel steiler als 35° ist. Das Gebiet ist mit einem dichten Netzwerk meteorologischer Stationen ausgestattet, das die Basis der hydrologischen Modellierung darstellt.

In alpinen Regionen ist die Abflussbildung und -dynamik stark von schneehydrologischen Prozessen geprägt. Schneeakkumulation, -speicherung, -umverteilung und -ablation steuern die saisonale Wasserverfügbarkeit. In dieser Studie werden mehrere robuste Methoden zur Beschreibung gebirgsspezifischer Schneeprozesse in ein voll flächendifferenziertes, physikalisch-basiertes Wasserhaushaltsmodell integriert. Die Schneedeckenentwicklung wird mit Methoden unterschiedlicher Komplexität simuliert, beginnend mit einem einfachen Temperatur-Index Verfahren, über die Energiebilanz-Methode, bis hin zur zusätzlichen Berücksichtigung lateraler Transportprozesse durch Gravitation und Wind. Das Energiebilanzverfahren und die Simulation von lateralen Schneetransportprozessen führt gegenüber der Temperatur-Index Methode zu großen Veränderungen in der modellierten räumlich-zeitlichen Schneedeckenverteilung und der folgenden Schneeschmelz- und Abflussdynamik. Die Schneebedeckungsdauer hängt dabei ab von Exposition, Höhe, Steilheit und dem umgebenden Gelände. Die Leistungsfähigkeit des Modells wird mit Messungen des Schneewasseräquivalents, satelliten-basierten Fernerkundungsdaten und Abflussmessungen analysiert und validiert. Die Energiebilanzmethode zur Bestimmung der Ablation wird mit Punktmessungen von Schneewasseräquivalent und Schneehöhe validiert. Es zeigt sich, dass das Modell die saisonale Schneedeckenentwicklung in verschiedenen Höhenlagen korrrekt darstellt. Um die Simulation der räumlichen Dynamik auf der Einzugsgebietsskala zu verfizieren werden Fernerkundungsdaten herangezogen. Das Modell reproduzierte sowohl großräumige Muster der Schneebedeckung, als auch eine Vielzahl an kleinskaligen Details. Numerische Performanzkriterien der räumlichen Variabilität zeigen zufriedenstellende Werte. Die Modelleffizienz (Nash-Sutcliffe-Koeffizient) für simulierten Abfluss steigt dabei mit zunehmender Modellkomplexität von 0.57 auf 0.68 in einem alpinen Kopfeinzugsgebiet und von 0.62 auf 0.64 für das Gesamtgebiet. Die Ergebnisse zeigen insbesondere, dass das Energiebilanzverfahren tägliche Abflussschwankungen reproduziert, die durch den Temperatur-Index Ansatz nicht wiedergegeben werden. Zudem führt die Simulation von lateralen Schneetransportprozessen zu einer jahreszeitlichen Umverteilung der modellierten Schneeschmelzmengen, was wiederum eine höhere Genauigkeit in der Abflusswiedergabe am Pegel zur Folge hat.

Um mögliche Einflüsse eines sich verändernden Klimas auf die regionale Hydrologie

und Wasserbilanz abzuschätzen, werden dynamisch verfeinerte Klimasimulationen herangezogen. Das optimierte hydrologische Modellsystem wird mit Szenariendaten eines regionalen Klimamodells angetrieben. Die Modellergebnisse werden zwischen der Kontrollperiode 1971-2000 und dem Szenariozeitraum 2021-2050 verglichen. Da die regionalen Klimasimulationen in den Niederschlagsmengen einen gerichteten Fehler aufweisen, werden sie mit Hilfe eines Quantile-Mapping Verfahrens und den vorhandenen Messdaten korrigiert. Das projizierte Klimawandelsignal für das Untersuchungsgebiet beläuft sich auf einen Anstieg der mittleren Lufttemperatur um +0.94 $°C$ und einen leichten Anstieg des Niederschlags um +1.3 %. Diese Zunahme des Niederschlags gilt allerdings nur für flüssigen Niederschlag (+6.1 %), wohingegen die Schneefallmengen signifikant abnehmen (-6.6 %). Diese Änderungen der Niederschlagsverteilung ist der Hauptfaktor für die Veränderungen im regionalen Wasserhaushalt. Die Schneebedeckungsdauer nimmt abhängig von der Höhenlage mit einem relativen Maximum in niedriger Höhe signifikant ab. Im Durchschnitt verkürzt sich die Zeit der Schneebedeckung um 19 Tage pro Jahr. Dementsprechend verringern sich auch die jährlichen Schneeschmelzmengen (-8.2 %). Trotz eines leichten Anstiegs der mittleren Verdunstung (+2.4 %) nimmt der mittlere Jahresabfluss aufgrund der erhöhten Niederschlagsmengen ebenso leicht zu (+2.8 %). Die absoluten Veränderungen in der saisonalen Verteilung von Schneeschmelze und Abfluss sind relativ gering. Eine Analyse der Häufigkeitsverteilung stündlicher Abflussraten zeigt eine Intensivierung und Häufung der Extremwerte auf beiden Seiten des Spektrums (Niedrig- und Hochwasser) auf Kosten mittlerer Abflussintensitäten.

1 Introduction

1.1 Motivation and Objectives

Runoff in Alpine regions is largely controlled by snow accumulation, storage, redistribution, and melting. Generally, the full complexity of the water balance in Alpine regions is only partially understood. High altitudinal gradients, a strong variability of meteorological variables in time and space, unquantified snow cover dynamics, complex and often unknown hydrogeological settings, and heterogeneous land use and soil formations result in high uncertainties in the quantification of the water balance and the prediction of discharge rates. These statements given by e.g. Klemes (1990) still hold even if there have been large research efforts to broaden the knowledge of Alpine water cycle processes. An effective tool to investigate these processes and quantify budgets of flux and storage terms are hydrological models. State of the art distributed hydrological models are still not capable of simulating all snow cover processes in complex terrain on the catchment scale. Especially lateral snow transport processes, interactions between vegetation and snow, radiation processes, and turbulent energy fluxes between open and snow covered areas are not yet fully understood and consequently not yet formulated for an operational application in hydrological models.

The area of the *Berchtesgaden National Park* is an ideal test case to study these processes as it is a catchment which is widely untouched by anthropogenic activities due to its state as a Biosphere reserve. On the other hand the catchment is equipped with an extraordinarily dense network of meteorological stations, in particular regarding the complex mountain terrain. This network is essential because it reduces model uncertainties introduced by limited knowledge of the meteorological forcing.

In addition to the scientific motivation, an objective of this work is to deliver a hydrological system and its results to the authority of the *Berchtesgaden National Park* that is optimized for simulating the regional hydrological characteristics. The climate change signal in the Alps is known to be more pronounced compared to the surrounding non-mountainous regions. Above that, due to the complex hydro-climatological setting and the special ecosystems, the Alpine regions react more sensitive to a changing climate. The long-term climate simulations carried out in the framework of this work are used in consecutive studies regarding ecosystems process studies, and in developing climate change adaptation strategies for the sensitive Alpine terrain.

This work will report about the investigation of the influence of different snow model approaches on modeling runoff dynamics in complex, high Alpine terrain. A state of the art distributed hydrological model system is enhanced using methods developed within a high-Alpine specific snow cover model. The optimized model system is forced by climate scenario simulations to assess potential impacts of a changing climate on the regional hydrology.

1.2 Scientific State of the Art and Innovation

Numerous model approaches exist to simulate snow processes on different scales. Depending on the purpose of the model application, e.g. runoff simulations, flood or avalanche forecasting, glacier mass balance, or small-scale snow physics studies, many snow models have been developed. The approaches can be classified in three different groups with numerous transitions in between: 1) index models (e.g. temperature, wind or radiation index), 2) models that determine the energy balance of a snow pack or surface, and 3) multi-layer schemes that additionally simulate

processes within the snow pack, e.g. stratification, metamorphism, and the accompanying energy and mass fluxes. Besides, there are formulations to account for additional processes like the interaction between snow and vegetation or for lateral snow transport. An overview of distributed snow modeling is given by Kirnbauer *et al.* (1994) and Fierz *et al.* (2003), of snow process modeling in different applications by Marsh (1999), and of snow process integration in land surface models by Pomeroy *et al.* (1998).

In distributed hydrological models, index approaches are most commonly used because of their simplicity, robustness, and efficiency. It is obvious, however, that they are not suitable tools to produce reasonable results for snow cover development in complex Alpine terrain on regional to local scales. Moreover, it is questionable to use temperature index methods in climate change impact assessment studies because of their high sensitivity to temperature change and their inability to adapt to changing systems. This holds particularly in high mountain regions with complex topography that are sensitive to climate change and, at the same time, subject to high uncertainties in climate projections. (Smiatek *et al.*, 2009, 2011; Laux *et al.*, 2011; Kobierska *et al.*, 2013)

Marks *et al.* (1999), Susong *et al.* (1999), Garen & Marks (2005), Lehning *et al.* (2006), Strasser (2008), and Liston & Elder (2006) present the application of distributed snow model systems that are suited for mountainous terrain and based on physical descriptions. Bavay *et al.* (2009) and Kobierska *et al.* (2013) use the model developed by Lehning *et al.* (2006) for future runoff simulations. Runoff formation is assessed by a conceptual approach in this case. Rigon *et al.* (2006) recently developed a distributed hydrological model system to simulate coupled mass and energy fluxes in Alpine catchments. They all show - with some limitations - successful applications of distributed snow models to Alpine catchments with high model resolution in time and space. Sophisticated snow modeling methods including lateral snow transport processes have not yet been used and studied in a physically based, fully distributed hydrological model on a regional scale. The study aims at establishing a distributed runoff model of this type that is, in addition, capable of performing scenario runs in the region.

Summarized, the innovative approaches in this work are:

- Integration of a high-Alpine specific energy balance calculation scheme for simulating snow melt and (re)sublimation into the hydrological model suite *Water Balance Simulation Model ETH (WaSiM-ETH)*
- Development and Implementation of algorithms to simulate lateral, gravitational transport of snow on steep slopes
- Development and implementation of a dynamic parameterization to account for wind-driven lateral redistribution of snow in complex Alpine terrain
- Climate change impact study including bias correction, specific model coupling and long-term simulations in a very fine spatial resolution using the enhanced, optimized hydrological model system

1.3 Project and Publications

The work was carried out in the framework of the project *WaterNPB* which was initiated and financed by the authority of the *Berchtesgaden National Park*. The project was split in the two subprojects *SnowNPB* and *KarstNPB*, each dealing with one of the two major hydrological research topics of the region, snow and karst processes, respectively. The new snow model approaches that were developed and implemented within this work have been officially released in WaSiM model version 9.06.02.

The core part of this work is published in:

- Warscher, M., Strasser, U., Kraller, G., Marke, T., Franz, H., Kunstmann, H.: Performance of complex snow cover descriptions in a distributed hydrological model system: A case study for the high Alpine terrain of the Berchtesgaden Alps. Water Resour. Res., doi:10.1002/wrcr.20219, 2013.

Other peer-reviewed publications originating from the project are:

- Marke, T., Strasser, U., Kraller, G., Warscher, M., Kunstmann, H., Franz, H., Vogel, M.: The Berchtesgaden National Park (Bavaria, Germany): a platform

for interdisciplinary catchment research. Env. Earth Sci., doi:10.1007/s12665-013-2317-z, 2013.

- Kraller, G., Warscher, M., Kunstmann, H., Vogl, S., Marke, T., Strasser, U.: Water balance estimation in high Alpine terrain by combining distributed modeling and a neural network approach (Berchtesgaden Alps, Germany). Hydrol. Earth Syst. Sci., doi:10.5194/hess-16-1969-2012, 2012.

1.4 Outline and Structure

Apart from this first introducing chapter and the summarizing final section, this work is structured in six main thematic chapters.

- Chapter two introduces the study area comprising the catchment of the *Berchtesgadener Ache* which includes the protected area of the *Berchtesgaden National Park*. Regional characteristics regarding climate, hydrology, geology, vegetation and general land use are pointed out.
- Chapter three describes the hydrological model system that is used as a central tool in the study including its most important modules and formulations. All input and validation data comprising hydrometeorological time series, spatial land use and hydrogeological classifications as well as remotely sensed datasets are presented. The configuration of the model setup, as well as calibration and validation procedures are explained in detail.
- Development and application of new methods for modeling the snow cover being the main focus of this work, the respective approaches are featured extensively in chapter four. The documentation comprises the existing snow model methods of the original hydrological model system and the implemented new methods for calculating snow melt and lateral redistribution. Besides the physical formulations and algorithms, a report of the technical implementation is given here.
- Chapter five presents the evaluation of the the new snow model approaches. The model performance is investigated using measurements and by comparison to the original snow model methods. Point measurements of snow depths

and snow water equivalent, as well as spatially-distributed satellite-based remote sensing data are used to validate the model. The consequences of the implementation of the new methods on modeling the regional runoff characteristics is analyzed in detail. By using measured discharge gauge data, this comparison serves additionally as an indirect validation of the snow model methods.

- The sixth chapter presents the conducted climate change impact study with the optimized hydrological model system. The basis are global atmospheric simulations that are dynamically downscaled and bias corrected. The respective models, simulations, and procedures are described. A special coupling strategy was developed to allow for realistically forcing the hydrological model in a very high horizontal resolution in order to cover the terrain complexities. The model results of 30 year scenario and control simulations are analyzed with a focus on assessing the impact of a changing climate on future snow coverage and melt-driven runoff conditions.

2

Study Area Berchtesgaden Alps

The *Berchtesgaden National Park* is located in southeast Germany in the Free State of Bavaria. The National Park (IUCN Category II) was founded in 1978 and comprises an area of 210 km^2, whereas the investigated catchment of the *Berchtesgadener Ache* exceeds the borders of the National Park covering an area of 433 km^2 in total. The National Park is the core zone of the UNESCO Man and Biosphere Reserve *Berchtesgadener Land*.

The region is characterized by an extreme topography with mountain ranges covering an altitude from 603 to 2713 m above mean sea level (MSL). About one quarter of the investigated catchment area has slopes steeper than 35°. The lake *Königssee* (603 m MSL) is situated next to the highest and best known summit of the region, the *Watzmann Mittelspitze* (2713 m MSL). The large altitudinal gradient (2110 m) between these two tourist attractions and the resulting different climatic conditions at a horizontal distance of about 3500 m illustrates the large spatial heterogeneity of the catchment. The mean annual precipitation ranges from 1500 mm in the valleys up to 2600 mm at elevated and peak regions.

Specific aspects of the region are high altitudinal gradients, a strong variability of meteorological variables in time and space, complex hydrogeological situations, unquantified lateral snow transport processes and heterogeneous snow cover dynamics.

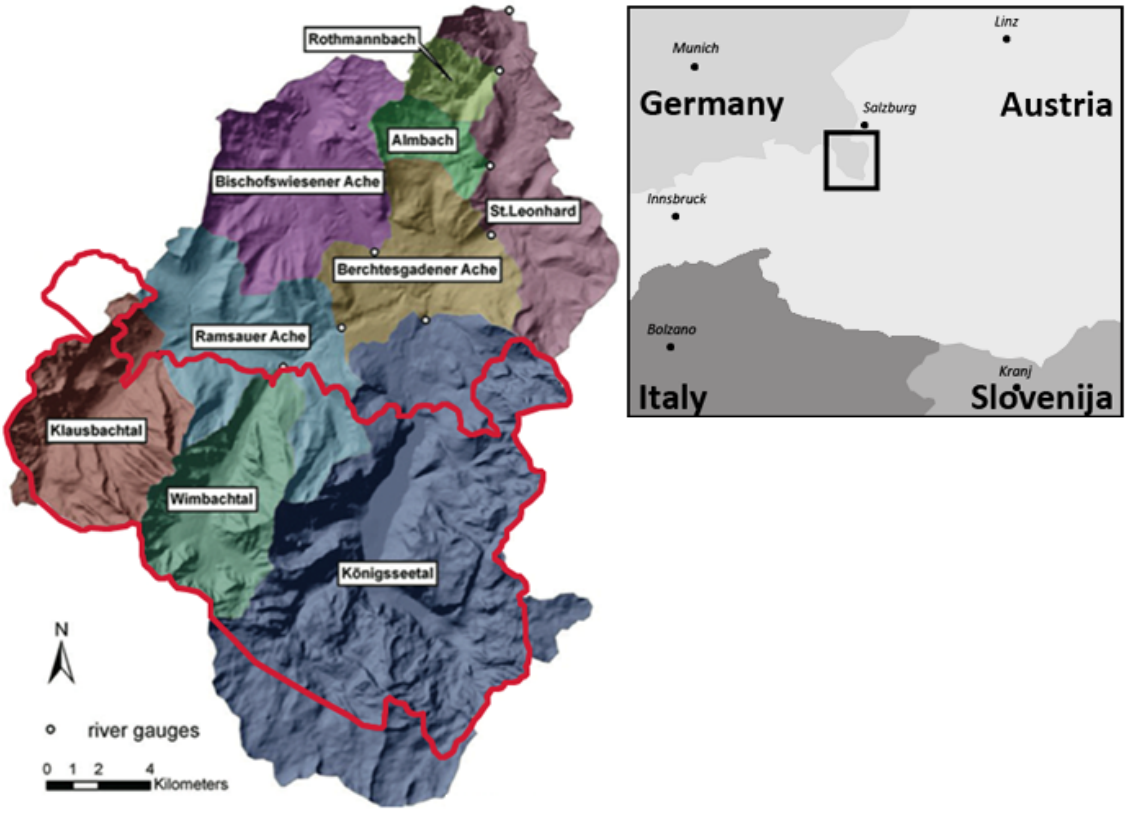

Figure 2.1: Location of the *Berchtesgaden National Park* and the catchment of the *Berchtesgadener Ache* with its subbasins. The core zone of the National Park is delineated in red (Marke *et al.*, 2013)

This results in high uncertainties in the quantification of the water balance. Because of the region's status as a protected area that is managed by the National Park authorities, it is on the one hand a widely "untouched" natural reserve that, on the other hand, has to handle the pressure of increasing tourism.

2.1 Land Use and Vegetation

Due to its status as a biosphere reserve, land use primarily depends on environmental protection policies and is only marginally influenced by economic activities (e.g. pressures resulting from Alpine sport and various sorts of touristic activities) (Franz *et al.*, 2012). The main ecosystem types found in the park area are forest (44.1 %), grass covered communities (21.0 %), rock and rubble fields (19.3 %), mountain pine

and green alder shrubs (12.4 %) as well as lakes (3.2 %) (StMLU, 2001). A detailed classification of land use for the whole catchment of the *Berchtesgadener Ache* is presented in Sec. 3.3, Fig. 3.7 and Tab. 3.5.

2.2 Geology and Soils

As part of the northern limestone Alps, the *Berchtesgaden Alps* form a geomorphological unit that consists of different parent materials. Triassic Dachstein limestone and Ramsau dolomite represent the dominant rock formations while Jurassic and Cretaceous rock series only cover small parts of the area. Thereby, the banked limestone formations are as thick as 1,000 m, covering dolomite material of 500 to 700 m thickness. (Kraller *et al.*, 2012; Marke *et al.*, 2013) The mountain ranges associated to the watershed *Berchtesgadener Ache* are shaped in close proximity as plateaus and ridges. Three valleys stretching from south to north, separating four mountain massifs from each other are representative for the area. The three main tectonic units in the area are arranged in such a way that the base Tirolicum is covered by the Lower Juvavicum, which is itself beneath the Upper Juvavicum. Alpine orogenic processes have produced the typical slope and inclined stratification of the existing rock formations. The mountain massifs *Hochkalter* and *Watzmann* slightly slope in a northern direction. (Fischer, 2005; Langenscheidt, 1981) The soluble limestone was exposed to karstification processes since the Alpine thrust, which took place in different phases. Typical karst phenomena in the region are the presence of sinkholes, basins, dry stream beds, caves and furrows. An exceptional characteristic is the Wimbach valley, which is filled with a 300 m thick layer of glacial deposits, consisting mainly of dolomite gravel that forms a porous aquifer. (Kraller *et al.*, 2011) Fig. 3.6 and Tab. 3.4 in Sec. 3.3 shows the soil types that are present in the catchment in detail. The main soil types are Syrosem (35.5 %), Cambisol (30.1 %), and Podsol (26.7 %).

2.3 Climatic Conditions

The predominant climate can be described as cool temperate and humid. Climate conditions are strongly influenced by topography with mean temperatures above 10 $°C$ and annual precipitation of 1.500 mm in the lower elevations and temperatures below 0 $°C$ and precipitation of up to 2.600 mm in the higher elevated parts of the catchment. Despite the dense station network in the catchment, the latter figure is still subject to high uncertainties because of the usual measurement errors (Sevruk, 1985) and a limited number of meteorological stations at high elevations. January is the coldest and July the warmest month (Strasser, 2008), whereas the seasonal course of precipitation is characterized by a maximum in July and a minimum in April with a mean altitudinal increase of 47 mm/100 m (Kraller et al. 2012). The mean decrease in temperature with increasing terrain elevation ranges from almost 0 K/100 m in winter to mostly -0.6 K/100 m , sometimes -0.7 K/100 m in summer. Temperature inversions occur frequently in winter, spring and autumn. (Franz *et al.*, 2012; Marke *et al.*, 2013) Sec. 3.2 presents meteorological station measurements that are used within this study. The interpolated fields of air temperature, relative humidity, wind speed, and global radiation for the period 2001-2010 (Figs. 3.2 - 3.4) show the mean climatic conditions and their spatial variety in the complex terrain of the catchment.

2.4 Regional Hydrology

The catchment of the *Berchtesgadener Ache* can be divided into the nine subcatchments illustrated in Figs. 2.1 and 3.1, following the location of the gauges listed in Tab. 3.3 and Fig. 3.5. Catchment hydrology is largely governed on the one hand by the seasonal storage of water in the snow pack, and on the other hand by the complex geological conditions in the region. The three headwater catchments in the south include the main mountain massifs *Watzmann* and *Hochkalter* and can be characterized as follows (Kraller *et al.*, 2012): Subbasin *Klausbachtal* covers an area of 42.78 km^2 and is surrounded by the plateau *Reiteralm* and the mountain *Hochkalter*. Its area is mostly covered by forests (lower parts) and ridge karst (higher parts). Subbasin *Wimbachtal* with an area of 35.69 km^2 is filled with dolomite gravel

deposits that built up a porous aquifer with depths of approximately 300 m. While the southern part is surrounded by dolomite rock mountains, the northern part is enclosed by the mountains *Hochkalter* and *Watzmann*, which both represent carbonate stratum. The *Königsseetal* with an area of 166.56 km^2 is the largest subbasin of the *Berchtesgadener Ache*. The genesis of the lake *Königssee* (511 m m^3), which gave the valley its name and which is located right in the center of the valley, goes back to the end of the Jurassic, where the lake evolved in a rift (Siebeck, 1982). Surrounding the lake in the north, the *Watzmann* and the *Hagengebirge* plateau form up huge mountain massifs that induce extremely steep relief gradients. *Steinernes Meer*, an extended karst plateau, surrounds the lake from the south. (Marke *et al.*, 2013)

Several tracer experiments, a spring database and geological conditions indicate a main groundwater flow direction from the south. Furthermore, groundwater redistribution between subcatchments is also indicated between three neighboring Alpine head subbasins stretching from north to south (Kraller et al., 2011).

The eight rivers within the watershed drain the area in a northerly direction. The rivers *Klausbach*, *Wimbach*, and *Königsseer Ache* drain three parallel valleys stretching from south to north. The *Klausbach* is a sinking stream during low flow conditions and the *Wimbach* is only emerging at a dam in the *Wimbachtal* that restrains the glacial deposits. The *Königsseer Ache* is draining lake *Königssee*. The *Klausbach*, draining the most western valley and later called *Ramsauer Ache*, receives inflow from the *Wimbach* from the south, plus the from the *Bischofswiesener Ache* from a northerly direction. In *Berchtesgaden*, the *Ramsauer Ache* and *Königsseer Ache* together form the *Berchtesgadener Ache* which flows north. Further downstream, the *Almbach* and *Rothmannbach* drain into the *Berchtesgadener Ache*. In *Salzburg*, the *Berchtesgadener Ache* flows into the *Salzach*, which contributes to the *Danube* river system that drains an overall area of 795 686 km^3 to the *Black Sea*. There are nine lakes in the region: *Königssee, Obersee, Hintersee, Funtensee, Grünsee, Schwarzensee, Seeleinsee, Laubseelein*, and *Blaue Lache*. (Kraller *et al.*, 2011)

3

Hydrological Model - Input Data and Model Setup

The water balance modeling in this study is done using the fully distributed, physically based hydrological model system WaSiM-ETH (Schulla & Jasper, 2007). A main objective of this work is to integrate new methods into the existing model that are specifically suited to reproduce Alpine snow cover processes in a high spatial and temporal resolution. The new snow model approaches are based on principles that were developed and validated within the high mountain specific snow cover model AMUNDSEN - Alpine MUltiscale Numerical Distributed Simulation ENgine (Strasser, 2008) and its predecessor and point version ESCIMO - Energy balance Snow Cover Integrated MOdel (Strasser & Marke, 2010). These models were developed and tested amongst others in the same catchment that is in the focus of this study. The following sections present details about the used models and the basic formulations and algorithms. Additionally, information about input and validation data, model setup, configuration and calibration, as well as details about the technical implementation structures are given.

3.1 Model WaSiM-ETH

The deterministic, fully distributed hydrological model WaSiM-ETH (Schulla & Jasper, 2007) is applied to simulate water flux and storage terms in the catchment. The model comprises process-based algorithms for the components of the terrestrial water cycle. WaSiM-ETH has been developed by Schulla & Jasper (2007) and was primarily applied in small to mesoscale Alpine catchments for impact studies of climate or land use change on the terrestrial water balance, and for flood forecasting in applications ranging from event-based to continuous simulations, e.g. by Gurtz *et al.* (2003), Verbunt *et al.* (2003), Jasper *et al.* (2004), Kunstmann *et al.* (2004), Kunstmann & Stadler (2005), Kunstmann *et al.* (2006), and Marx *et al.* (2008).
The required data for running the model are spatially distributed data sets to describe topography, land use, and soil parameters (section 3.3) as well as station measurements of meteorological variables, and discharge rates (section 3.2). Details about WaSiM-ETH can be found in the technical model description (Schulla & Jasper, 2007). The most important components and formulations of the model are described following a compilation by Wagner (2008).

Preprocessing The topographical analysis tool *Tanalys* derives exposition, slope, flow net structure, flow directions, flow times, and subcatchment boundaries from the digital elevation model (DEM).

Interpolation of Meteorological Input Data Hydrological models generally require precipitation, temperature, humidity, wind speed, and solar radiation data as the driving meteorological information. Usually this information is available as station data. Consequently, these point measurements have to be interpolated to the predefined regular grid. Applying gridded meteorological data sources, e.g. results of an atmospheric model, also requires an interpolation to the predefined regular grid. WaSiM-ETH provides the following interpolation techniques for the calculation of meteorological fields:

- Inverse distance weighting (IDW)
- Thiessen polygon

- Altitude-dependent regression
- Bilinear and bicubic spline
- Bilinear and bicubic spline interpolation of gradients and residuals
- Combination of Thiessen polygon method and constant lapse rate

The interpolation methods made use of in this study and according interpolation results are presented in section 3.2, and 6.1.

Radiation and Temperature Adjustment A radiation and temperature adjustment is implemented to compensate shadowing effects in mountainous regions. Shadowing affects incoming shortwave radiation. Sensible heat flux and air temperature depend among others on incoming shortwave radiation. Therefore, an adjustment of temperature and radiation is done following an approach by Oke (1987), which calculates a correction factor depending on sunshine duration, incident and zenith angle, and an empirical factor considering diffuse short wave radiation. This correction factor is applied for radiation and temperature.

Potential and Actual Evapotranspiration Potential evapotranspiration is calculated using the Penman-Monteith equation (Penman, 1948). Using this approach, the most important plant properties are taken into consideration, e.g. stomata resistance, root density distribution and depth, leaf area index (LAI), effective vegetation height and vegetation coverage. The seasonal variations of plant properties can be taken into account. To determine real evapotranspiration, potential evaporation is reduced dependent on the actual suction of the soil considering plant and soil physiological properties.

Interception For the storage of precipitation on vegetation and ground level a simple bucket approach is used with a capacity depending on the leaf area index LAI, the vegetation coverage degree, and the maximum height of the water on the leafs. The extraction of water out of the interception storage by evaporation is assumed to be at a potential rate. If the interception storage is filled, further precipitation will fall directly to the soil surface. A dedicated interception model for snow precipitation, or generally for the interaction between vegetation and snow is

not implemented yet but would be an interesting complement for a future extension of this work.

Infiltration and Generation of Surface Runoff The infiltration model is an integrated part of the soil model. Running WaSiM-ETH with Richards equation for the unsaturated zone, infiltration is considered in the calculation of the Richards equation (Richards, 1931). Surface runoff is generated if precipitation intensities are larger than the actual hydraulic conductivity of the soil.

Flow in the Unsaturated Zone Within this work, WaSiM-ETH is applied using the Richards equation (Richards, 1931) to calculate water fluxes in the unsaturated zone. The vertical fluxes are modeled as follows:

$$\frac{\partial \Theta}{\partial t} = \frac{\partial q}{\partial z} = \frac{\partial}{\partial z}\left(-k(\Theta)\frac{\partial \Psi(\Theta)}{\partial z}\right) \tag{3.1}$$

with Θ being water content in $m^3 \cdot m^{-3}$, t time in s, k the hydraulic conductivity in $m \cdot s^{-1}$, Ψ the hydraulic head as sum of suction ψ and geodetic altitude in m, q the specific flux in $m \cdot s^{-1}$, and z the vertical coordinate in m.

WaSiM-ETH calculates the Richards-equation in a spatially and temporally discretized form for each grid cell. Hydraulic conductivity and hydraulic head, which are functions of the water content, are parameterized through an approach by Van Genuchten (1980). Through the introduction of a recession constant k_{rec} for describing the recession of the saturated hydraulic conductivity k_s with depth z in

$$k_{s,z} = k_s \cdot k_{rec}^z \tag{3.2}$$

the generation of interflow q_{ifl} for soil layer n

$$q_{ifl} = k_s(\Theta_m) \cdot \Delta z \cdot d_r \cdot \tan i \tag{3.3}$$

is enabled with the drainage density d_r, which is a scaling parameter to consider river density. i is the local slope angle (inclination). Groundwater recharge in WaSiM-ETH is defined as the remaining vertically percolating water.

Using the Richards equation it is assumed that matrix flow dominates macropore flow. The Richards equation is interpreted as a combination of mass balance and Darcy equation, due to the fact that the used horizontal resolutions are much larger than the original lab scale. Hence, the corresponding parameters are not fully comparable to laboratory derived ones. In addition, they consider natural heterogeneities within the horizontal resolution and therefore must be interpreted as effective lumped parameters (Kunstmann *et al.*, 2007).

Flow in the Saturated Zone A horizontally two-dimensional groundwater model is coupled to the unsaturated zone. The unsaturated zone module calculates the flux between unsaturated zone and groundwater. With these boundary fluxes the lateral fluxes are calculated using the groundwater model, which is based on the mass balance equation and Darcy's law. Interactions between surface water and subsurface water are simulated using the leakage principle. Therefore, baseflow can only be generated when groundwater levels reach the river bed or lake bottom level. Reinfiltration of surface water into groundwater occurs if groundwater drops below river water level. If the model is run without groundwater flow, base flow Q_B is calculated in a conceptual way using a scaling factors Q_0 which is the maximum baseflow if the soil is saturated, the actual groundwater table h_{GW}, the geodetic altitude of the soil surface $h_{geo,0}$, the saturated hydraulic conductivity k_s and the recession constant k_B:

$$Q_B = Q_0 \cdot k_s \cdot e^{(h_{gw} - h_{geo,0})/k_B} \tag{3.4}$$

Discharge Routing Direct runoff and interflow are routed to the subcatchment outlet by subdividing the catchment into flow time zones which are calculated with the preprocessor Tanalys. Discharge routing in the river bed channel is performed by a kinematic wave approach using different flow velocities for different water levels in the channel. After the translation of the wave, a single linear storage is applied accounting for diffusion and retention. Finally, discharges from different subbasins are superposed.

Snow Accumulation and Melt Model formulations to simulate snow accumulation and ablation processes are explained in detail in section 4. There are three

methods implemented in WaSiM-ETH to calculate snowmelt. A temperature index approach, a temperature wind index approach, and a combination approach after Anderson (1973) and Braun (1985). The index approaches use calibrated parameters and actual air temperature and wind speed to assess snowmelt rates. The combination approach intends to calculate melt by an assessment of energy balance components by air temperature, wind speed and pressure. The widely used temperature index approach is used as a reference to evaluate the benefits of the newly implemented energy balance approach, which calculates the full energy balance of the snow cover. Additionally, algorithms were implemented to account for lateral snow redistribution (section 4).

3.2 Hydrometeorological Data

The meteorological data sets were recorded by 34 meteorological stations, of which 20 are operated automatically and provide hourly values of main meteorological variables. 14 of them are mechanical stations that provide daily measurements of precipitation. Six of the stations are situated on Austrian territory and operated by the *Central Institute for Meteorology and Geodynamics / Zentralanstalt für Meteorologie und Geodynamik(ZAMG)*. The stations on German territory are operated by the *Berchtesgaden National Park Administration (NPV)*, the *Administration Union of the Berchtesgaden-Königssee Region*, the *Bavarian Avalanche Warning Service / Lawinenwarnzentrale Bayern (LWZ)*, and the *German Weather Service / Deutscher Wetterdienst (DWD)* (Tab. 3.1). Fig. 3.1 shows the locations of the 16 automatic stations within the modeling domain. All data were sampled every ten seconds and recorded every ten minutes. Recordings are then aggregated to hourly values (i.e. average for temperature, humidity, wind speed, radiation, and atmospheric pressure; total for precipitation). The daily precipitation data of the 14 mechanical stations are disaggregated to hourly values using the hourly measurements of the automatic stations. The study reported here is based on station data from 2001 to 2010.

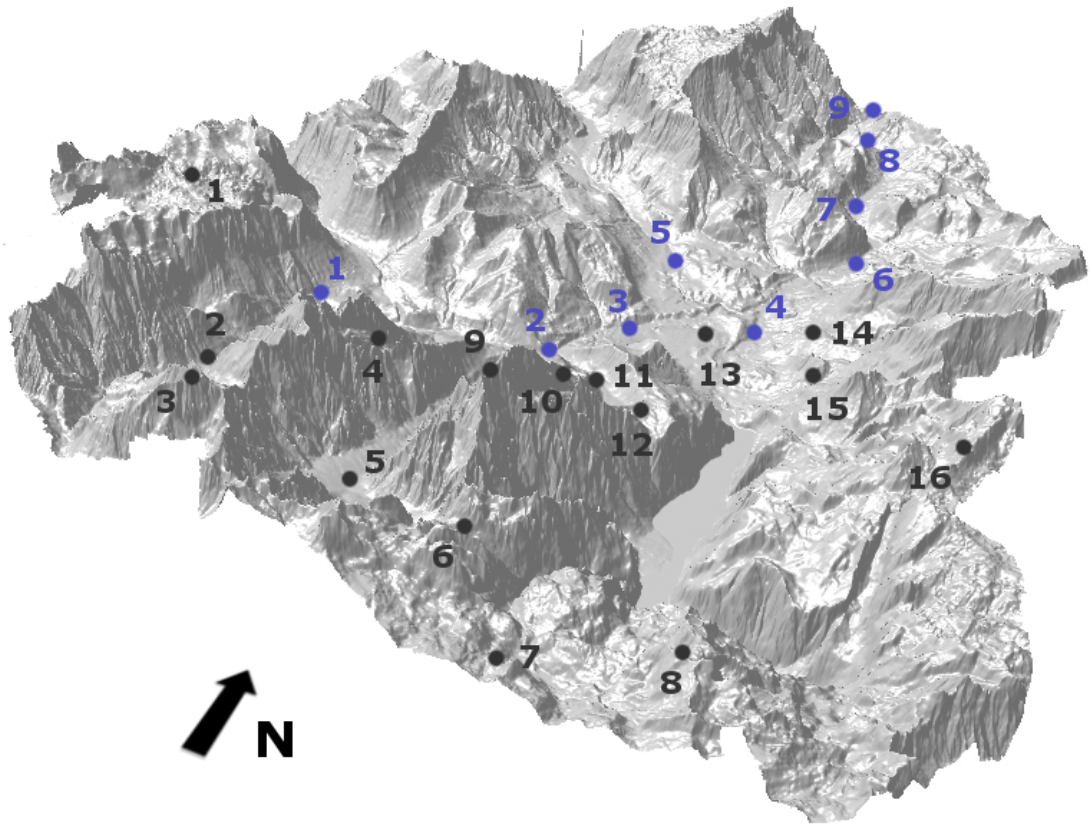

Figure 3.1: Digital elevation model (spatial resolution: 10 m) of the study area and positions of automatic meteorological stations (black) and runoff gauges (blue), listed in Tabs. 3.1 and 3.3.

Table 3.1: Altitude, set of recorded parameters, and temporal resolution for the meteorological stations of the automatic network in the *Berchtesgaden National Park*. Accuracy of the recordings used in the modeling is 0.3 ms^{-1} (wind speed), 0.3 °C (temperature), 1 % (humidity), 5 % (global radiation), and < 0.4 % (precipitation), respectively. Accuracy of the snow pillow recording SWE is 0.25 % and of the ultrasonic ranger measuring snow depth is 0.1 %. All accuracies according to the technical specifications of the manufacturers.

ID	Station	Altitude	Parameters	Temp. res.	Operator
1	Reiteralm 1	1753 m	T, H, WS, WD	10 min	LWZ
1	Reiteralm 2	1679 m	T, H, TS, SD	10 min	LWZ
1	Reiteralm 3	1611 m	T, H, P, GR, RR, SD	10 min	LWZ
2	Hinterseeau	839 m	T, H, WS, WD, GR, RR, SD	10 min	NPV
3	Hinterberghorn	2270 m	T, H, WS, WD, GR, RR	10 min	NPV
4	Blaueis	1651 m	T, H, WS, WD, GR, RR, SD	10 min	NPV
5	Brunftbergtiefe	1238 m	T, H, P, WS, WD, GR, RR, SD	10 min	NPV
6	Trischübel	1764 m	T, H, P, WS, WD, GR, RR, SD	10 min	NPV
7	Steinernes Meer	1900 m	T, H, P, WS, WD, GR, RR, SD	10 min	NPV
8	Funtenseetauern	2522 m	T, H, WS, WD	10 min	LWZ
9	Watzmanngrat	2630 m	T, H, WS, WD, GR, RR	10 min	LWZ
10	Watzmannhaus	1919 m	T, H, WS, WD, GR, RR	10 min	LWZ
11	Falzalm	1484 m	T, H, P, WS, WD	10 min	LWZ
12	Kühroint	1407 m	T, H, P, WS, WD, GR, RR, TS, SD, SWE	10 min	LWZ
13	Schönau	617 m	T, H, P, GR, DR, SS, WS, WD, AP	10 min	DWD
14	Höllgraben	640 m	T, H, P	10 min	LWZ
15	Jenner	1219 m	T, H, P, WS, TS, SD	10 min	LWZ
16	Schlunghorn	2155 m	T, H, WS, WD, GR, RR	10 min	NPV
-	Lofer	625 m	T, P, H, WS, WD, GR, SS, AP	1 h	ZAMG
-	Loferer Alm	1623 m	T, P, H, WS, WD, GR, SS, AP	1 h	ZAMG
-	SBG Flughafen	430 m	T, P, H, WS, WD, GR, SS, AP	1 h	ZAMG
-	Schmittenhöhe	1973 m	T, P, H, WS, WD, GR, SS, AP	1 h	ZAMG
-	Mülldeponie Winkel	699 m	P	1 d	NPV
-	Königsberg Pegel	1532 m	P	1 d	NPV
-	Schapbach	953 m	P	1 d	NPV
-	Kühroint (m.)	1418 m	P	1 d	NPV
-	Lahneralm	1240 m	P	1 d	NPV
-	St. Bartholomä	604 m	P	1 d	NPV
-	Wimbachschloss	926 m	P	1 d	NPV
-	Brunftbergtiefe (m.)	1238 m	P	1 d	NPV
-	Auf dem Gries	1435 m	P	1 d	NPV
-	Bindalm	1119 m	P	1 d	NPV
-	Eckau	1015 m	P	1 d	NPV
-	Lahnwaldfütterung	840 m	P	1 d	NPV
-	Mittereis	1325 m	P	1 d	NPV
-	Halsalm	1088 m	P	1 d	NPV

T = air temperature, H = relative humidity, WS = wind speed, WD = wind direction, SD = snow depth, SWE = snow water equivalent, SS = sunshine duration, GR = global radiation, DR = direct radiation, RR = reflected radiation, P = precipitation, AP = atmospheric pressure at sea level, TS = surface temperature, LWZ = Lawinenwarnzentrale Bayern / Bavarian avalanche warning service, NPV = Nationalparkverwaltung Berchtesgaden / Administration Berchtesgaden National Park, ZAMG = Zentralanstalt für Meteorologie und Geodynamik / Central Institute for Meteorology and Geodynamics, DWD = Deutscher Wetterdienst / German Weather Service

Snow water equivalent (SWE) at the station *Kühroint* is measured by means of a snow pillow. Snow depth is captured with an ultrasonic ranger. The point measurements of meteorological variables are spatially distributed to each grid cell of the model domain. Figs. 3.2, 3.3, and 3.4 show the resulting spatial distribution of the respective variables during the modeling period which are finally forcing the hydrological simulations. Minima, maxima, and mean values are listed in Tab. 3.2. Air temperature, humidity, wind speed, and precipitation are interpolated with an elevation-dependent regression function considering individual regression parameters for each time step and three different elevation layers. This allows for the detection and reproduction of atmospheric inversion conditions. Measured global radiation is used to calculate cloudiness by comparison to modeled topography- and time-dependent potential global radiation.

Table 3.2: Minima, maxima, and mean values for interpolated meteorological fields.

	min	max	mean
Temperature $[°C]$	-1.8	9.3	5.6
Humidity [%]	71.1	81.4	75.6
Wind speed $[m \cdot s^{-2}]$	1.1	5.3	2.1
Global radiation $[W \cdot m^{-2}\ ]$	1	119	56
Precipitation $[mm]$	1522	2731	1748

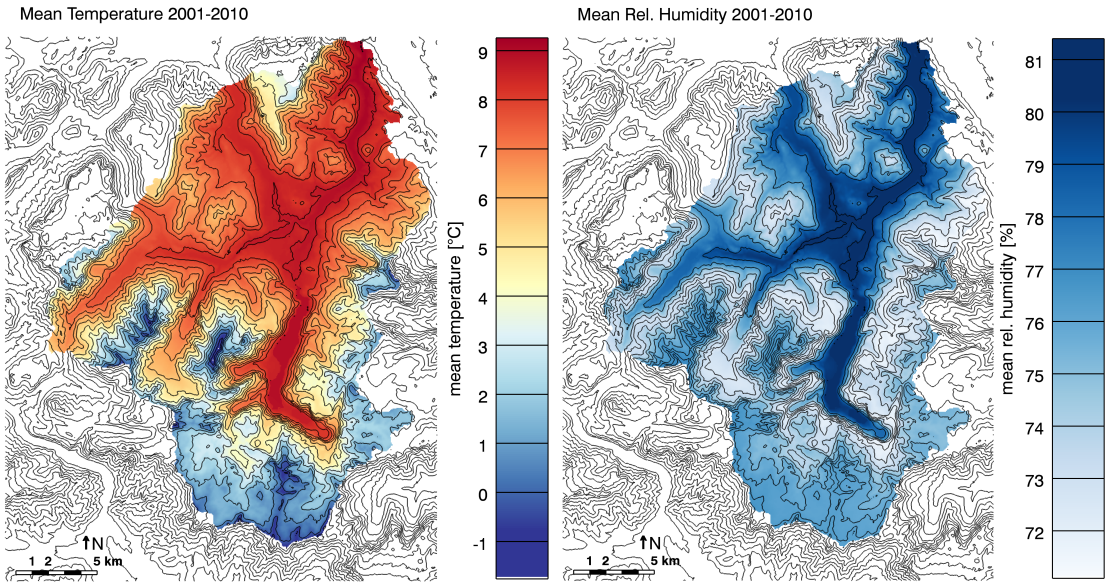

Figure 3.2: Interpolated fields of meteorological driving data 2001-2010: 2 m air temperature (left) in $°C$, and relative humidity in % (right).

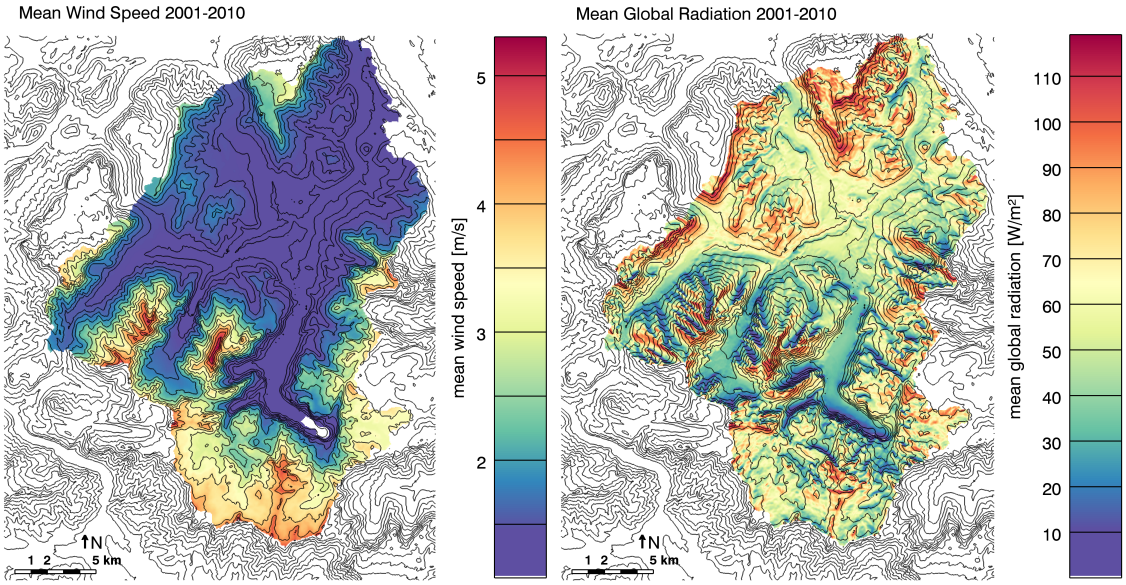

Figure 3.3: Interpolated fields of meteorological driving data 2001-2010: wind speed in $m{\cdot}s^{-1}$ (left), and global radiation in $W \cdot m^{-2}$ (right). Raw global radiation measurements are spatially interpolated using Inverse Distance Weighting and then modified by the radiation module according to local terrain and atmospheric characteristics.

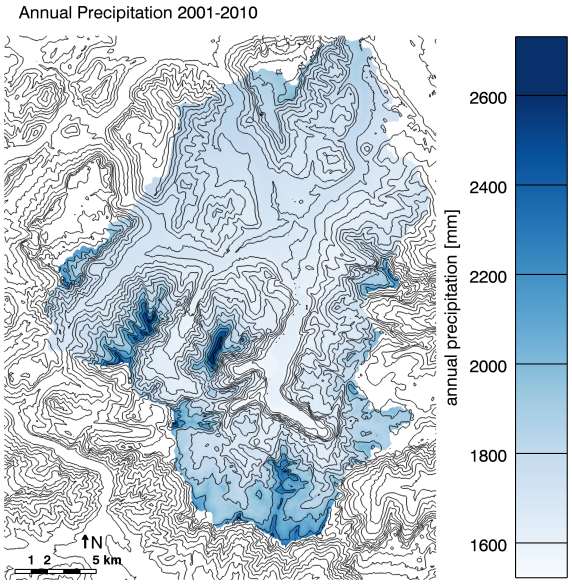

Figure 3.4: Interpolated fields of meteorological driving data 2001-2010: annual precipitation in mm.

Measurements of runoff are provided by the *Water Authority Traunstein* for 8 gauges in the region (Tab. 3.3). The discharge time series of the Austrian gauge *St. Leonhard* is provided by the *Hydrographic Service Salzburg*. Tab. 3.3 shows the name of the gauges, the associated streams, and the areas of the respective watersheds. Figs. 3.1 and 3.5 display the locations of the gauges. The division of the catchment in subbasins following the terrain surface and the location of the discharge gauges are delineated in shaded colors in Fig. 3.5. Runoff data are available from 2001 to 2010.

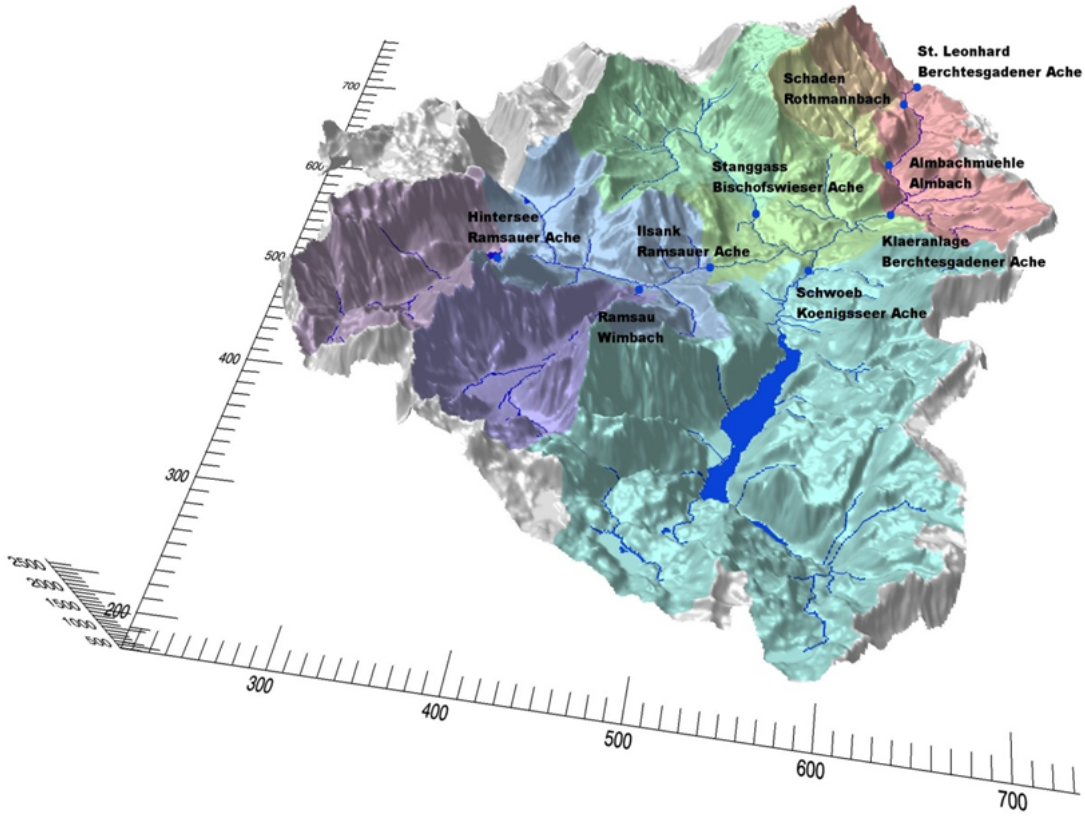

Figure 3.5: Overview of subbasins, discharge gauges, rivers, and lakes in the study area.

Table 3.3: Gauging stations, stream channels, and watershed areas of the subbasins.

ID	Gauge / Subbasin	Stream	km^2	%
1	Hintersee	Ramsauer Ache	42.78	9.9
2	Ramsau	Wimbach	35.69	8.3
3	Ilsank	Ramsauer Ache	47.05	10.8
4	Schwöb	Königsseer Ache	166.56	38.5
5	Stanggass	Bischofswiesener Ache	47.53	11.0
6	Kläranlage	Berchtesgadener Ache	33.11	7.8
7	Almbachmühle	Almbach	9.83	2.3
8	Schaden	Rothmannbach	8.00	1.8
9	St. Leonhard	Berchtesgadener Ache	42.06	9.6
			432.61	100

3.3 Spatially Distributed Data Sets

The hydrological model applied requires a set of spatially distributed input data. A digital elevation model (DEM) with a spatial resolution of 50 m is used to drive the model and derive all required topographic parameters. A regional soil map is provided by the *Bavarian Environment Agency*. During preprocessing, the soil types of the soil map are aggregated to 12 classes based on the classification of the *German Soil Map (BÜK)*. Fig. 3.6 shows the resulting map. Land use is classified based on the *HABITALP* project (Lotz, 2006) by interpretation of color-infrared aerial images. Habitats of all protected areas in the Alps are mapped on the basis of a jointly defined interpretation key. For the parts of the catchment situated in Austria, the *HABITALP* classification is not available. The land use map (Fig. 3.7) is complemented by data from the *Corine Land Cover (CLC)* project (http://www.eea.europa.eu/data-and-maps/) of the *European Environment Agency (EEA)*.

Table 3.4: Classification and assignment of the main soil types.

ID	Soil type	km^2	%
1	Lowmoor	0.49	0.11
2	Highmoor	0.74	0.17
3	Alluvial soils	3.25	0.75
4	Pararendzina	11.72	2.71
5	Rendzina	6.51	1.51
6	Pseudogley	0.58	0.13
7	Cambisol-Pseudogley	1.75	0.40
8	Kolluvisol	2.44	0.56
9	Cambisol	130.03	30.09
10	Podsol	115.53	26.73
11	Syrosem	153.51	35.52
12	Subhydrical soils	6.06	1.40
		432.61	100

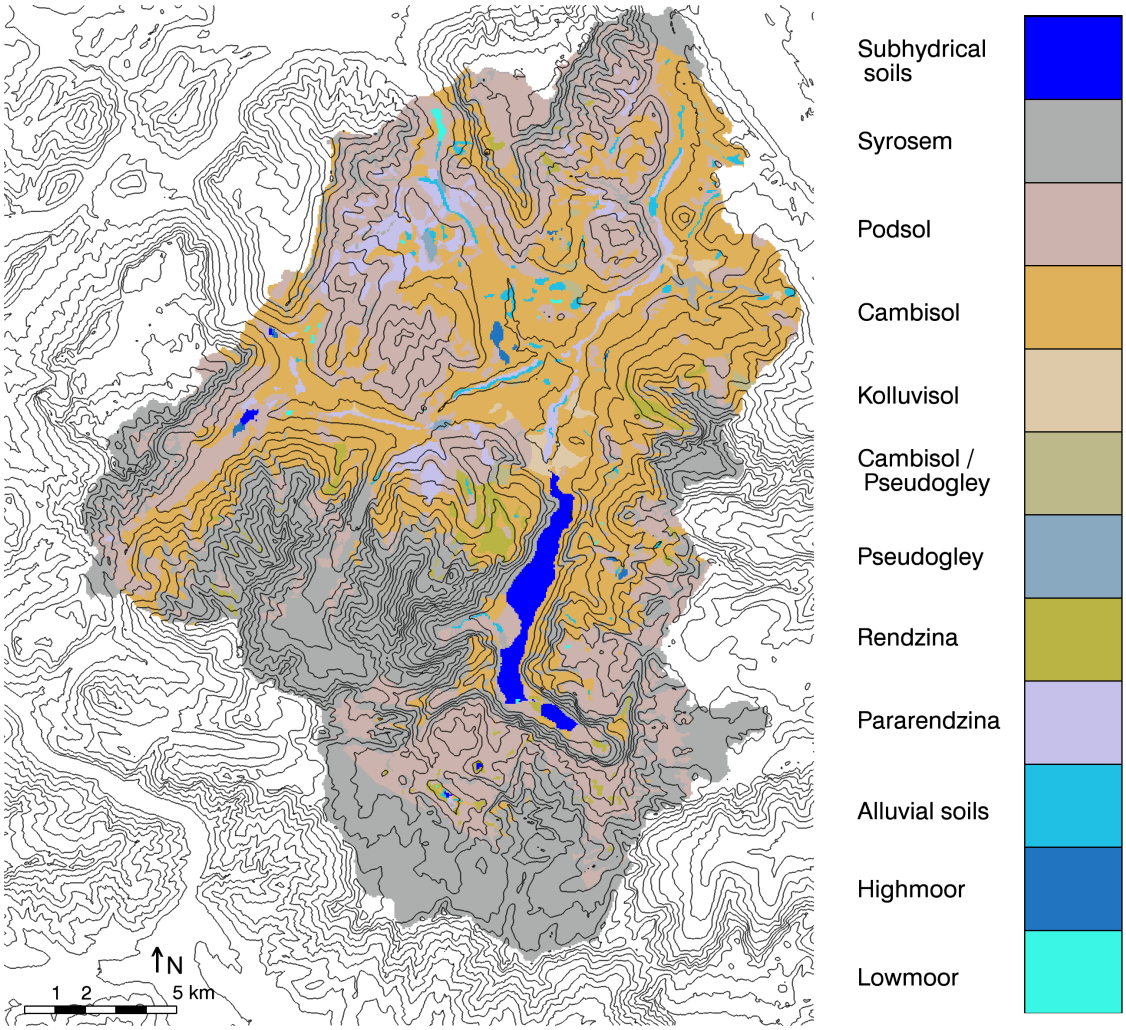

Figure 3.6: Map of soil types as classified for the model setup based on classifications of the *Bavarian Soil Map* and the *German Soil Map*.

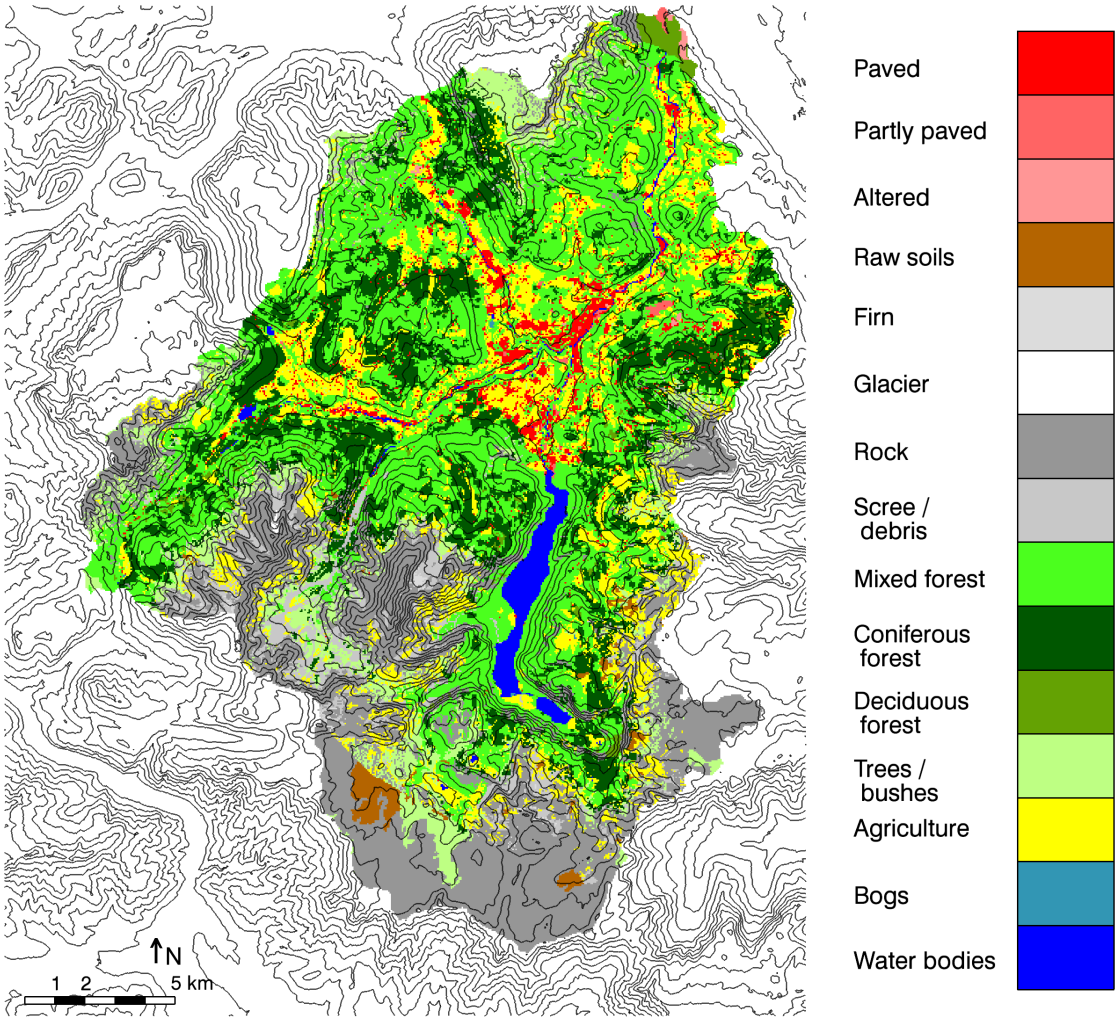

Figure 3.7: Map of land use classes as derived from the *HABITALP* classification and complemented by *Corine Land Cover* data.

Table 3.5: Classification and assignment of land use classes.

ID	Land use class	km^2	%
1	Water bodies	7.31	1.69
2	Bogs	0.13	0.03
3	Agriculture	59.19	13.70
4	Trees / bushes	30.99	7.17
5	Deciduous forest	4.51	1.04
6	Coniferous forest	62.25	14.40
7	Mixed forest	139.40	32.26
8	Scree / debris	15.89	3.68
9	Rock	93.55	21.65
10	Glacier	0.10	0.02
11	Firn	0.69	0.16
12	Raw soils	4.01	0.93
13	Altered areas	0.59	0.14
14	Partly paved areas	0.99	0.23
15	Paved areas	13.01	3.01
		432.61	100

To validate modeled spatial snow distribution fields, satellite-based remote sensing data are used that were recorded by the ETM+ (Enhanced Thematic Mapper) image sensor on board of the Landsat-7 mission satellite operated by the US government agency NASA. Landsat ETM+ data is organized in image tiles. Examples of the tiles that cover the study area of this work is shown in Figs. 3.8, 3.9 and 3.10 by presenting the real color representation of the visual channels.

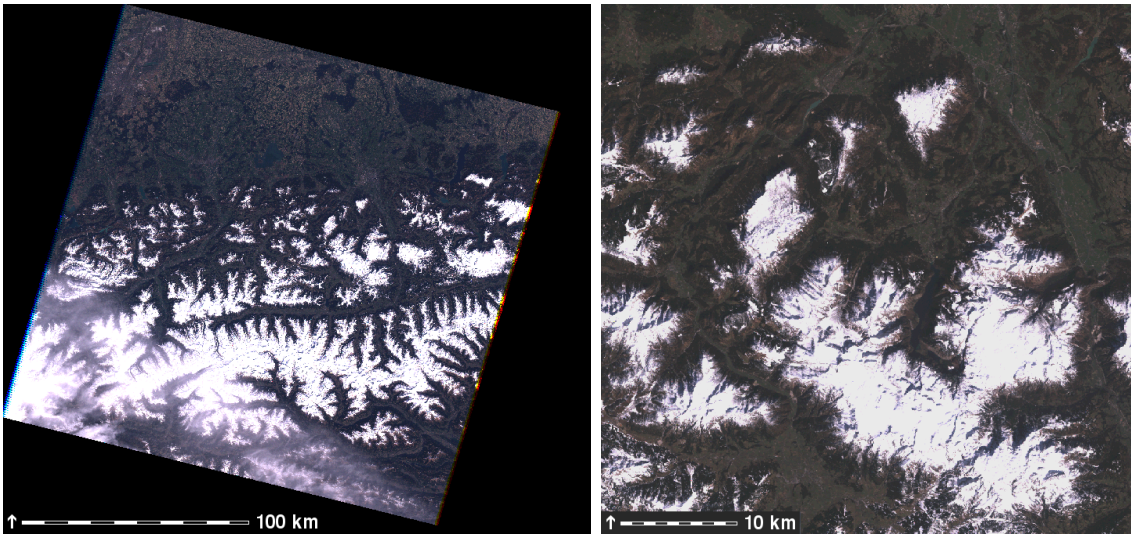

Figure 3.8: Landsat ETM+ scene April 07, 2002. After georeferencing (right), snow coverage is classified using the spectral information of the ETM+ channels.

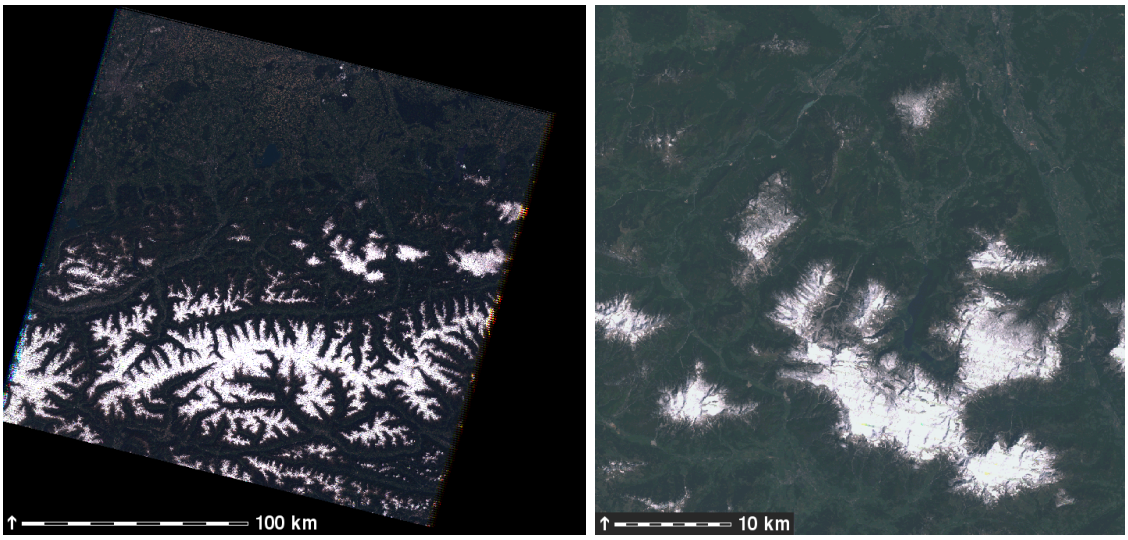

Figure 3.9: Landsat ETM+ scene May 30, 2004. After georeferencing (right), snow coverage is classified using the spectral information of the ETM+ channels.

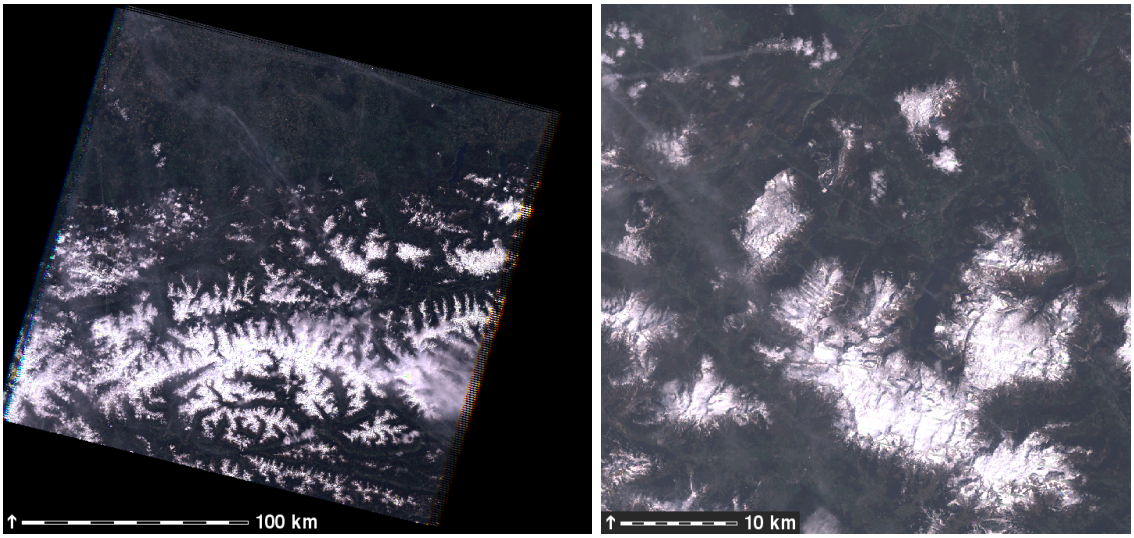

Figure 3.10: Landsat ETM+ scene May 01, 2005. After georeferencing (right), snow coverage is classified using the spectral information of the ETM+ channels.

3.4 First Standard Setup and Calibration

Model Configuration WaSiM-ETH model runs are performed for the period from 2001 to 2010 with a horizontal resolution of 50 m and a temporal resolution of one hour model time step. Evapotranspiration is determined by the Penman-Monteith model (Penman, 1948). Water flow in the unsaturated zone is calculated by solving the one-dimensional Richards equation (Richards, 1931). The saturated zone is represented by a two-dimensional groundwater flow model. The settings and used methods for the most important modules are listed in Tab. 3.6. Additional information on model setup and performance is listed in Kraller *et al.* (2012). To investigate the influence of the different snow process parameterizations on discharge modeling, four model runs with different combinations of snow cover modeling methods (Tab. 5.4) are performed. The different approaches are explained in detail in the following section.

Table 3.6: Module settings for the hydrological model WaSiM-ETH.

Module	Method
Spatial interpolation of meteorological input	Elevation-dependent regression function for each time step and three elevation layers (temperature, humidity, wind speed, precipitation) Inverse distance weighting (IDW) for raw global radiation
Evapotranspiration	Penman-Monteith
Snow	Energy balance and lateral redistribution / temperature index
Glacier	-
Interception	Bucket approach
Unsaturated Zone	Infiltration Green-Ampt / Peschke Richards equation and macropore infiltration
Groundwater	Darcy continuity equation
Routing	Single linear storage / cinematic wave

For the numerical quantification of the model performance, several performance criteria for hydrological model assessment exist (listed e.g. in Krause *et al.* (2005)). Nash-Sutcliffe model efficiencies (Nash & Sutcliffe, 1970) are widely used in hydrological modeling. The range of Nash-Sutcliffe efficiency (NS) values is $[-\infty...1]$, with 1 representing the best model performance where the modeled numbers equal the observed ones. The analyses in this work mainly use the NS criterion. The NS coefficient is calculated as

$$NS = 1 - \frac{\sum_{t=1}^{T}(Q_o^t - Q_m^t)^2}{\sum_{t=1}^{T}(Q_o^t - \overline{Q_o^t})^2} \tag{3.5}$$

with Q_o being observed discharge, Q_m modeled discharge, Q_o^t resp. Q_m^t the discharge values at time step t, and T the last time step.

Model Calibration As there are constraints in hydrological model formulations and in available input data, processes have to be simplified and parameterized. Some important parameters have to be calibrated before using the model. In this application, the parameters were calibrated manually comparing simulated and observed

runoff data by visual analysis and numerical performance criteria. The calibration and validation was done in the period 2003 - 2009. The period was separated in a calibration period (2005 - 2007) and two independent validation periods (2003 - 2005 and 2007 - 2009). Each model run was initialized with a one year simulation to avoid model spin-up effects in the analysis. The calibration was performed mainly for the subcatchment *Hintersee*. Parameter values were then transferred to the other catchments. This approach was chosen because *Hintersee* is the only mountainous catchment where runoff is not dampened by a big lake (lake *Königssee*, gauge *Schwöb*) or by a debris landfill with a dam at the outlet (valley *Wimbach*, gauge *Ramsau*) that introduce further uncertainties. The calibration procedure was done for two setups, one using the groundwater model and one using a conceptual method for calculating baseflow without the groundwater model. The results shown in this work are based on the setup using the conceptual groundwater approach, whereas model results using the lateral groundwater flow are presented in Kraller *et al.* (2012).

Tab. 3.7 shows the main calibrated parameters of the model. Single linear storage approaches are applied to direct runoff and interflow with the respective recession constants k_D and k_I. The runoff component Q_t at time t is calculated with the runoff component Q_{t_0} at time t_0, $\Delta t = t - t_0$ and the corresponding recession constants k by:

$$Q_t = Q_{t_0} \cdot e^{-\Delta t/k} \tag{3.6}$$

Running the model without the groundwater module, a similar approach is used to calculate baseflow with a calibrated outflow constant k_B (Eq. 3.4).

Additionally, the empirical scaling parameter drainage density d_r (Eq. 3.3), which linearly controls the amount of interflow, has to be calibrated. For modeling flow in the unsaturated zone, an adaption of the recession constant k_{rec}, which describes the decrease of the saturated hydraulic conductivity with increasing depth (Eq. 3.2), is necessary. Furthermore, an initial groundwater level as well as numbers and thicknesses of soil layers have to be determined.

Table 3.7: Main calibration parameters for WaSiM-ETH using Richards equation.

	Unit	Parameter	Value
k_D	$[h]$	recession constant for direct runoff	1
k_I	$[h]$	recession constant for interflow	5
k_B	$[m]$	outflow constant for baseflow	0.3
d_r	$[m^{-1}]$	drainage density	20
k_{rec}	$[-]$	recession constant for saturated hydraulic conductivity with depth	0.5
Q_0	$[-]$	scaling factor for baseflow	1

The model was calibrated during the two hydrological years 2005 - 2007. The model performance for this calibration period expressed in NS coefficients is presented in Tab. 3.8. Results at gauge 2 (valley *Wimbach*, gauge *Ramsau*) are not representative, as runoff measurements are disturbed by a dam construction which is not implemented in the model. Considering the complexity of the catchment and the uncertainties that comes with meteorological input data in such terrain, the NS values are in a satisfying range. NS coefficients are the highest in subcatchments 1, 3, 6, and 9 whereas runoff in subcatchments 4, 5, and 7 is modeled with a slightly lower performance. Fig. 3.11 shows modeled and measured runoff after calibration for the year 2006. This period serves as main development and validation basis for the following new snow modeling methods.

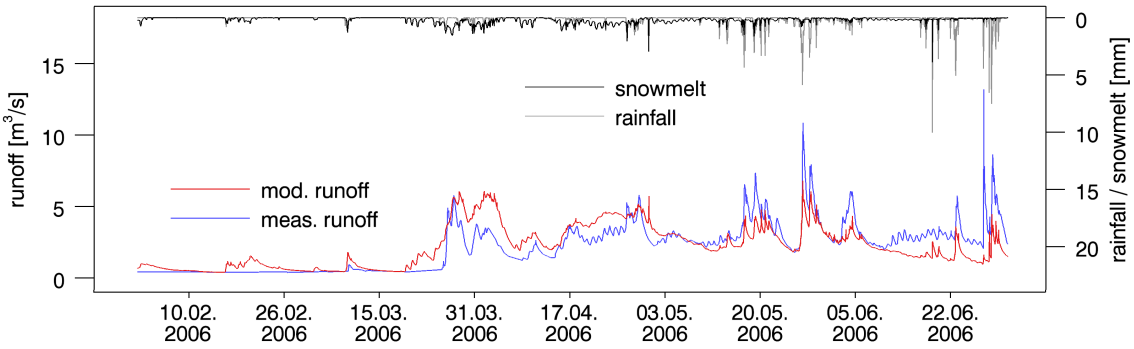

Figure 3.11: Modeled and measured runoff at gauge *Hintersee* from February to June 2006.

Two periods of two hydrological years each are chosen as two independent validation periods. The NS values for validation period I (2003 - 2005) and validation period

Table 3.8: Model performance in the calibration period 2005-2007 expressed by Nash-Sutcliffe coefficients as well as during validation period I (2003-2005) and validation period II (2007-2009). Measured data at gauge 8 is incomplete during this period. No data was available at gauge 7 during validation period II. Results at gauge 2 (*) are not representative, as runoff measurements are disturbed by a dam construction.

Subcatchment (ID)	1	2	3	4	5	6	7	8	9
NS cal. 2005 - 2007	0.61	-0.15*	0.51	0.35	0.26	0.85	0.43	-	0.81
NS val. I 2003 - 2005	0.46	0.05*	0.75	0.39	0.03	0.98	0.43	-	0.86
NS val. II 2007 - 2009	0.43	0.05*	0.60	0.50	-0.23	0.97	-	-	0.82

II (2007 - 2009) are listed in Tab. 3.8. Generally, NS values for the two validation periods are in the same range as for the calibration period. In catchments 1 and 5, the model performance in the validation periods is slightly lower than in the calibration period, whereas in the other catchments, the model performance is even higher during both validation periods. However, the reproduction of calibrated performance measures during independent time periods is not the main goal of this modeling study. The decisive focus is set on analyzing the differences in model performance implied by the implementation of the new snow model methods.

4

Model Extensions for the Simulation of Spatio-temporal Snow Mass Distribution

The main focus of this work lies on modeling snow cover distribution using methods of varying complexity. The implementation of robust formulations that facilitate the reproduction of snow cover evolution on a regional scale while maintaining transferability to changing climate conditions aims at enabling the performance of scenario calculations. Besides the existing snow module of WaSiM-ETH, which is based on a degree-day approach, methods were further developed and integrated that have proven to be robust representations of Alpine snow processes. The methods follow their implementation in the snow model AMUNDSEN (Strasser, 2008), and its predecessor and point version ESCIMO (Strasser & Marke, 2010). Model results of mountain snow cover evolution simulated by the formulations used in this study were previously compared to measurements in a variety of geographical regions, including analyses on a regional scale using snow cover data derived from satellite data (Strasser & Mauser, 2001; Strasser *et al.*, 2002, 2004; Prasch *et al.*, 2007; Strasser, 2008; Strasser *et al.*, 2008; Strasser & Marke, 2010; Strasser *et al.*, 2011; Zappa

et al., 2003). Model results were additionally validated within the framework of the two international snow model intercomparison projects SnowMIP (Etchevers *et al.*, 2004) and SnowMIP2 (Rutter *et al.*, 2009).
The following formulations and modules were implemented in WaSiM-ETH: 1) To determine melt as well as sublimation and resublimation rates, an energy balance scheme (Anderson, 1973; Strasser *et al.*, 2008; Weber, 2008; Strasser & Marke, 2010) was applied. 2) To account for lateral, gravitational snow transport processes, an algorithm according to Gruber (2007) was implemented. 3) To assess wind-driven snow redistribution, a method based on the idea of Winstral & Marks (2002) was further developed. All approaches were fully integrated in the snow module of WaSiM-ETH.

4.1 Snow Accumulation

Snow accumulation is controlled by snow precipitation, resublimation, and lateral snow transport. Snow precipitation is estimated for each grid cell using the interpolated air temperature during the event and a transition range with liquid and solid precipitation. The fraction of snow is given by:

$$p_{snow} = \begin{cases} 0 & \text{if } T > T_{R/S} + T_{trans} \\ \frac{T_{R/S}+T_{trans}-T}{2 \cdot T_{trans}} & \text{if } T_{R/S} + T_{trans} \geq T \geq T_{R/S} - T_{trans} \\ 1 & \text{if } T < T_{R/S} - T_{trans} \end{cases} \tag{4.1}$$

with the fraction of snow in total precipitation p_{snow}, air temperature T, temperature for 50 % snowfall fraction $T_{R/S}$, and half of the temperature transition range T_{trans} (Schulla & Jasper, 2007). In this study, $T_{R/S}$ is set to 273.66 K and T_{trans} to 1 K. Resublimation is explicitly determined during the energy balance calculation. It is neglected when using a temperature index approach, as this method determines mass losses only. Lateral transport mechanisms change snow accumulation rates according to the formulations in 4.3.

4.2 Snow Ablation

Snowmelt, sublimation, and lateral transport are the processes that lead to the ablation of the snow pack at a certain location. Snowmelt and sublimation are explicitly described by the implemented energy balance approach. When using a temperature index approach, snow sublimation can be regarded as inherently included in the calibrated melt or ablation factor. Generally, in the region investigated sublimation losses are small compared to snowmelt. Furthermore, ablation processes are controlled by the lateral transport mechanisms described in 4.3.

4.2.1 Temperature Index Approach

Temperature index approaches, e.g. the degree-day method, are widely used for modeling snowmelt. In WaSiM-ETH it is implemented by:

$$M = \begin{cases} c_0 \cdot (T - T_{0,m}) \cdot \frac{\delta t}{24} & \text{if } T > T_{0,m} \\ 0 & \text{if } T \leq T_{0,m} \end{cases} \tag{4.2}$$

with M being the melting rate per time step, c_0 a temperature-dependent ablation factor, T the air temperature, $T_{0,m}$ the lower temperature limit for snowmelt, and δt the model time step in hours. (Schulla & Jasper, 2007)
In this study, $T_{0,m}$ is set to 273.16 K. The degree-day factor c_0 was calibrated by Marx *et al.* (2008) in an adjacent catchment with similar characteristics and is kept constant at 2.5 mm d^{-1} K^{-1}, this value being in a valid range for Alpine catchments (Hock, 2003). Eq. 4.2 disaggregates the daily melt rates into hourly values by using hourly air temperatures and a scaled degree-day factor.

4.2.2 Energy Balance Approach

The energy balance of the snow surface is calculated hourly considering short-wave and long-wave radiation, sensible and latent heat fluxes, energy conducted by solid and liquid precipitation, (re)sublimation, and a constant energy input originating from the soil heat flux. The snow pack is regarded as a single layer of homogeneous

snow beneath the surface for which the energy balance is calculated. A distinction is made using air temperature as a proxy between melting conditions ($T \geq 273.16$ K) and non-melting conditions ($T < 273.16$ K), with T being the current air temperature. In the first case, a snow surface temperature of 273.16 K is assumed and melting occurs, if the computed energy balance is positive. In the case of non-melting conditions, an iterative scheme to close the energy balance is applied, where the snow surface temperature is adjusted and the long-wave emission and turbulent fluxes are recalculated until the energy balance residual equals zero (Strasser, 2008; Weber, 2008; Strasser *et al.*, 2011).

The decision between melting and non-melting conditions by using air temperature as a proxy has proven to be a stable approach when determining the energy balance of the surface (Weber, 2008). For this application - runoff simulations on the regional scale - the processes in the underlying snow layers are only of interest in the respect that they can influence the energy balance of the surface by a potential cold content. The proxy approach has proven to be robust, as air temperature above a snow surface is controlled by the energy balance of the snow cover beneath (Weber, 2008). However, situations might occur where air temperature exceeds 273.16 K while the snow surface underneath is still below that threshold. In these instances, the assumption fails and the model possibly produces snow melt if the energy balance is positive.

For a snow surface, the energy balance can be expressed as

$$Q + H + E + A + G + M_{ae} = 0 \tag{4.3}$$

where Q is the short-wave and long-wave radiation balance, H the sensible heat flux, E the latent heat flux, A the advective energy supplied by solid or liquid precipitation, G the soil heat flux, and M_{ae} the energy potentially available for melting during a given time step (Anderson, 1973). These fluxes are schematically illustrated in Fig. 4.1. All energy flux densities are expressed in Wm^{-2}. The soil heat flux G is assumed to be constant in space and time, as it is very small compared to other fluxes. It is set to 2 Wm^{-2}, this value being a robust average for mid-European Alpine sites (Durot, 1999). The available energy for melting M_{ae} can be computed for the case of melting conditions ($T \geq 273.16$ K). For this case, all fluxes are calculated with an assumed snow surface temperature of 273.16 K and M_{ae} is

the remainder of the energy balance equation. If $M_{ae} > 0$, the amount of melting M in mm is calculated as

$$M = \frac{M_{ae} \cdot dt}{c_m} \tag{4.4}$$

where c_m is the latent heat of melting.

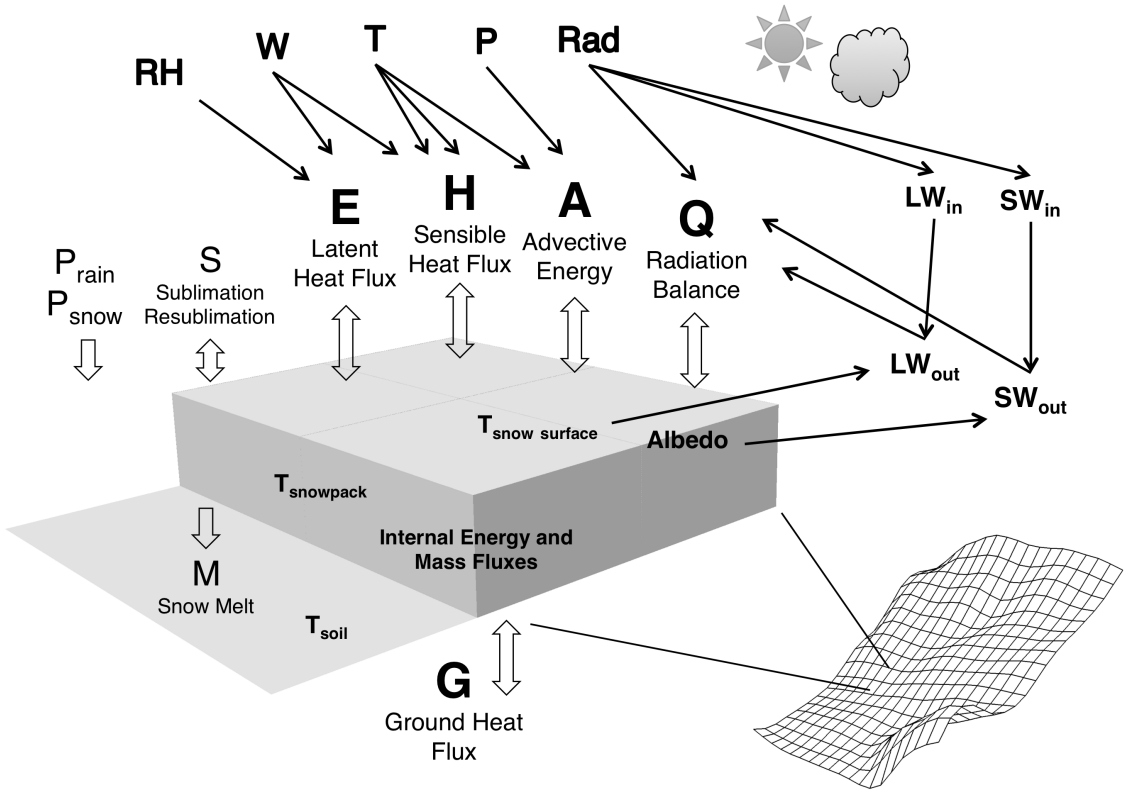

Figure 4.1: Schematic overview of the energy and mass fluxes at the snow cover, the driving meteorological variables and the snow cover state variables.

For consistency, the snow cover energy balance model uses the same radiation model to the determine the terms of the radiation balance Q as the evapotranspiration module of the hydrological model documented in Schulla & Jasper (2007).
The equations for calculations of sensible and latent heat fluxes can be found in Kuchment & Gelfan (1996), Strasser (2008), and Strasser *et al.* (2008). Sensible

heat flux H is calculated as

$$H = 18.85 \cdot (0.18 + 0.098 \cdot W) \cdot (T - T_s) \tag{4.5}$$

where W is wind speed in $m \cdot s^{-1}$, T air temperature in K, and T_s snow surface temperature in K. Latent heat flux E is simulated as

$$E = 32.82 \cdot (0.18 + 0.098 \cdot W) \cdot (e_l - e_s) \tag{4.6}$$

where e_l is the water vapor partial pressure at measurement level in $mbar$ and e_l the water vapor saturation pressure at the snow surface in $mbar$, the water vapor pressures being calculated using the *Magnus formula*. The respective accompanying mass flux S, sublimation or resublimation from or to the snow cover, is calculated as

$$S = \frac{E \cdot dt}{c_s} \tag{4.7}$$

where c_s is the latent heat of sublimation.
The advective heat flux by precipitation is calculated using precipitation amounts and phase, as well as air temperature according to Strasser (2008) for rainfall as

$$A = P_{rain} \cdot c_{lw} \cdot (T - 273.16\,K) \tag{4.8}$$

and for snowfall as

$$A = P_{snow} \cdot c_{sw} \cdot (T - 273.16\,K) \tag{4.9}$$

where P_{rain} is rainfall, P_{snow} snowfall, c_{lw} the specific heat capacity of liquid water, and c_{sw} the specific heat capacity of ice, both in $J \cdot kg^{-1} \cdot K^{-1}$.

4.3 Lateral Redistribution of Snow

Lateral redistribution of snow is a complex process on different spatial and temporal scales depending on a variety of controlling mechanisms. Two main drivers for lat-

eral transport are topography and atmospheric boundary conditions, mainly actual surface wind speed and direction. This work aims at introducing and investigating modules to simulate snow redistribution not on an event-basis, but on the catchment scale and in a model complexity that facilitates to reproduce the hydrologically relevant redistribution of water. This is implemented by the application of an algorithm to calculate gravitation-driven transport of snow in steep mountain topography and a parameterization of wind-driven snow redistribution.

4.3.1 Gravitational Snow Transport

Sliding of snow from steep walls and faces to the base of the slopes was identified to be an important process in modeling accumulation and ablation of snow in high mountain regions with steep terrain (Dadic *et al.*, 2008; Strasser, 2008; Bernhardt & Schulz, 2010, e.g.). For distributed snow process modeling on the catchment scale and long-term simulations of high mountain snow cover dynamics and glacier response to climate change in Alpine regions, accounting for gravitational, lateral redistribution of snow is an indispensable prerequisite for obtaining realistic results for the simulated SWE development. An approach according to Gruber (2007) was implemented in the hydrological model to consider the gravitational transport of snow. It was tested in the studies by Dadic *et al.* (2008) and Strasser (2008). Bernhardt & Schulz (2010) successfully implemented a similar approach in a distributed snow model. Our study presents the first implementation of such a method within a fully distributed, physically based water balance model.
The approach is based on an analysis of the topography and the available mass input. It is a mass-conserving, multiple-direction flow propagation procedure which routes entrained snow masses along predefined flow couloirs derived from the DEM. In each cell, the fraction of mass F_{NB} drained to a neighbor NB is a function of topography only and totals one over all neighboring cells in order to conserve mass. Deposition D_{grav} is limited by the local maximum deposition $D_{max,grav}$ and determined by the available incoming mass M_{in} that is the sum of the received inflows from the neighboring cells. Potential surplus of sliding snow is transported into the neighboring cells. All masses are denoted as mm SWE. The flow F_{NB} into each neighbor NB of a cell is given by the total outflowing mass of a cell M_{out} and the

draining fractions f_{NB}:

$$F_{NB} = (M_{out}) \cdot f_{NB} \tag{4.10}$$

The calculation of the draining fractions is explained in detail in Gruber (2007). The total outflow of a cell is:

$$M_{out} = \begin{cases} f_{erosion} \cdot SWE + M_{in} - D_{grav} & \text{if } i \geq i_{erosion} \text{ and } SWE > 0 \\ M_{in} - D_{grav} & \text{if } i \geq i_{erosion} \text{ and } SWE = 0 \\ M_{in} - D_{grav} & \text{if } i < i_{erosion} \end{cases} \tag{4.11}$$

with $f_{erosion}$ being an erosion factor depending on model time step, SWE the snow storage in the current pixel, i the local inclination, $i_{erosion}$ lower inclination limit for snow erosion, M_{in} the received inflow from all neighbors, and D_{grav} the deposition in the pixel in mm.

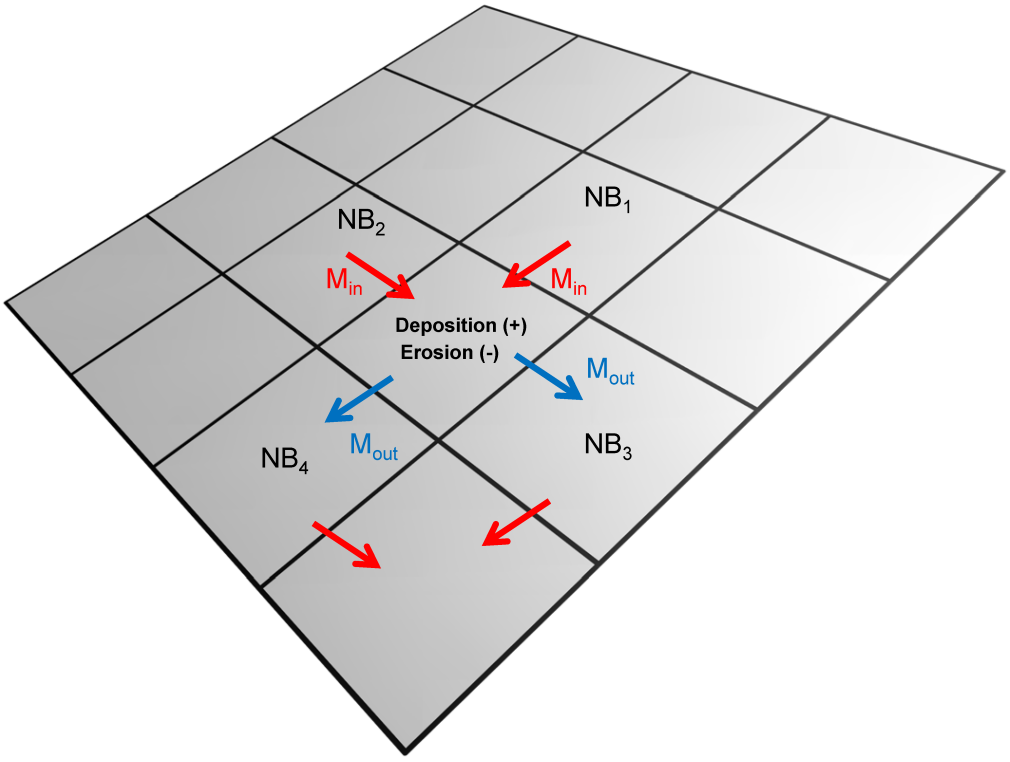

Figure 4.2: Illustration of the gravitational snow slide scheme for a simple slope.

Deposition D_{grav} is controlled by the available mass and the local maximum deposition. The amount of snow deposited in a cell can be quantified as:

$$D_{grav} = \begin{cases} M_{in} & \text{if } M_{in} < D_{max,grav} \\ D_{max,grav} & \text{if } M_{in} \geq D_{max,grav} \end{cases} \tag{4.12}$$

with $D_{max,grav}$ being the maximum snow mass that can be deposited within a single DEM cell during a slide event. $D_{max,grav}$ is determined by local inclination. The following simple linear function is used to quantify $D_{max,grav}$ (Gruber, 2007):

$$D_{max,grav} = \begin{cases} (1 - \frac{i}{i_{lim}}) \cdot D_{lim} & \text{if } i < i_{lim} \\ 0 & \text{if } i \geq i_{lim} \end{cases} \tag{4.13}$$

where D_{lim} is an upper deposition limit, e.g. the maximum amount of snow that would be deposited on horizontal terrain, and i_{lim} an upper limiting angle above which all incoming sliding snow is transported downslope. D_{lim} is related to the model time step.

The parameterization of the model depends on the model time step, the spatial resolution of the DEM, and on local topography characteristics. Some values have to be derived empirically and parameters have to be adapted to produce flow paths which are coherent with visual experience. For the current study, the model was initialized with the following settings: $f_{erosion}$ is 1 % of the actual snow storage in a cell. If local inclination i exceeds the lower limiting angle $i_{erosion}$ of 45°, snow is eroded (Eq. 4.11). As a reasonable value for the threshold, above which incoming sliding snow is not deposited, but entrained further downslope (i_{lim}, Eq. 4.13), 55° was identified. Cells that are steeper than i_{lim} still receive snow by precipitation. They are constantly freed of snow by gravitational transport within a certain time period after a snowfall depending on $f_{erosion}$.

In this parameterization both flow and deposition physics are not described explicitly, but characterized by simple parameters. Since the effects of kinetic energy are not included, potential uphill flow of fast moving snow masses are neglected. Many other factors like stability criteria in the layers of the snow pack, type of underground, local-scale meteorological conditions, or external forces also are not considered here. Therefore, the timing of avalanches on an event basis cannot be

predicted by this method, but the procedure allows for a hydrologically plausible redistribution of snow. (Strasser, 2008)

4.3.2 Wind-driven Snow Redistribution

A main driver of spatial heterogeneity of the snow cover in complex terrain is redistribution of snow caused by wind. Wind-driven snow redistribution is important to local and regional hydrology as well as to the assessment of the danger potential due to natural hazards, as wind-loaded slopes are often avalanche-prone locations due to big snow masses paired with instabilities within the snow pack. Apart from the wind impact on the energy balance of the snow pack, three major interaction mechanisms of wind and snow shape the complex snow cover distribution in mountainous terrain: Preferential deposition of snow precipitation, wind-driven redistribution of previously fallen snow, and the effective sublimation of suspended snow into the atmosphere (Lehning *et al.*, 2008; Mott *et al.*, 2008; Dadic *et al.*, 2010a). These processes lead to a highly variable distribution of snow on different spatial scales. (Blöschl & Kirnbauer, 1992; Pomeroy *et al.*, 1998; Liston & Sturm, 1998; Lehning *et al.*, 2008; Strasser, 2008; Bernhardt *et al.*, 2010; Dadic *et al.*, 2010a,b; Mott *et al.*, 2010)

Several methods of different complexity have been developed to account for wind-driven snow transport and redistribution e.g. by Liston & Sturm (1998); Winstral & Marks (2002); Lehning *et al.* (2008); Mott *et al.* (2008); Raderschall *et al.* (2008); Bernhardt *et al.* (2010); Dadic *et al.* (2010a). In this study, a simple parameterization is used to capture all the wind-driven snow processes described and to estimate and reproduce the result of their interaction. The basic principle is the extraction of locations that are sheltered from or exposed to wind by a topography analysis and a respective correction of snow precipitation. This approach is in line with the idea of Winstral & Marks (2002). The topography analysis is based on a modified algorithm by Corripio (2003) that calculates the sky view factor (SVF). The routine was modified to determine a partial, directed sky view factor (SVF_{dir}). The correction is done by specification of sectors representing prevailing main wind directions. Snow precipitation is corrected by:

$$P_{snow} = P_{snow} + C_{wind} \cdot P_{snow} \tag{4.14}$$

where P_{snow} is solid precipitation (snow). The correction factor C_{wind} is calculated for each cell of the domain:

$$C_{wind} = e \cdot (D_{max,wind} \cdot (1 - SVF_{dir}) - 1) + 0.1 \tag{4.15}$$

with a (linear) elevation weighting factor e, the directed sky view factor SVF_{dir}, and the maximum possible deposition $D_{max,wind}$. e ranges from 0 at the lowest elevated pixel to 1 at the highest pixel and linearly scales the amount of snow redistribution. This scaling is based on the assumption that the lower wind speeds at lower elevations reduce redistribution. In this implementation, the calculation of C_{wind} results in values between -0.82 and +1.84. Fig. 4.3 shows the field of C_{wind} for a main wind direction south-west (left) and no distinct wind direction (right). This method certainly has drawbacks and limitations, as it is a simple estimation that should not be expected to produce highly accurate values for redistributed snow masses. Accuracy in modeling these processes on the regional scale additionally are highly depending on spatial and temporal resolutions. Benefits of the method are its computational efficiency and the transferability without the need for complex wind field input data. In contrast to Winstral & Marks (2002), the application is restricted to lateral snow redistribution and does not adjust wind speed values for the computation of turbulent fluxes.

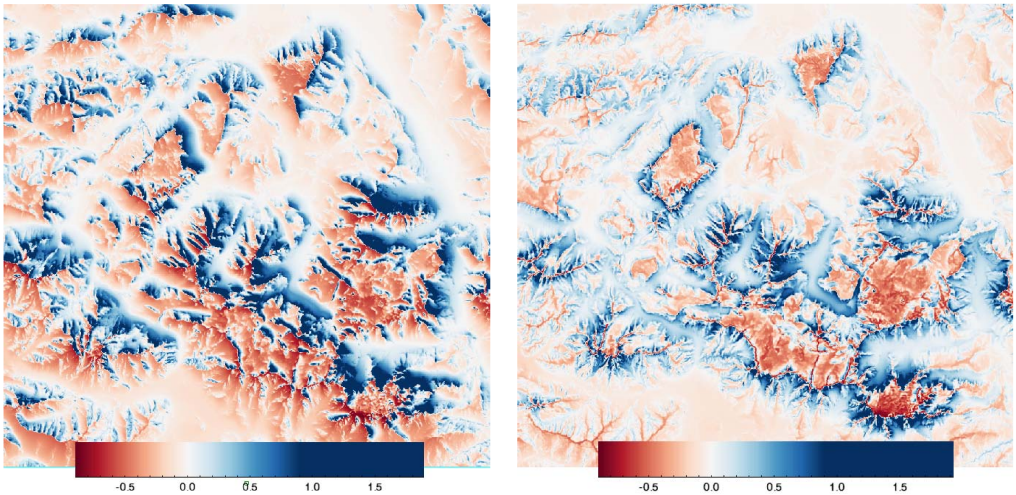

Figure 4.3: Examples for the field of wind correction factor C_{wind} for wind direction south-west (left) and no distinct wind direction (right). Red indicates erosion and blue deposition.

4.4 Technical Implementation of the Enhanced Snow Model Approaches

The enhanced snow model approaches were fully implemented in the core of the hydrological model WaSiM-ETH and tested in model versions 8.0.5, 8.3.0, and 8.8.0. The program is written in the programming language C++, and makes use of the *Open Multiprocessing* (OpenMP) libraries to allow for fast shared-memory parallel processing. The algorithms for simulating lateral transport make use of preprocessed input grids that were derived from the DEM in external routines using the software package IDL (*Interactive Data Language*). The following section lists the technical details of the implementation of modules that simulate the energy balance of the snow cover and lateral snow redistribution processes, consisting of gravitational snow transport and wind-induced snow redistribution. The single methods and combinations of them can be chosen by call codes in the control file of the hydrological model WaSiM-ETH as listed in Tab. 4.1. The developed approaches have been officially released within WaSiM model version 9.06.02.

Energy Balance of the Snow Cover The calculation of the energy balance of the snow cover (4.2.1) was implemented in the snow module of WaSiM-ETH. The respective parts of the source code are listed in appendix (A.1). The complex simulation of terrain dependent radiation processes and the derivation of cloudiness from radiation measurements is implemented in the evapotranspiration module of WaSiM-ETH (Schulla & Jasper, 2007).

Lateral Snow Transport Gravitational snow transport is simulated during runtime. The algorithm described in 4.3.1 was implemented in the snow module of WaSiM-ETH (source code in appendix (A.2). The algorithm uses input fields that are derived from the DEM during preprocessing. These are fields of the draining fractions to neighboring cells f_{NB}, and the local maximum gravitational deposition $D_{max,grav}$ (section 4.3.1). The IDL source code for calculating these input fields is appended (A.4). Similar to gravitational transport, the runtime simulation of wind-driven snow redistribution is implemented in the snow module of WaSiM-ETH (A.3).

The according spatial input field C_{wind} (section 4.3.2) is derived from the DEM in a preprocessing routine programmed in IDL (A.5).

Table 4.1: Module call codes for different combinations of the implemented methods in the control file for the hydrological model WaSiM-ETH.

Method	CTL-Code
EnBal	5
EnBal + grav.slides	6
EnBal + grav.slides + wind red.	7
T-Index + grav.slides	8
T-Index + grav.slides + wind red.	9
T-Index + wind red.	10
EnBal + wind red.	11

5

Performance of the Snow Model Extensions

The following section evaluates the performance of the enhanced hydrological model system in reproducing the hydrological processes of the investigated catchment. In a first step, the capability of the energy balance approach in simulating snow cover development at the local scale is discussed. Computed values of SWE are compared to measurements at the station *Kühroint*. The functionality of the algorithm is depicted in detail by presenting the simulated energy fluxes in a selected time period. Consequently, spatially distributed model results are presented for the regional catchment scale. The influence of integrating the separate snow model approaches, comprising the energy balance approach and the simulation of lateral redistribution, is discussed in a step by step performance evaluation. The modeled spatial snow distribution fields are finally validated using satellite-based remote sensing data recorded by the ETM+ (Enhanced Thematic Mapper) image sensor on board the Landsat-7 mission satellite operated by the US government agency NASA. Ultimately, the performance of the hydrological model in simulating runoff generation and streamflow dynamics influenced by snow accumulation, redistribution, storage, and ablation is validated using discharge gauge measurements in Sec. 5.4.

5.1 Performance on the Point Scale

Fig. 5.1 shows the seasonal snow cover evolution at the station *Kühroint* during two winters. Simulated and observed values of SWE are compared. Both the temperature index and energy balance approach perform differently during the two winter seasons. The course of SWE during the snow-rich winter 2005/2006 is reproduced better by the energy balance approach and underestimated by the temperature index method. For the winter season 2006/2007, which is characterized by an exceptionally small amount of snow, the temperature index method performs slightly better. The energy balance approach overestimates SWE in this season. This is mainly caused by missing the melt out event in December 2006. However, these validation results are based on the measurements and simulations at a single point in the catchment, which means at one out of 172,959 model grid cells. Moreover, the location of the station is not representative for the whole study area. It can be assumed that these results would strongly vary within the complex terrain of the catchment, the key characteristics for snow cover development being very inhomogeneous, e.g. exposure, altitude, steepness, surrounding terrain, or land cover. The performance of the temperature index model in Fig. 5.1 could have been improved at the point scale by additional calibration e.g. by different factors for single winter seasons.

Fig. 5.2 the calculated energy fluxes at the snow cover during the simulated SWE for three weeks in April and May 2006. The daily variations and the amount of incoming and outgoing energy to or from the snow cover are shown as a snap-shot result to demonstrate how the energy balance scheme explicitly describes the energy fluxes at the snow surface. Snow rapidly melts off during this time period. The main drivers are radiation and sensible heat flux. Net radiation is the energy flux that results by summing up incoming and outgoing short- and long-wave radiation. The daily variations of this term originate from the dominant incoming solar radiation and nocturnal outgoing long-wave radiation. Maximum values in this period are 200 Wm^{-2} net radiation energy income. Sensible heat flux follows the radiation cycle in daily variations according to the course of air temperature. The maximum values (100 Wm^{-2}) are slightly shifted in time. Decrease in SWE, i.e. snowmelt and sublimation, obviously occurs mainly during daytime when the energy input is high. The short period from April 29 to May 1 indicates cloud-covered sky with incoming

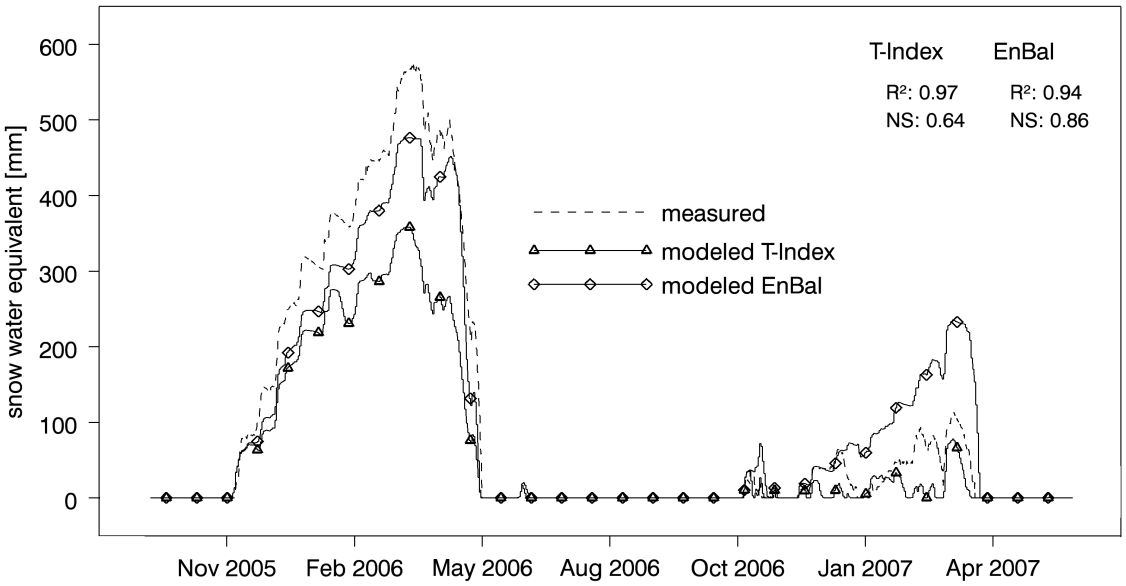

Figure 5.1: Seasonal snow cover evolution at the *Kühroint* station site (1407 m MSL) as modeled and recorded with a snow pillow during the winter seasons 2005/2006 and 2006/2007.

snow precipitation. SWE is increased and the sum of energy fluxes is negative. The small amounts of incoming advective energy on April 27 and 28 denote rainfall on the snow pack.

In addition to the SWE data at the station *Kühroint*, measurements of snow depth are available at several locations in the catchment. As the density of the snow cover and snow depth values are not computed by our model system, we compare SWE with measured snow depths to allow an evaluation of the dynamic behavior. Fig. 5.3 presents a comparison of measured snow depth and modeled SWE at six stations that cover an elevation range from 839 to 1900 m MSL for the winter seasons 2008/2009 and 2009/2010 to further validate the implemented energy balance approach and the general model setup.

The observed timing of first seasonal snowfall and melt out dates are well produced throughout this large elevation range by the model. At the station *Blaueis* (Fig. 5.3, e)) the snow cover melts off faster than observed resulting in an underestimated snow cover duration. This deviation might also be caused by the specific location of the station possibly measuring at a point with unrepresentatively large

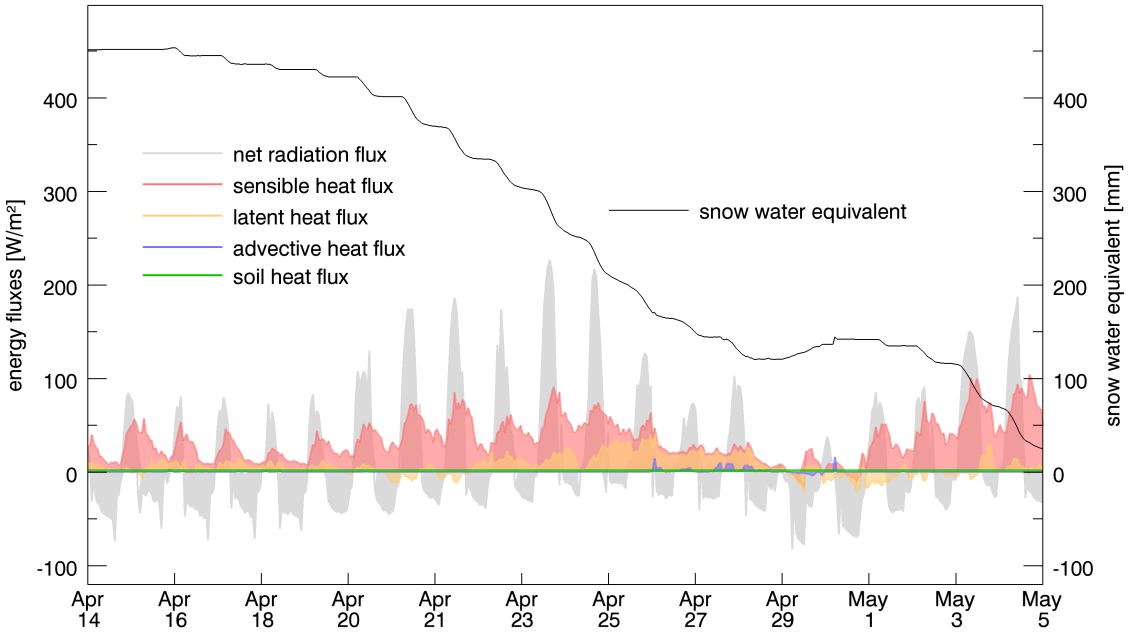

Figure 5.2: Modeled snow water equivalent in mm and energy fluxes in $W \cdot m^{-2}$ at the station *Kühroint* during the end of the melting season 2006.

snow amounts, as snow cover duration significantly differs from the other stations. The timing of single snowfall events are mostly modeled correctly. This can be seen from the corresponding time periods of increasing SWE and snow depth values. The short period of preseasonal snow coverage in October 2009 is reproduced at all stations where observations are available (Fig. 5.3, a, c, d, and e). The model seems to overestimate the amount of snow at the lowest elevated station *Hinterseeau* (Fig. 5.3, a). This can be explained by an underestimation of snowfall amounts and possibly by higher snow densities at the station characterized by warmer climatic conditions. Regarding the total catchment, snow cover duration and amounts are modeled with a satisfying performance, even though there are model errors at some stations. It is noted that there are uncertainties in this comparison induced by scale difference. The observations are valid for one specific point, whereas the modeled values represent a mean value of a cell with a surface area of 2500 m^2. Moreover, using the presented methods for spatial interpolation of meteorological forcing variables (Sec. 3.2), the measured driving data is not necessarily reproduced at a station during model runtime. Additionally, there are uncertainties when determining the precipitation phase (Eq. 4.1). As the used energy balance model is a relatively

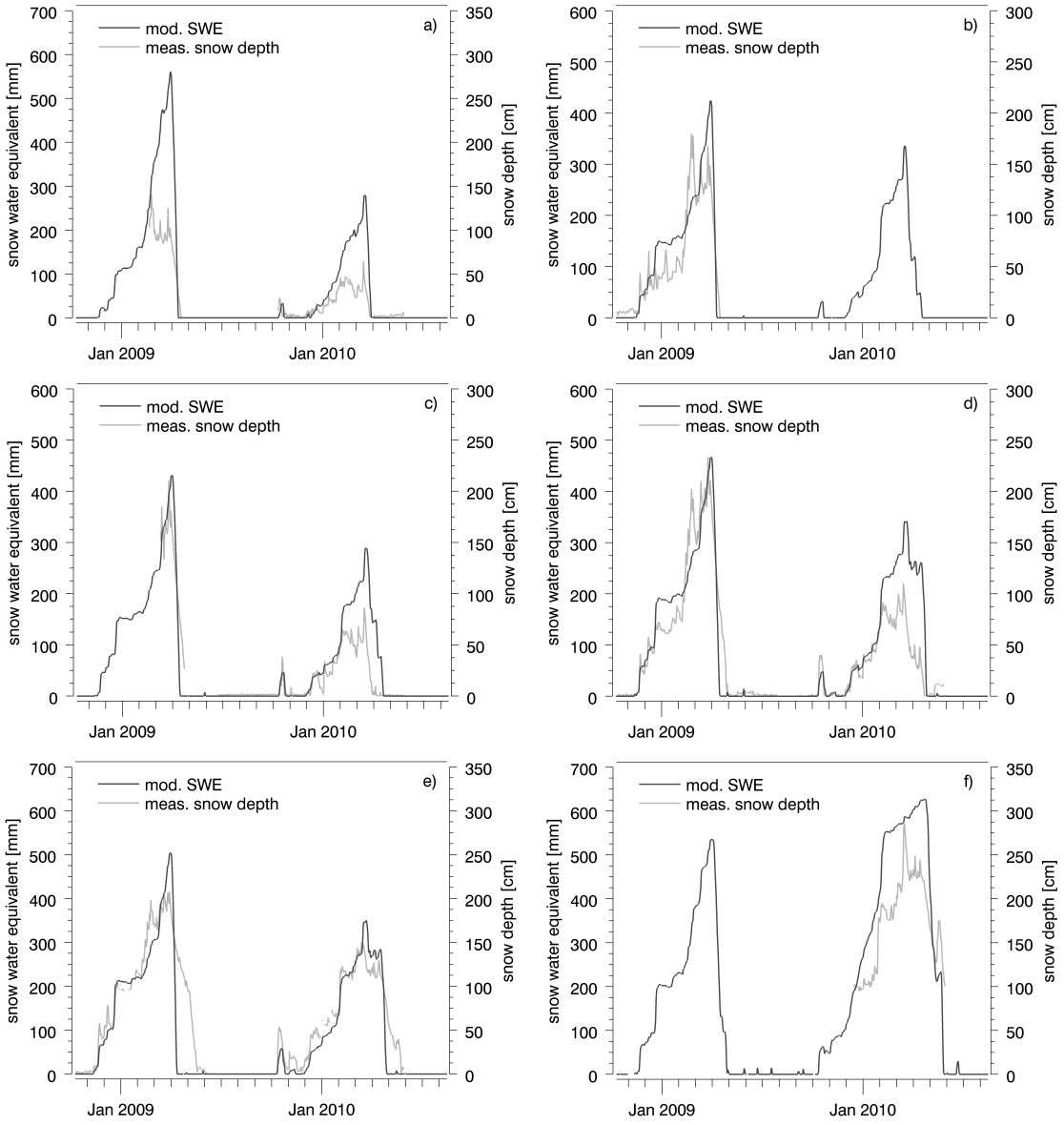

Figure 5.3: Comparison of seasonal modeled SWE evolution (energy balance approach without lateral redistribution) and measured snow depth values at 6 stations for the winter seasons 2008/2009 and 2009/2010. Stations are from top left to bottom right: a) *Hinterseeau* 839 m MSL, b) *Jenner 1219* m MSL, c) *Brunftbergtiefe* 1238 d) *Kühroint* 1407 m MSL, e) *Blaueis* 1651 m MSL, f) *Steinernes Meer* 1900 m MSL. For station b) and f), no data were available for 2008/2009, 2009/2010 respectively.

simple one layer approach using a proxy assumption (Sec. 4.2.1), future research may show if model performance can be improved by using a more complex energy balance approach or by using an even more complex multi-layer snow model.

5.2 Performance on the Catchment Scale

The modified snow module calculates the energy balance of the snow cover considering topography-dependent radiation fluxes as well as lateral snow transport processes. The scheme explicitly describes short- and long-wave radiation fluxes, turbulent latent and sensible heat exchange at the snow cover, advective energy by precipitation as well as a constant soil heat flux. It also accounts for mass changes accompanying the latent heat flux. This leads to a topography-driven distribution of snow ablation processes depending on exposure, slope, and shading effects.
The consideration of lateral snow transport processes covers two mechanisms: Snow redistribution by snow slides on very steep slopes and wind-induced snow transport. A simple mass-conserving approach was applied for the simulation of snow slides and a parameterization for the estimation of wind-induced snow transport based on an analysis of the DEM that extracts exposed and sheltered locations.

Gravitational Snow Transport As a result of introducing gravitational slides as described in Sec. 4.3.1, snow is removed from steep rock faces and accumulated at the base of the slopes. Erosion or ablation rates at the steepest slopes with highest snow precipitation reach up to 2023 mm SWE per winter. These areas are high elevated peaks with steep rock faces. The deposition rates are 2957 mm additional SWE per year at some locations. According ranges of gravitational snow redistribution were simulated by Strasser (2008) and Bernhardt & Schulz (2010). When the snow slide module is combined with the parameterization of wind-driven snow distribution, these maximal values increase to 4448 mm erosion and 3311 mm deposition (Fig. 5.4), because of higher incoming snow masses at the respective elevated steep slopes on leeward ridge sides. Fig. 5.5 illustrates that the locations of high accumulation amounts fit to remaining snow patches in summer observed on aerial images. The spatial distribution of snow cover duration (Fig. 5.6) accordingly

shows large values at these model cells.

Wind-driven Snow Redistribution Fig. 5.7 illustrates the amount of snow that is redistributed by the parameterization of wind-driven snow transport. In this study, the directed SVF is kept constant and was calculated for a sector of 90 degrees from south to west, which represents the main wind directions during winter season. The direction of the sector is based on a station analysis (not presented here) that matches an assessment by Konnert (2004). This constant directed SVF limits the redistribution structure to a constant field. Depending on data availability regarding main wind directions, the approach could be extended by implementing time-varying parameter fields. As described above, the redistribution is implemented as a correction of precipitation before the modeling process. It is important to know that this approach is not mass-conserving in the sense of eroded snow mass having to be equivalent to the deposited snow mass in total. Conservation of mass is not a prerequisite here, as the approach is to correct snow precipitation before the modeling process. This can be regarded as a sophisticated method of spatial interpolation of snow precipitation measured at the stations to the model grid. Such spatial interpolation methods in general are not mass-conserving. In this implementation, a pixel receives on average 27.8 mm additional snow precipitation per year (+5.2 % of total snow precipitation).
Slopes oriented to the prevailing wind direction sector, as well as high elevated ridges and peaks are windward locations and receive up to 1574 mm less snow precipitation per winter season. In contrast to this, sheltered regions at leeward locations facing the north-east gain additional snow precipitation of up to 3214 mm. The patterns and spatial distribution are similar to the results obtained by Bernhardt *et al.* (2010) in their study, and the values of redistribution are in a similar order. They model maximum gains of SWE by wind-induced snow transport of 2140 mm in a case study at the *Blaueisgletscher*. The amounts computed by the presented parameterization are higher and range up to 2634 mm at this location. Bernhardt *et al.* (2012) compare seasonal snowmelt differences between a model run with and without the consideration of lateral snow transport. They present a spatial distribution of values ranging from maximal losses of 1600 mm SWE to maximal gains of

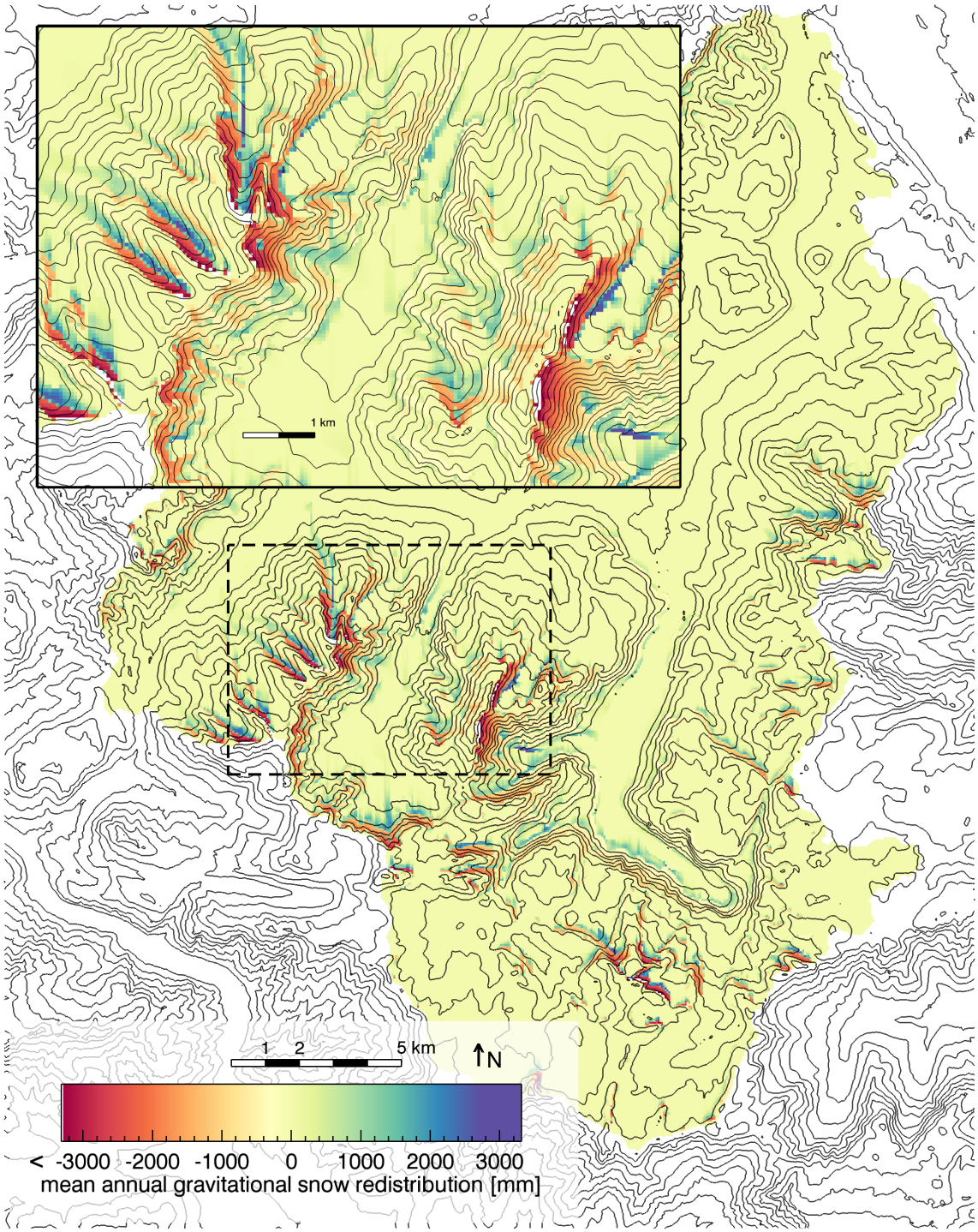

Figure 5.4: Simulated mean annual lateral snow redistribution by gravitational snow transport when additionally accounting for wind-driven redistribution (see details in the text). Red regions show erosion, and blue regions show accumulation zones. Minimum values range down to -4448 mm at very steep slopes with high snow precipitation. Contour lines denote elevation levels of 150 m (100 m in the enlarged view). The dashed rectangle demarcates the area shown in the enlarged view.

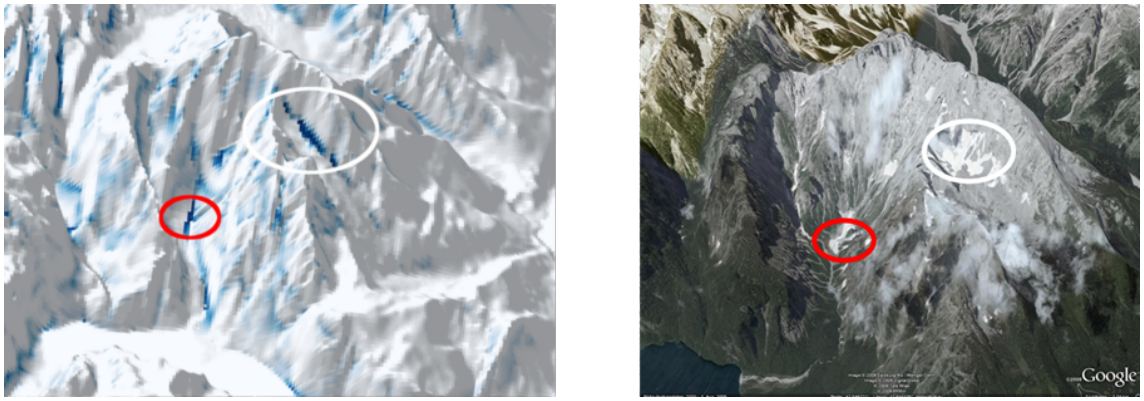

Figure 5.5: Deposited snow by gravitational transport during winter 05/06 (left) compared to remaining snow patches in summer on aerial imagery (right). Highlighted are two locations of large accumulation values, which correspond to the perennial firn field *Eiskapelle* (red mark) and the small glacier *Watzmanngletscher* (white mark).

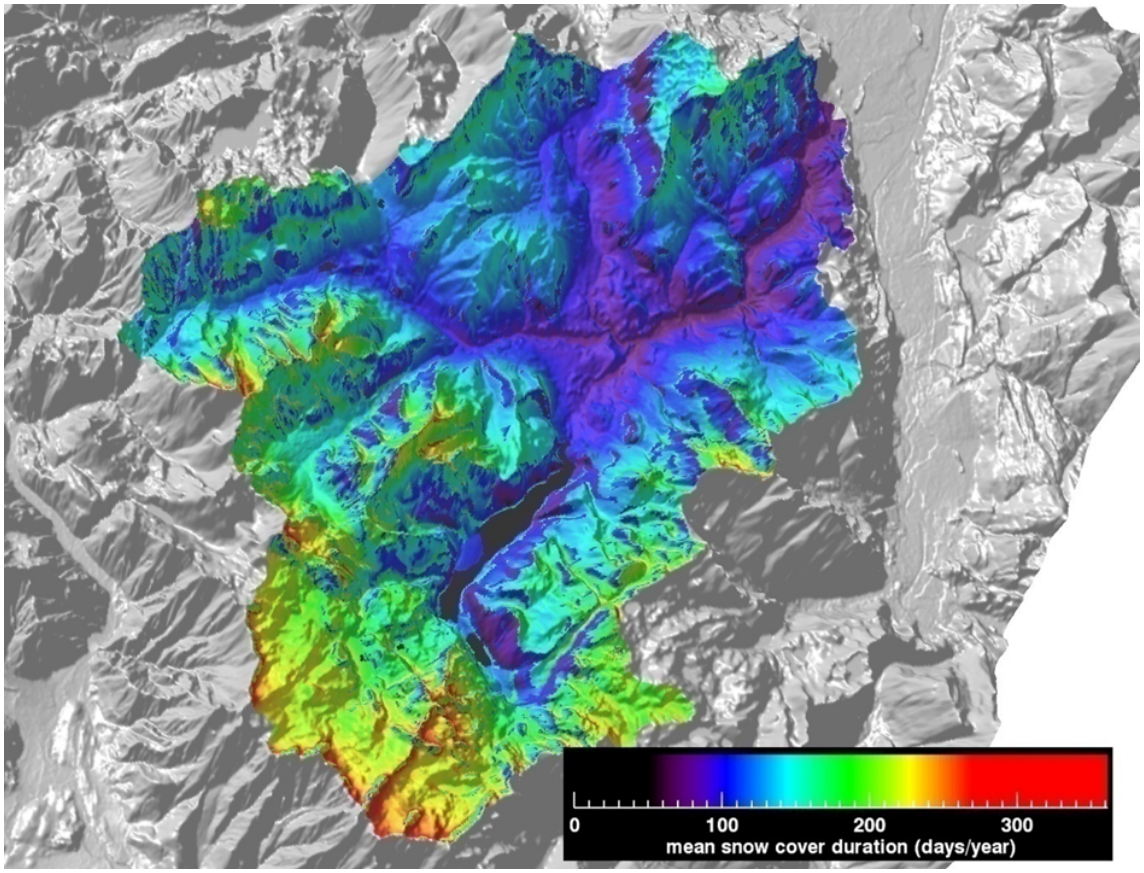

Figure 5.6: Mean snow cover duration per year (2002-2007) including the simulation of gravitational snow transport.

5000 mm by simulating lateral snow processes. In the same comparison, we assess similar values of maximal 1989 mm losses and maximal 5155 mm gains in seasonal snowmelt distributed in a matching spatial pattern.

Energy Balance Approach Calculated with the temperature index method, snow cover evolution depends on the precipitation amount and air temperature and therefore, its duration increases with elevation. The energy balance approach in combination with lateral redistribution processes results in an exposition-dependent snow cover duration with a maximum at high elevated, northern-oriented, shaded, and sheltered areas at the foot of steep faces (Fig. 5.10), where the accumulation is large due to high snowfall rates and incoming mass from snow slides and the energy input for ablation by solar radiation and sensible heat is limited.
Fig. 5.8 illustrates the differences between the snow pack development simulated by means of a temperature index model and that modeled by the energy balance calculation, both without accounting for lateral snow transport. The range in gain and loss of snow cover duration is significant. The values range from 58 days less snow coverage per year to additional 45 snow-covered days at certain locations on average. The respective percentage change of snow cover duration at each cell is displayed in Fig. 5.8 and ranges from -18% to +50%. The maximal losses in modeled snow cover duration can be found at high elevated, southern oriented ridge sites because of the explicitly modeled incoming radiation energy. When using a temperature index approach, melting is underestimated particularly in high elevated, south-facing slopes with high radiation energy input and small average air temperatures.

Energy Balance Approach and Lateral Processes The effects of additionally accounting for lateral transport processes are shown in Fig. 5.9, which presents the percentage change in snow cover duration by introducing the simulation of gravitational slides and wind-driven snow redistribution. Values range from -59% to +34% of change in mean snow cover duration. The maximal absolute changes are a reduction of 77 days per season and an increase of 57 days at certain cells. The maximal losses in modeled snow cover duration can be found at high elevated, exposed, steep

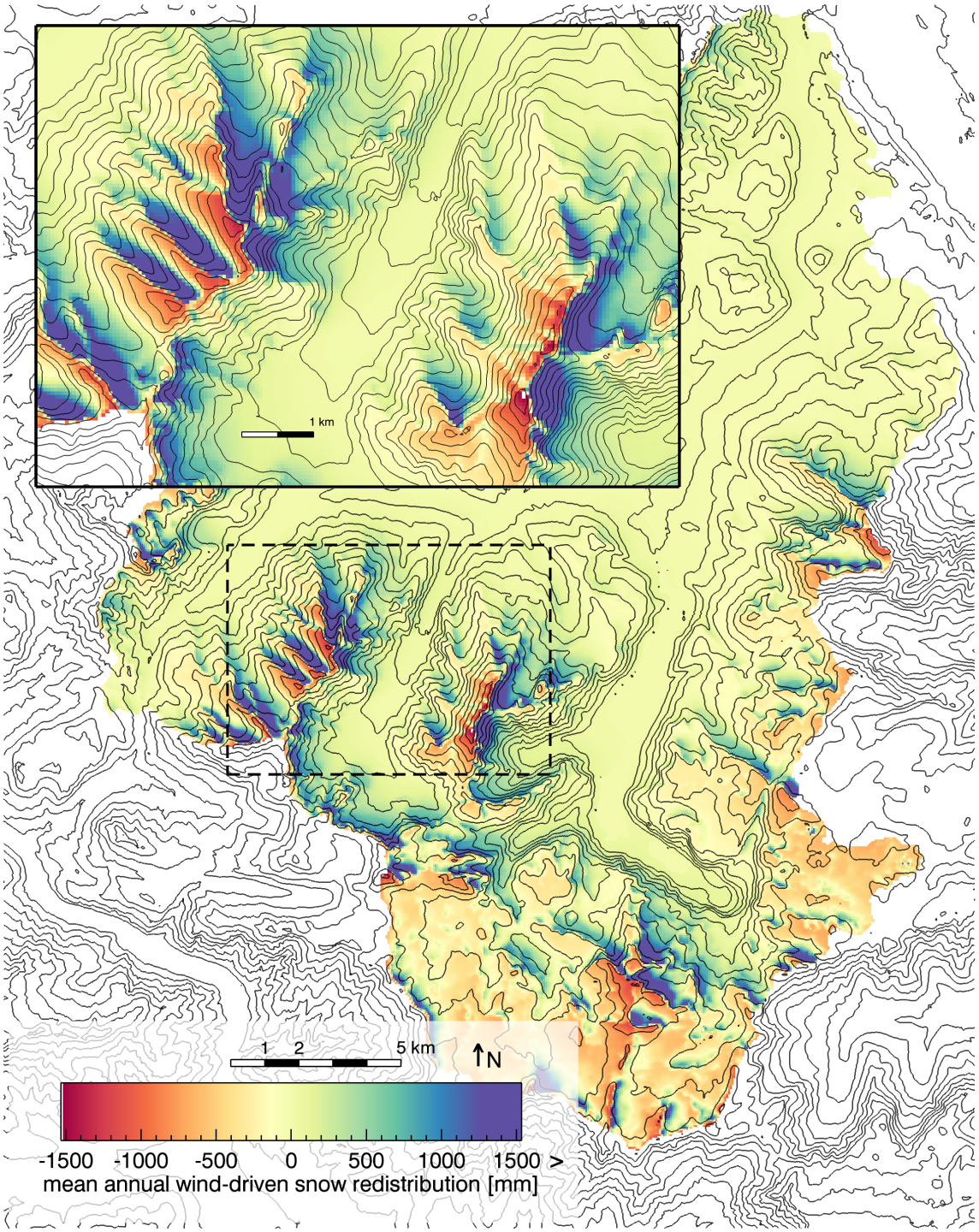

Figure 5.7: Simulated mean annual lateral wind-driven snow redistribution. Main wind directions is south-west. Red regions show erosion, and blue regions show accumulation zones. Maximum values range up to 3214 mm, but are limited to small, high elevated, leeward locations. Contour lines denote elevation levels of 150 m (100 m in the enlarged view). The dashed rectangle demarcates the area shown in the enlarged view.

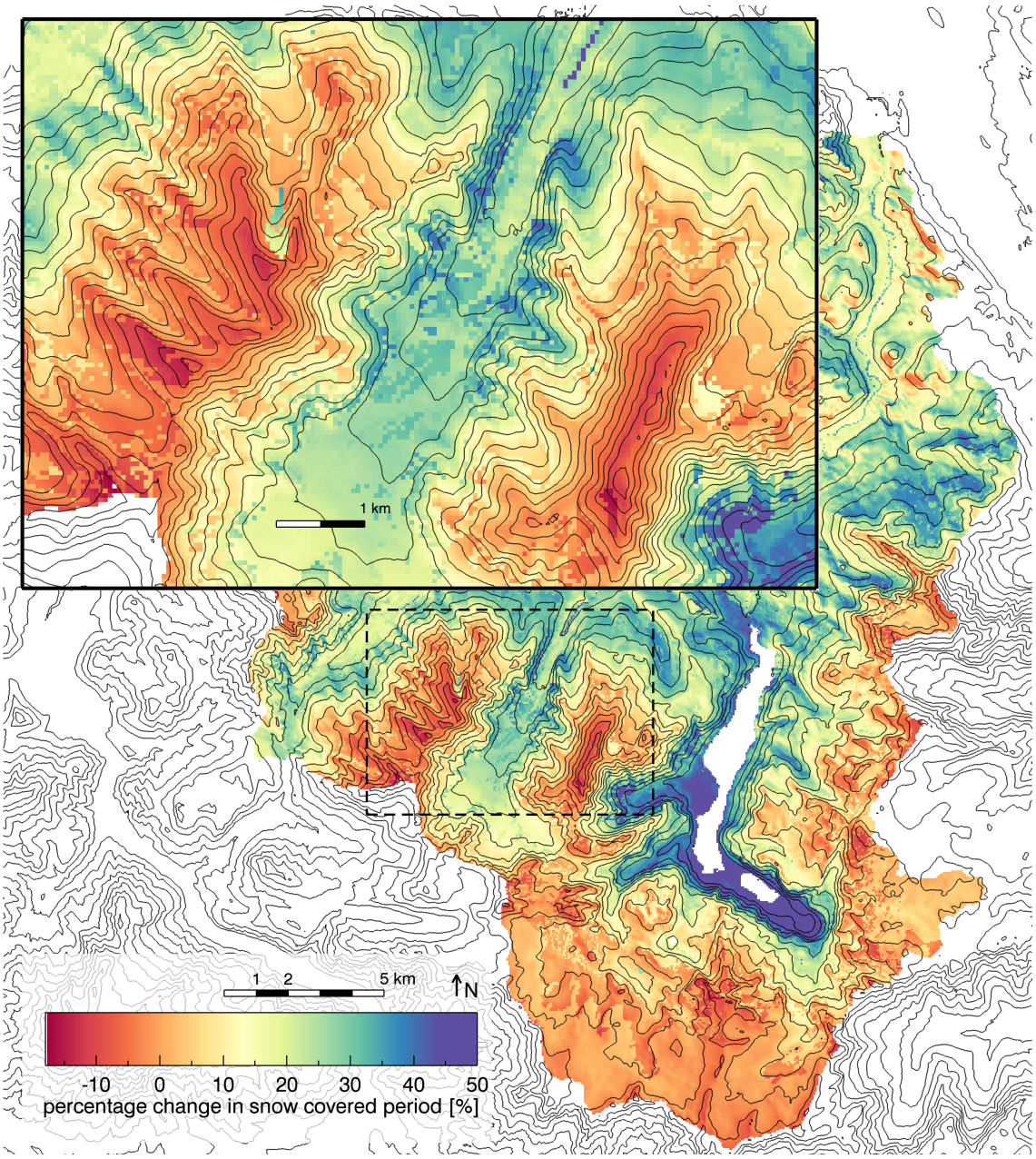

Figure 5.8: Difference in modeled mean annual snow cover duration between temperature index (TI) and energy balance (EB) approach (percentage change EB - TI). Contour lines denote elevation levels of 150 m (100 m in the enlarged view). The dashed rectangle demarcates the area shown in the enlarged view.

ridge sites that are oriented to the main wind direction. These areas are blown free of snow by wind and lose snow masses by gravitational slides. The maximal gains in snow-covered days are located at leeward ridge sites and at the foot of steep faces, where snow is transported to by the snow slide algorithm.

In summary, maximum values of snow cover duration appear at the base of steep slopes, where the snow mass input is significantly increased by lateral transport mechanisms (Fig. 5.10). Moreover, these locations are often shaded by surrounding steep faces. Low elevated, northern-oriented, shaded slopes generally show an increased snow cover duration when using the energy balance approach, independently of snow input by lateral transport (Fig. 5.8). This is due to the consideration of the reduced radiative energy income in that locations. In contrast to this, the temperature index approach determines snow cover duration independently of exposure, if it is not implied in air temperature interpolation routines. The areas with a maximum snow cover duration of nearly 360 days per season (Fig. 5.10) fit the locations where the perennial firn fields and glaciers are situated in the catchment (*Schöllhorneis*, *Eiskapelle*, *Watzmanngletscher*, and *Blaueisgletscher*). These realistic maximum values and particularly correct locations are not simulated by using the simple temperature index routine.

5.3 Spatial Validation

A comparison of modeled SWE and Landsat ETM+ imagery classification is shown in Fig. 5.13. To validate the implemented snow model approaches, observed and modeled snow coverage are compared on three specific dates of data recording. The choice of the dates was mainly restricted by data availability and cloud-free conditions. The Normalized Difference Snow Index NDSI (Dozier, 1989; Hall *et al.*, 1995) is used to classify the satellite observations into snow and no-snow areas. The NDSI makes use of the special reflectance properties of snow. The reflectivity of snow is very high in visible wavelengths and low in the near infrared range, whereas the reflectivities of e.g. clouds, dry soils, or bare rocks are high in the near infrared and e.g. water and vegetation are characterized by low reflectivities in the visible

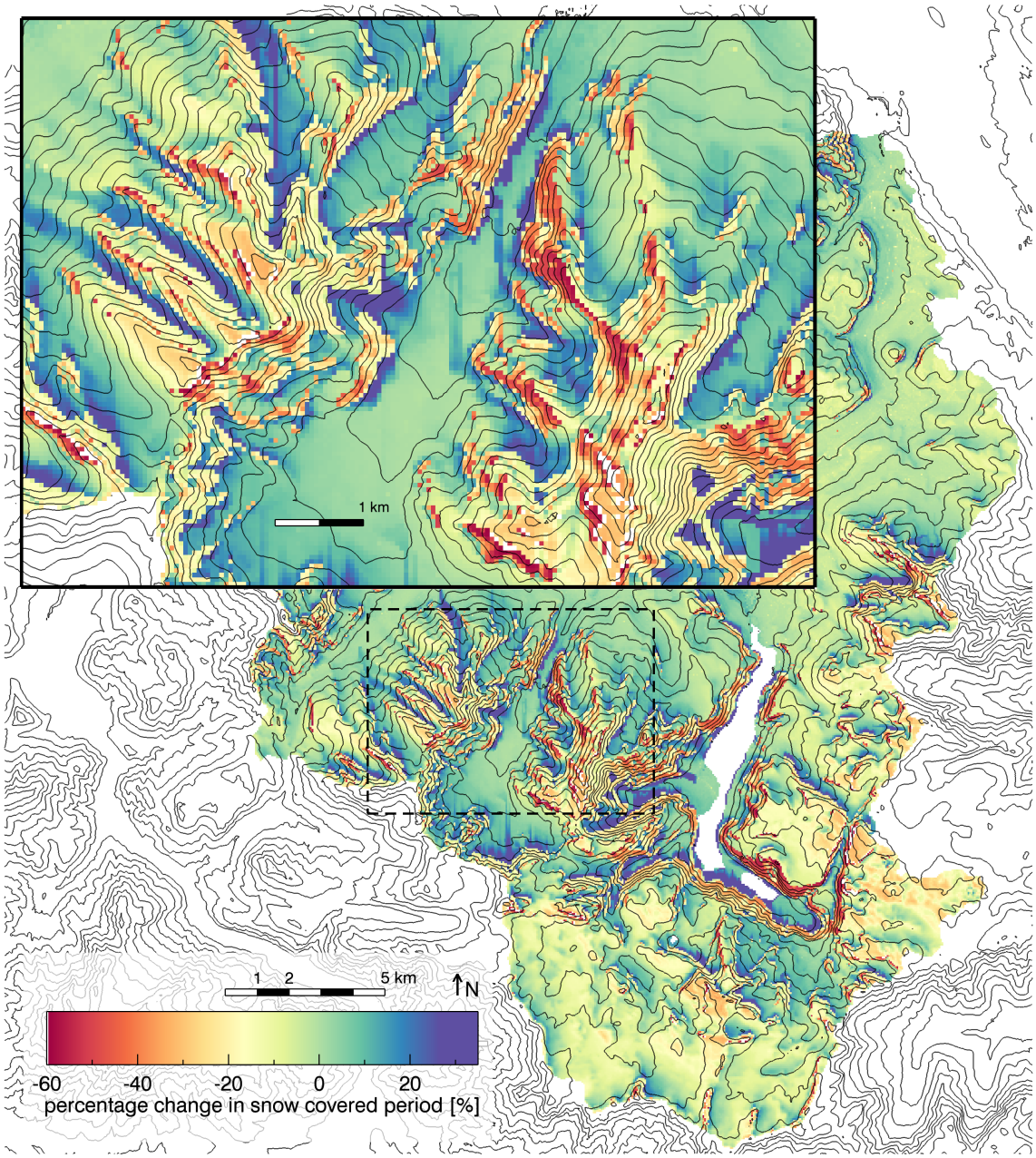

Figure 5.9: Difference in modeled mean annual snow cover duration due to lateral snow transport (percentage change 'EB and lateral redistribution' - 'EB without lateral redistribution'). Contour lines denote elevation levels of 150 m (100 m in the enlarged view). The dashed rectangle demarcates the area shown in the enlarged view.

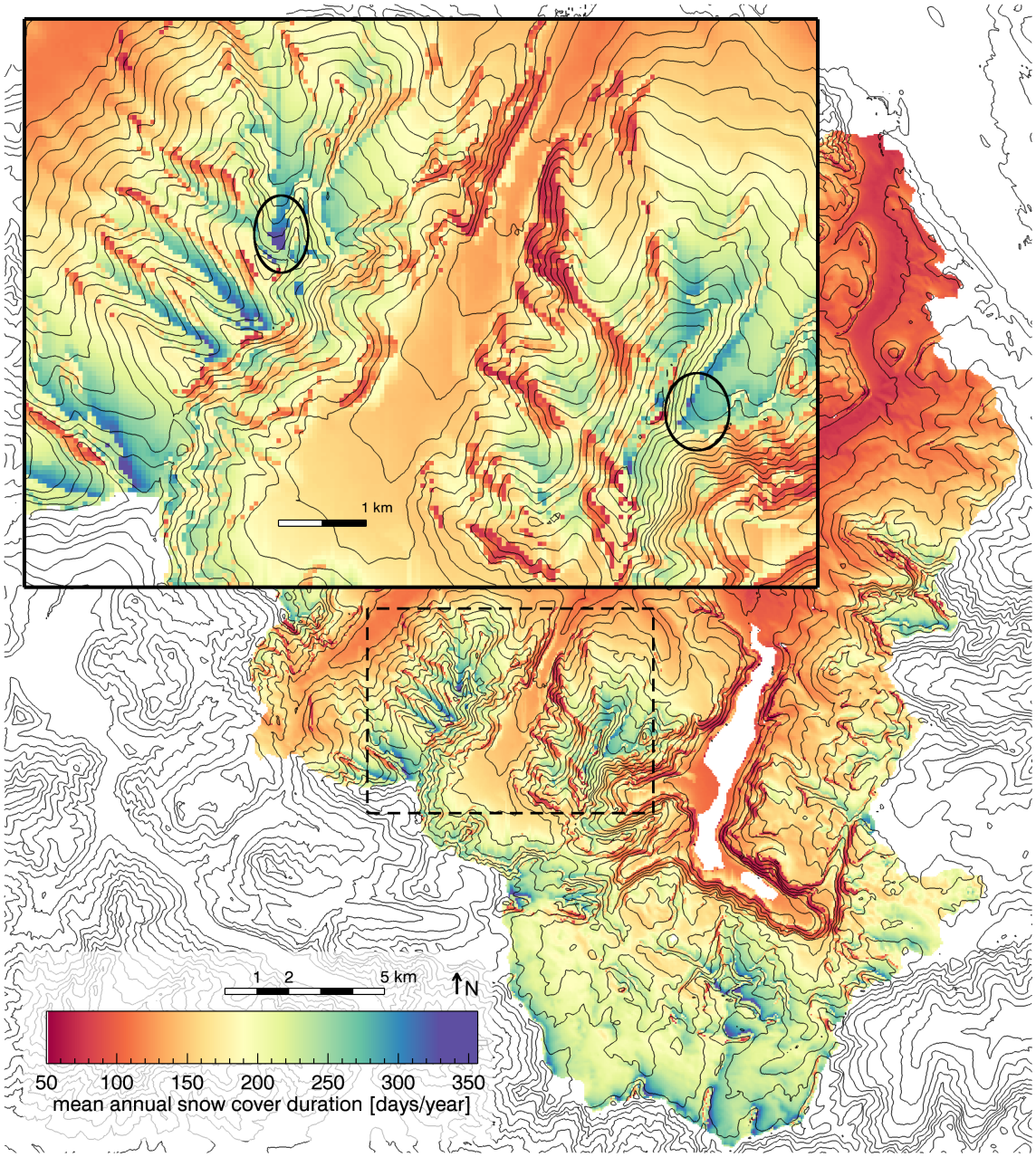

Figure 5.10: Modeled mean annual snow cover duration using the energy balance approach and simulating lateral redistribution of snow. Contour lines denote elevation levels of 150 m (100 m in the enlarged view). The dashed rectangle demarcates the area shown in the enlarged view. The locations of the two small glaciers in the catchment that are referred to in the text are indicated.

spectrum. NDSI is defined as

$$NDSI = \frac{\rho_{VIS} - \rho_{NIR}}{\rho_{VIS} + \rho_{NIR}} \tag{5.1}$$

with ρ_{VIS} being the reflectance in the visible and ρ_{NIR} in the near infrared range of the electromagnetic spectrum. For the application using the data recorded by the Landsat sensor Enhanced Thematic Mapper (ETM+), the spectral band 2 (wavelength 0.52-0.60 µm) was used as visible channel, and the band 5 (wavelength 1.55-1.75 µm) for the near infrared reflectance.
The NDSI was extracted from the Landsat ETM+ data which is available in a horizontal resolution of 30 m and was interpolated to match the 50 m model grid. The threshold of 0.4 (Dozier, 1989) is used as a lower boundary of NDSI to identify snow covered pixels.

A comparison of NDSI and modeled mean snow cover duration is shown in Fig. 5.11. This qualitative assessment shows that the general spatial structure of snow coverage as well as small scale patterns of high snow accumulation areas are well captured by the model. Fig. 5.12 compares the snow coverage on May 01, 2005 as classified from the Landsat ETM+ scene, to the modeled coverage using the temperature index approach, and the energy balance calculation including lateral redistribution. It is clearly seen that the snow coverage modeled by the temperature index approach shows a sharp, distinct line induced by the elevation-dependent characteristics of the temperature and precipitation interpolation. The energy balance calculation together with the lateral redistribution results in a pattern that is refined on small scales and represents a more realistic image. Fig. 5.13 shows the full NDSI range above the threshold. Cells having NDSI values below the threshold are indicated in grey color. The probability of the existence of snow in a pixel increases with higher NDSI values. As there are still uncertainties in classifying snow in the Landsat ETM+ data and particularly in the distinction between snow and rock in shaded locations, this probability map is shown in addition to the definite snow or no-snow decision. Matching Figs. 5.10 and 5.13, the small-scale regions with high incoming snow masses by gravitational slides, as well as snow- free ridges can be identified clearly in the observed and modeled images. A percentage of cells that

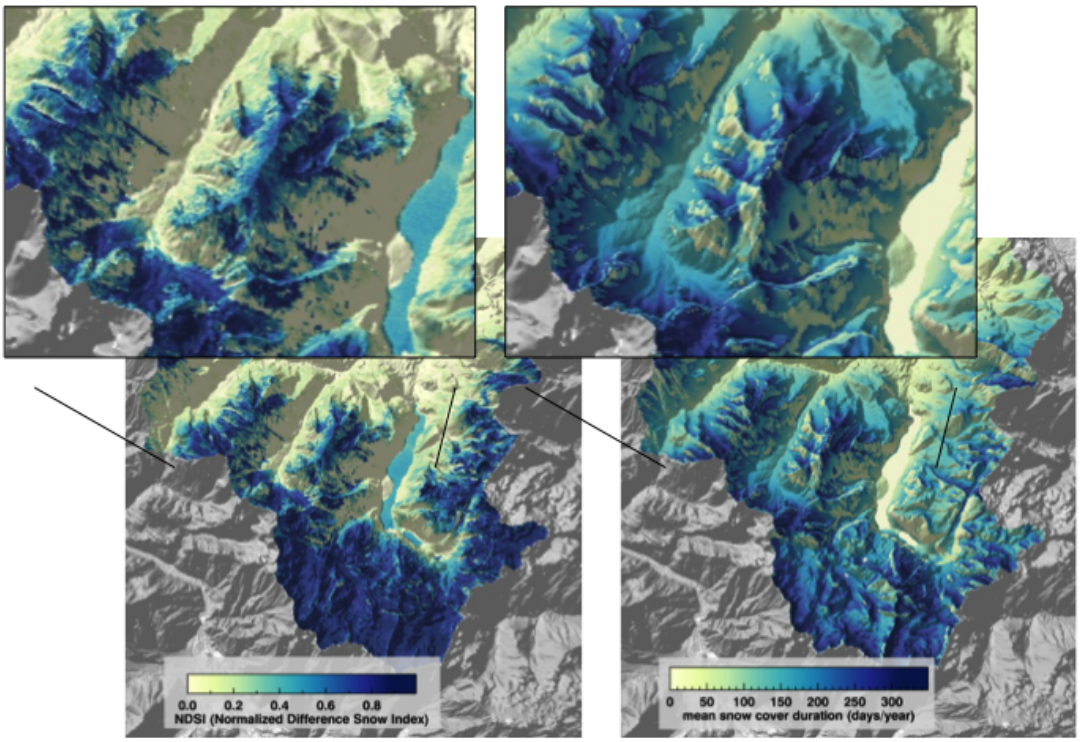

Figure 5.11: Comparison of spatial patterns of NDSI (left, May 01, 2005) and modeled mean snow cover duration using the energy balance calculation including lateral redistribution (right).

are in agreement in the Landsat ETM+ NDSI classification and the modeled field of snow coverage was calculated (Tab. 5.1). The performance for the region shown in Fig. 5.13 ranges from 71.1 to 82.5%, and for the entire catchment from 82.5 to 89.5% at the different dates analyzed. The higher values for the entire catchment can be explained by a large area being free of snow in the lower elevations.

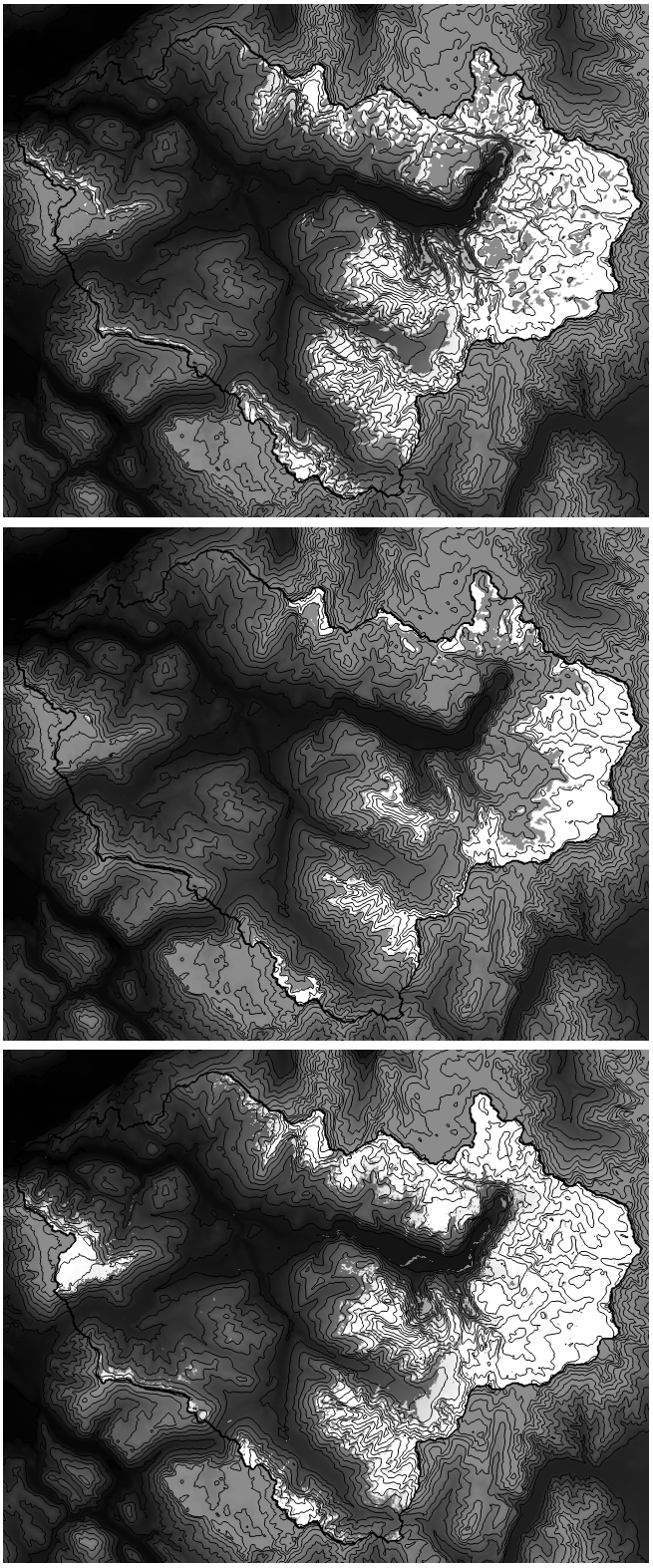

Figure 5.12: Snow coverage (white) on May 01, 2005 based on NDSI extracted from a Landsat-ETM+ scene (left, see details in the text), modeled using the temperature index approach (middle), and modeled using the energy balance calculation including lateral redistribution (right). The black line delineates the modeled catchment.

Table 5.1: Percentage of cells that are in agreement in the Landsat ETM+ classification and the modeled field of snow coverage (energy balance calculation and lateral snow transport) at three different dates for the summit section depicted in Fig. 5.13 and the entire catchment.

	April 07, 2002	May 30, 2004	May 01, 2005
summit section	71.1	82.5	72.5
total catchment	84.0	89.5	82.5

To further quantify the spatial analysis, additional performance indices are presented in the following. The model of indices was introduced by Aronica *et al.* (2002), and applied by e.g. Hunter *et al.* (2005) and Bernhardt *et al.* (2012). The equations to compute the performance measures $F^{\langle 1\rangle}$, $F^{\langle 2\rangle}$, and $F^{\langle 3\rangle}$ are:

$$F^{\langle 1\rangle} = \frac{\sum_{i=1}^{n} a + \sum_{i=1}^{n} d}{n} \tag{5.2}$$

$$F^{\langle 2\rangle} = \frac{\sum_{i=1}^{n} a}{\sum_{i=1}^{n} a + \sum_{i=1}^{n} b + \sum_{i=1}^{n} c} \tag{5.3}$$

$$F^{\langle 3\rangle} = \frac{\sum_{i=1}^{n} a - \sum_{i=1}^{n} b}{\sum_{i=1}^{n} a + \sum_{i=1}^{n} b + \sum_{i=1}^{n} c} \tag{5.4}$$

with a, b, c, and d describing different combinations of modeled and observed binary patterns and n the number of pixels. The specific meanings of a, b, c, and d in this assessment are listed in Tab. 5.2.

Tab. 5.3 presents the results for $F^{\langle 1\rangle}$ - $F^{\langle 3\rangle}$ for the entire catchment and the three dates shown in Fig. 5.13. All three indices are 1 if the modeled snow coverage perfectly matches the observed one. $F^{\langle 1\rangle}$ shows the same values as the percentage evaluation presented above (Tab. 5.1) as fractions of 1. This performance index includes all pixels including the case d which represents pixels that are snow free in the model and in the observations. Since there are large areas that are low elevated

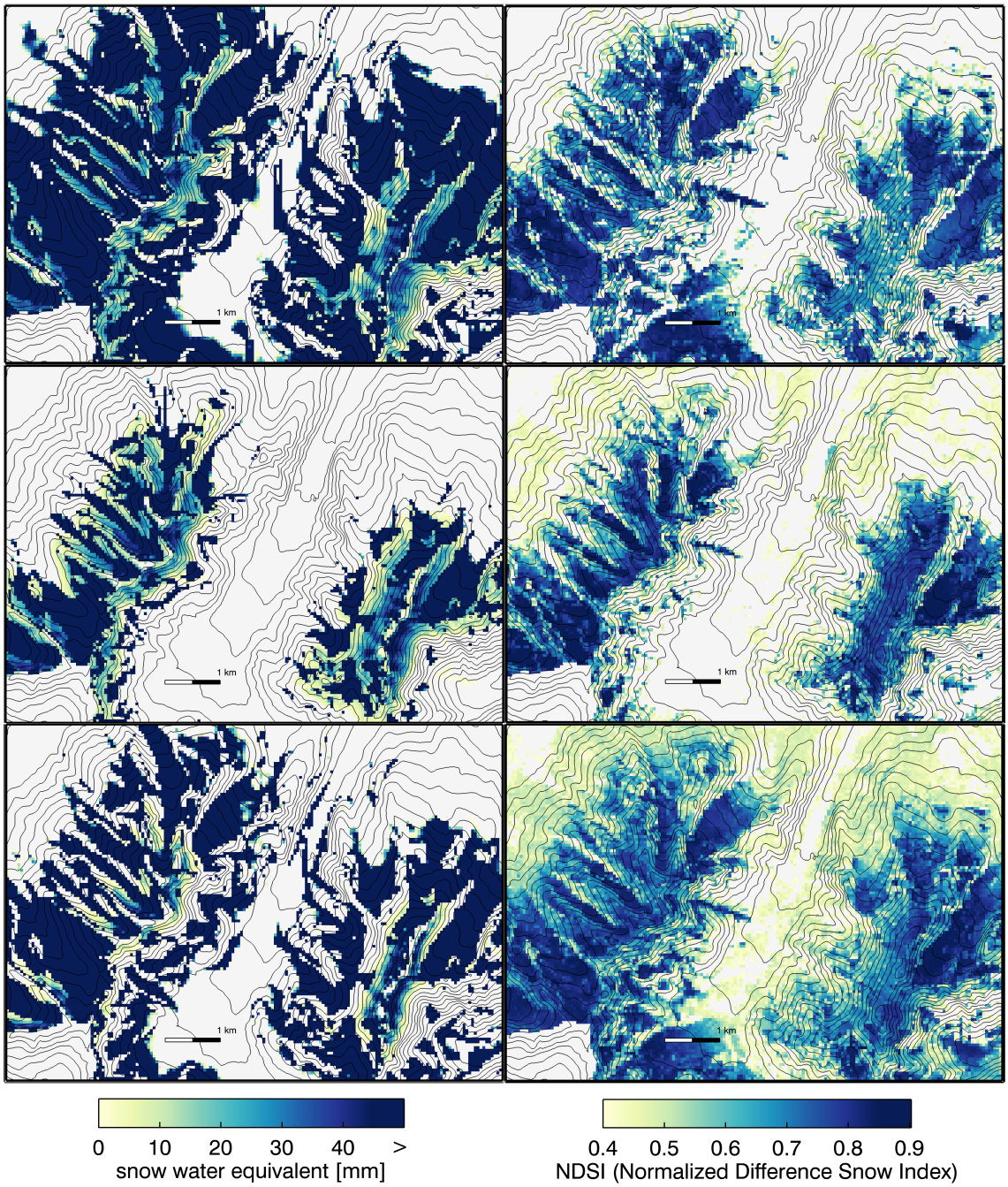

Figure 5.13: Modeled snow water equivalent using the energy balance calculation including lateral snow transport (left) compared to NDSI (right) from top to bottom on April 07, 2002, May 30, 2004, and May 01, 2005. NDSI was extracted from Landsat-ETM+ scenes (see details in the text). SWE on the according dates is shown on the left with saturation of the color scale at 50 mm to reveal spatial details at locations with low SWE values. Snow free pixels are presented in grey color. Percentage of cells that match between observation and model are from top to bottom 71.1, 82.5, and 72.5%.

Table 5.2: Contingency table listing the parameters used in Eqs. 5.2 - 5.4.

	obs. snow	*obs.* no snow
mod. snow	a	b
mod. no snow	c	d

Table 5.3: Performance indices (Eqs. 5.2 - 5.4) for the three evaluation dates comparing Landsat ETM+ NDSI classification and modeled fields of snow coverage (energy balance calculation and lateral snow transport).

	April 07, 2002	May 30, 2004	May 01, 2005
$F^{\langle 1 \rangle}$	0.84	0.90	0.83
$F^{\langle 2 \rangle}$	0.68	0.62	0.56
$F^{\langle 3 \rangle}$	0.51	0.48	0.42

and snow free in the NDSI classification as well as in the model simulation, this performance measure shows the highest values. $F^{\langle 2 \rangle}$ and $F^{\langle 3 \rangle}$ exclude these pixels and accordingly result in lower values. Generally, the performance is similar at the three dates representing spring snow coverage after three different winter seasons. Values for $F^{\langle 1 \rangle}$ range from 0.83 to 0.90, for $F^{\langle 2 \rangle}$ from 0.56 to 0.68, and for $F^{\langle 3 \rangle}$ from 0.42 to 0.51. These values are in the same range as assessed by Bernhardt *et al.* (2012) in their study for one specific date.

The spatial distribution of snow coverage is refined by implementing the new snow model methods, resulting in a good agreement of modeled and observed snow distribution for simulations on the regional and catchment scale. However, a perfect match between modeled and real snow coverage or even SWE should not be expected, as some processes have not been addressed in the formulations, e.g. interaction between vegetation and snow or lateral heat exchange, and due to simplifications, restrictions in spatial resolution, and additional uncertainties, e.g. when measuring snow precipitation at the stations and spatially interpolating model input in the domain.

5.4 Effects on Runoff Generation and Streamflow Dynamics

The different modeling approaches produce differing snowmelt and runoff dynamics. Fig. 5.14 shows the modeled and measured runoff in m^3s^{-1} at the gauge *Hintersee* from February 2006 to July 2006, Fig. 5.15 for the same period in 2007. February to July is the period, when snowmelt plays a significant role in runoff generation in the region. Figs. 5.14 and 5.15 additionally display modeled rainfall and snowmelt rates in mm for the catchment. In this way, snowmelt- and rainfall-triggered runoff events can be distinguished clearly.

Energy Balance Approach A major effect of introducing the energy balance calculation regarding catchment runoff is the production of daily fluctuations in the snowmelt rates that trace down to the channel stream. This daily cycle of snowmelt and consequent runoff rates could not be reproduced by the temperature index approach (Fig. 5.14 and Fig. 5.16, April). As the temperature index model is also run on an hourly basis, there are daily cycles as well, but the magnitudes are much smaller compared to the energy balance calculation. Directly modeling the impact of incoming radiation energy leads to more pronounced melting peaks. These melting peaks promote more clearly to runoff peaks in channel streamflow when routing the water to the gauges.

During the winter, there are various discharge peaks in the simulations that cannot be observed in reality (Fig. 5.14, February, temperature index). These peaks do not occur when using the energy balance approach. This effect can be explained by air temperature exceeding the defined limit for melting conditions in Eq. 4.2 for short periods. Melting occurs even if the available energy input is not able to melt snow, because it is used to warm up the cold snow pack. These cases are identified by the energy balance approach where the available energy input is determined explicitly. Consequently, the respective runoff peaks vanish (Fig. 5.14, February). In contrast, a small runoff peak at the beginning of March was not modeled properly by the energy balance method and overestimated by the temperature index calculation. Total melting and runoff rates are highest in the spring months from March

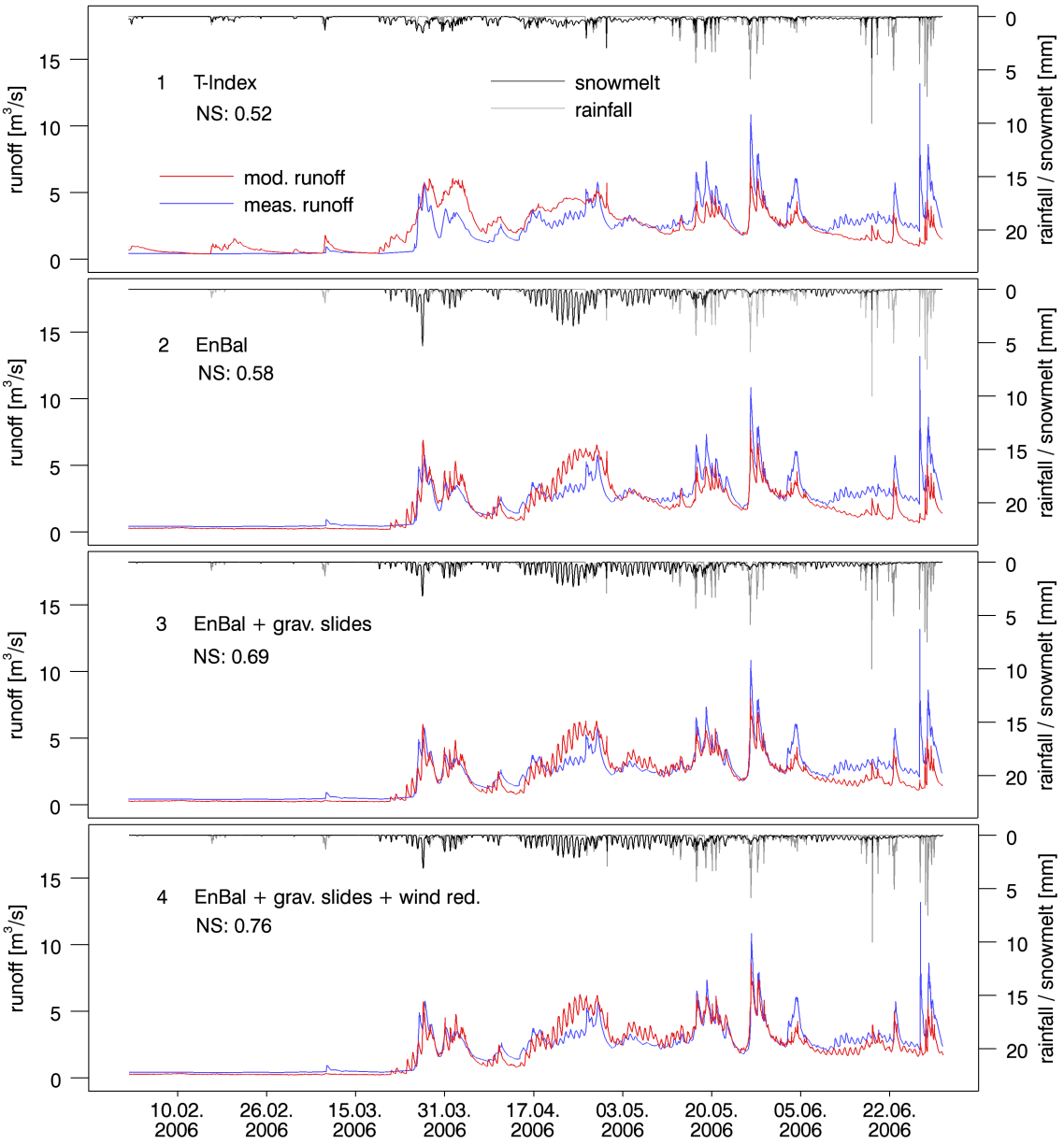

Figure 5.14: Modeled and measured runoff at gauge *Hintersee* from February to June 2006 and according Nash-Sutcliffe coefficients (NS). Increasing snow model complexity from top to bottom: 1 temperature index, 2 energy balance, 3 energy balance and snow slides, 4 energy balance, snow slides, and wind redistribution.

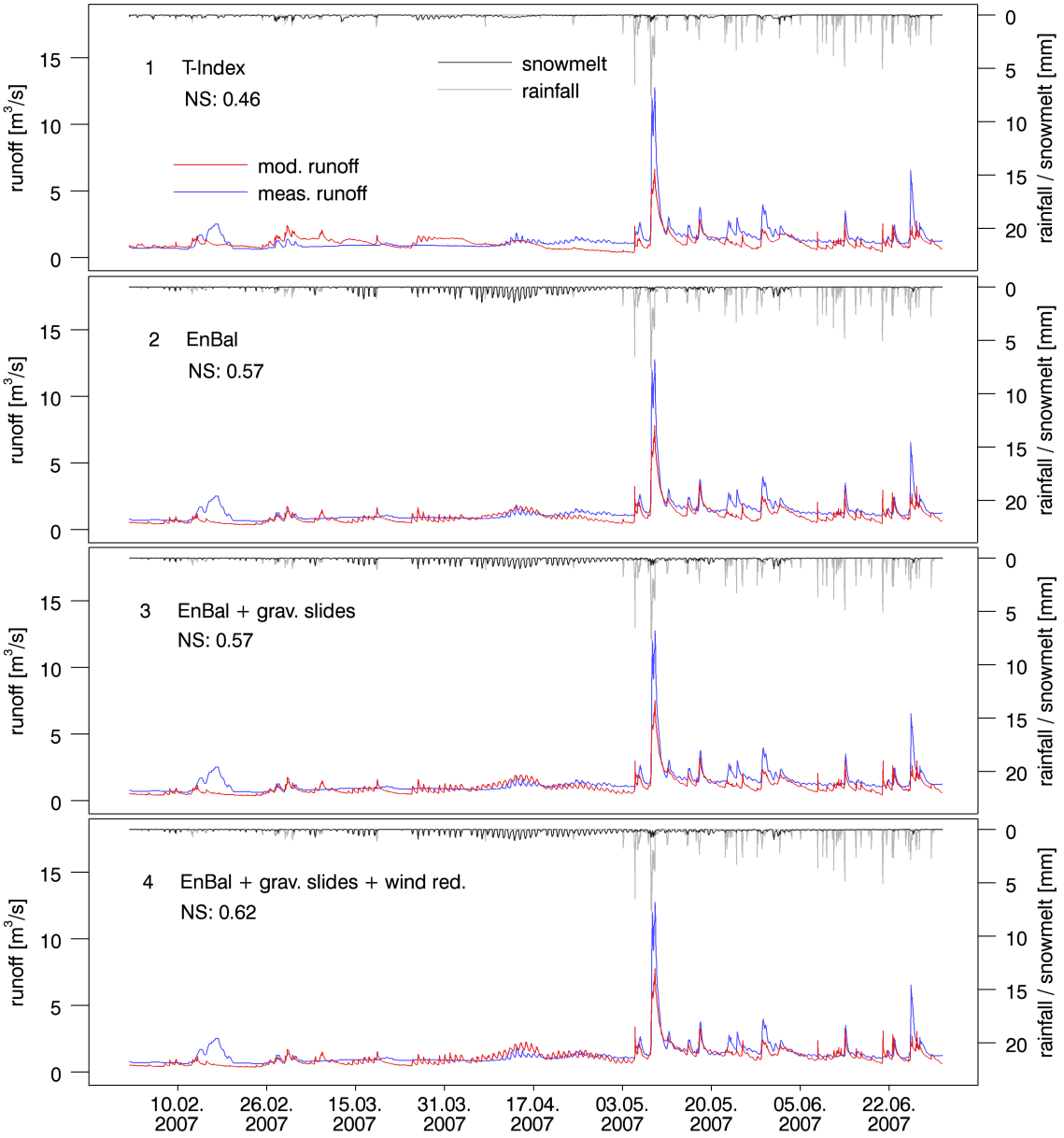

Figure 5.15: Modeled and measured runoff at gauge *Hintersee* from February to June 2007 and according Nash-Sutcliffe coefficients (NS). Increasing snow model complexity from top to bottom: 1 temperature index, 2 energy balance, 3 energy balance and snow slides, 4 energy balance, snow slides, and wind redistribution.

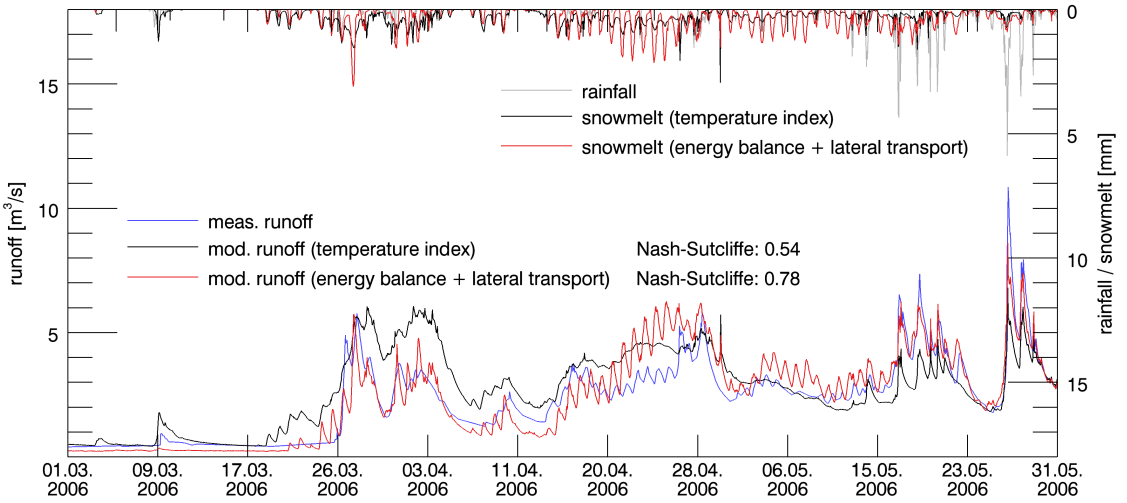

Figure 5.16: Modeled and measured (blue) runoff at gauge *Hintersee* from March to May 2006 and according Nash-Sutcliffe coefficients (NS). Snow cover is modeled using the temperature index approach (black) and the energy balance method including lateral transport (red).

to May. Analyzing mean snowmelt totals per month (Fig. 5.17) reveals a clear shift of simulated snowmelt from summer, autumn, and early winter months to early and late spring months by using the energy balance approach. At the gauge *Hintersee*, the NS coefficient for runoff model performance rises from 0.52 to 0.58 during this period when using the energy balance approach (Fig. 5.14). For the whole period modeled, the coefficient increases from 0.57 to 0.62 and the mean coefficient of all gauges from 0.62 to 0.63 (Tab. 5.4).

The following melting season 2007 (Fig. 5.15) shows the result of a winter season with different meteorological conditions, generally with smaller amounts of snow (Fig. 5.1) and the snow cover melting off several times during midwinter over large areas of the catchment. Results are similar to the year 2006, though a runoff peak in February was not captured by the model. This is probably due to a precipitation event in the subcatchment that was not measured by the meteorological stations. The daily fluctuations in snowmelt and runoff are overestimated in some periods by the energy balance calculation during March and April. The NS coefficient increases from 0.46 to 0.57 in the melting season 2007 when using the energy balance calculation instead of the temperature index approach (Fig. 5.15).

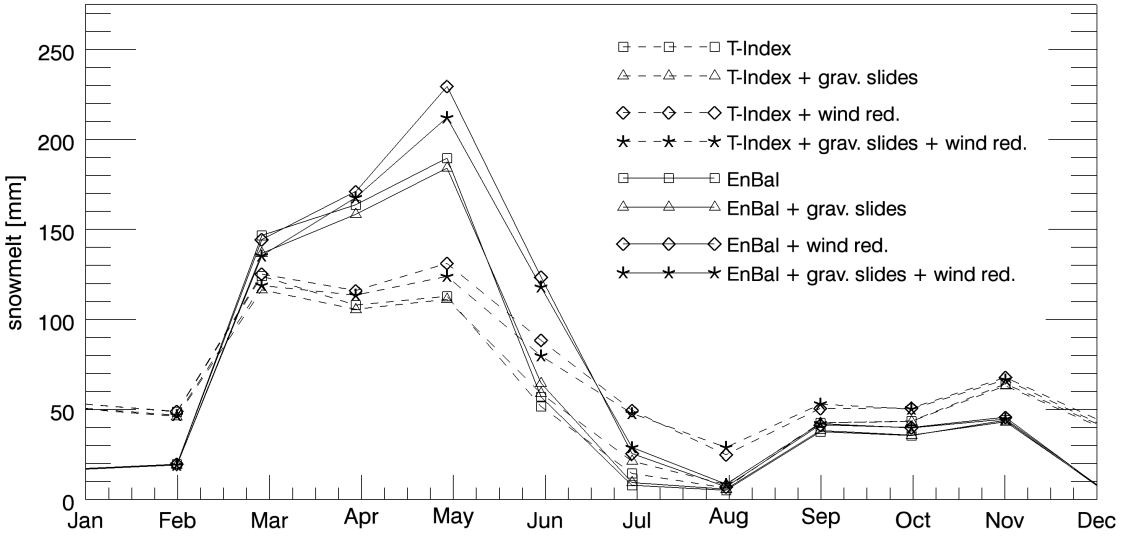

Figure 5.17: Mean monthly snowmelt sums (2002-2007) simulated by means of different combinations of snow modeling methods.

Table 5.4: Mean Nash-Sutcliffe coefficients at the gauge *Hintersee*, for the mountainous headwater catchments and for all subbasins (total) for the period 2002-2007.

Snow module	*Hintersee*	headwater catchments	total
T-index	0.57	0.46	0.62
EnBal	0.62	0.49	0.63
EnBal + grav. slides	0.65	0.51	0.64
EnBal + grav. slides + wind red.	0.68	0.52	0.64

Gravitational Snow Transport Accounting for gravitational snow transport generally shifts runoff from early spring to late spring. This can be explained by those snow masses that slide down and accumulate at shaded locations. These are compact, spatially limited areas with very high amounts of incoming snow. They can be identified in Figs. 5.4 and 5.10 at the base of steep faces where the terrain flattens out. This water storage concentrated on fewer snow covered cells with large amounts of snow needs time to melt off completely and therefore still produces runoff later in the season. The introduction of gravitational snow transport reduces

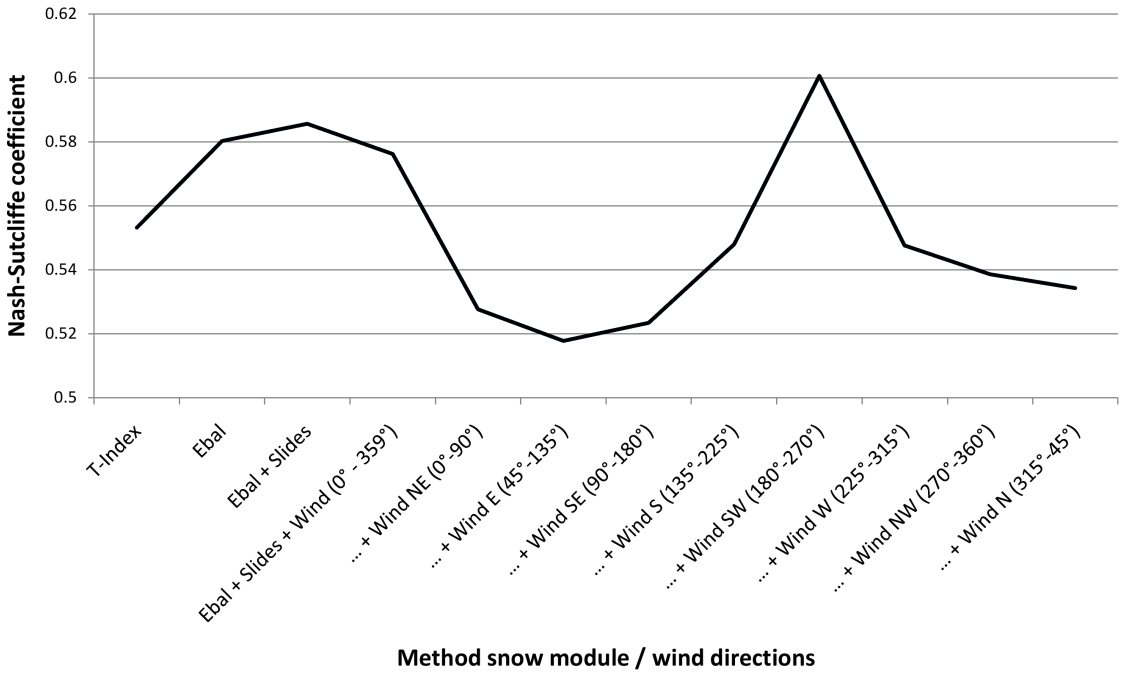

Figure 5.18: Mean Nash-Sutcliffe efficiency for all catchments and different snow model methods as well as changing main wind directions (90 degree sectors rotated in 45 degree steps).

snowmelt totals in March, and April, and increases the rates in May, June, and July (Fig. 5.17). NS performance increases to 0.69 in the melting period 2006 (Fig. 5.14) and to 0.57 in 2007 (Fig. 5.15). Accounting for gravitational snow transport increases runoff model performance regardless of the catchment, and time period (Tab. 5.4).

Wind-driven Snow Redistribution Wind-driven redistribution is estimated roughly by a terrain analysis and implemented by correcting the field of snow precipitation. It is not an event-based method or a detailed description of the wind field and snow transport physics, but an assessment of redistribution patterns on a regional scale. The model combination simulating wind-driven redistribution was run additionally for a shorter testing period (2004 to 2007) using different main wind directions and a general redistribution without a specific direction (Fig. 5.18). The mean NS coefficient for all gauges and different model combinations as well as

different wind directions is presented. The figure shows the importance of determining a realistic main winter wind direction when applying the parameterization of redistribution. Model performance in runoff reproduction decreases when using other main wind direction sectors than the assessed one (south-west, see Sec. 4.3.2).

The effects of simulating gravitational transport on modeled discharge dynamics are amplified by integrating wind-driven snow redistribution. Snow precipitation in winter at steep locations on leeward ridge sides (Fig. 5.7) is highly increased. Consequently, the snow masses are transported laterally down the slopes by the snow slide module. This is a process that can be observed well in reality. The NS coefficient for runoff increases to 0.76 in the melting season 2006 (Fig. 5.14) and to 0.62 in 2007 (Fig. 5.15). Performance does not necessarily increase in every case by introducing wind redistribution. As a consequence of the process described, model performance decreases noticeably when assessing wind redistributions without accounting for gravitational slides (not shown here). In that case, snow masses are transported into steep leeward slopes and not entrained downslope. Therefore, for the simple parameterization of wind-driven snow redistribution used, the simulation of gravitational transport is a prerequisite. This certainly holds for any kind of simulation of lateral wind-driven snow transport in complex, high Alpine terrain. Tab. 5.4 shows that the simulation of wind-driven redistribution increases NS coefficients for the Alpine headwater catchments. Regarding the entire catchment - including downstream subbasins and flat terrain - the increase in model performance is very small (not evident in Tab. 5.4 due to rounding).

6

Climate Change Impact Analysis

To assess potential changes in the regional water balance under changing climate conditions, the established hydrological model system (HM) is forced with climate change scenario data. These data are based on emission scenario driven GCM simulations. To account for the heterogeneity of the complex topography and the according meteorological conditions, the GCM results are downscaled using an RCM. The model chain used in this study is schematically illustrated in Fig. 6.1. Basic information about the models is listed in Tab. 6.1. The resulting RCM model data have shown to be biased (Berg *et al.*, 2013; Wagner *et al.*, 2013), in particular over Alpine terrain, and are consequently corrected using the dense station network in the catchment. The following sections present the datasets and coupling procedures.

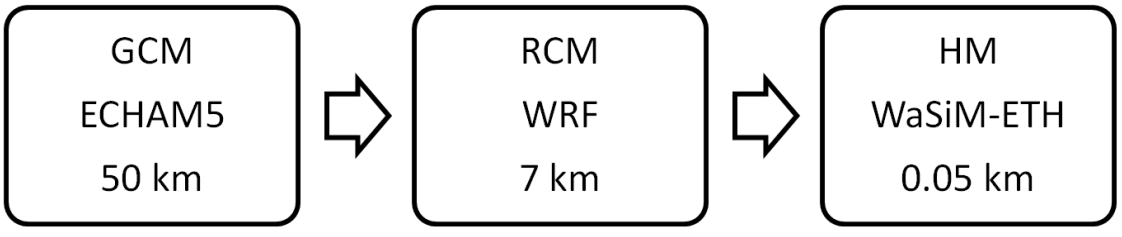

Figure 6.1: Model chain for climate change impact assessment.

6.1 Global and Regional Atmospheric Model Data

GCM Data The basis of the climate projection are global simulations carried out using the ECHAM5/MPIOM model system (Röckner *et al.*, 2003) in the framework of the Fourth Assessment Report AR4 (Pachauri & Reisinger, 2007) of the Intergovernmental Panel on Climate Change (IPCC). This GCM includes physical representations of key atmospheric, cryospheric, ocean, and land surface processes. The GCM was forced by anthropogenic greenhouse gas emissions for the control period 1971-2000 and for the future period 2021-2050 using the IPCC SRES A1B scenario emissions developed in the context of the Special Report on Emission Scenarios SRES (Nakićenović *et al.*, 2000). The model runs were performed in T63 spectral horizontal resolution (approximately 200 km). (Berg *et al.*, 2013; Wagner *et al.*, 2013)

RCM Data The non-hydrostatic RCM WRF (Weather Research and Forecasting Model) version 3.1.1 (Skamarock *et al.*, 2008) was used for dynamically downscaling the GCM data. A double nesting approach with horizontal spatial resolutions of 42 km and 7 km was chosen to account for the large resolution step to the GCM. The coarse nest is centered over Europe, whereas the fine resolution domain comprises Germany and its surroundings including the Alps. The performance of these simulations is discussed in detail in Wagner *et al.* (2013). Results of the two GCM runs described in section 6.1 were downscaled, and the 7 km gridded fields of meteorological parameters necessary for driving the HM are further processed as described in the following section. These parameters are 2 m air temperature, relative humidity, precipitation, wind speed, and global radiation (see details in 3.2). Fig. 6.2 shows the position of the 7 km spaced RCM grid cells above the investigation area.

The HM setup presented in section 3 is based on a grid space size of 50 m. The RCM output data have a horizontal resolution of 7000 m, which means - despite the RCM downscaling - a factor of 140 larger than the HM it should force. These numbers and Fig. 6.2, which shows the model grid locations of the RCM WRF above the catchment, illustrate that there is still a large gap between the resolutions of these two coupled models. Therefore, the RCM data is further downscaled by spatially

Table 6.1: Model specifications for the members of the coupled system.

Model	Model type	Scale	Spatial res.
ECHAM5-MPI/OM	atmospheric	global	T63 / appr. 200 km
WRF	atmospheric	regional	42 km, 7 km
WaSiM-ETH	hydrological	regional	50 m

interpolating the data to the finer grid of the HM using the high-resolution DEM of the catchment and the respective RCM grid elevations. This is done according to the method described in section 3.2.

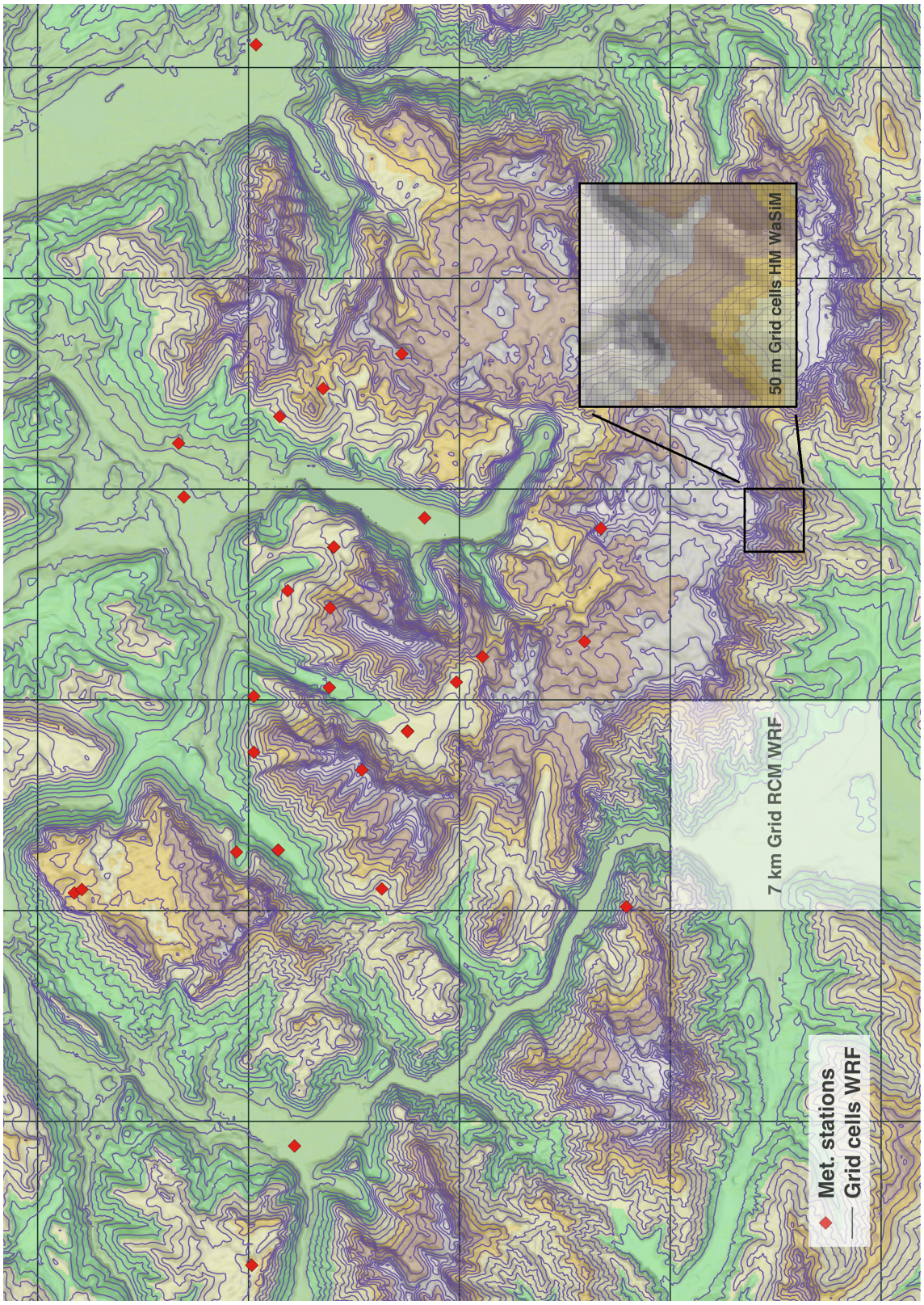

Figure 6.2: Locations of the meteorological stations (red) and the RCM grid cells (WRF, 7 km Grid) in the model domain. The enlarged close-up view of the 50 m HM (WaSiM-ETH) grid spacing illustrates the differences in the spatial resolution between the RCM and the HM.

6.2 Bias Correction of RCM Data

The climate simulations used in this study have shown to overestimate precipitation amounts in the Alpine region (Berg *et al.*, 2013; Wagner *et al.*, 2013). The spatial distribution of mean annual precipitation in the control period 1971-2000 is shown in Fig. 6.6 (left). The RCM output is interpolated to the model grid as described in the previous section. Compared to Fig. 3.4, the values reveal a large positive bias in the resulting precipitation amounts. These two fields are not quantitatively comparable, as the data in Fig. 3.4 is based on the modeling period 2001 to 2010. However, the mean annual values should be in the same range. Tab. 6.2 shows mean daily precipitation values for the observation stations and the RCM model grid cells that are in close vicinity. The consistent and significant overestimation of precipitation in the RCM simulations is apparent in this comparison. The finding of a wet bias, meaning the overestimation of precipitation amounts confirms the results of Berg *et al.* (2013). This wet bias is corrected using a standard quantile mapping (QM) approach, which is described in the following section.

6.2.1 Quantile Mapping

The QM method maps the distribution of a variable onto that of the respective observed data using cumulative distribution functions (CDFs). To correct model values for a future period, the corresponding percentile values for the future projection points in the CDF of the model for the training period and then the observed values for the same CDF values of the observations are located (Li *et al.*, 2010).

For model X and observation Y, the distribution functions are modeled using theoretical parametric distributions $F_X(x)$ and $F_Y(y)$. For a specific model time step x, the probability $P(X \leq x) = F_X(x)$ is determined. This probability is compared to the probability distribution $F_Y(y)$ of the observations at the point where $F_Y(y) = F_X(x)$ and the data value at the respective point in the distribution is picked (6.3). For a specific time step t of a modeled time series $mod(t_1), ..., mod(t_n)$

Station	$\overline{obs}$	$\overline{mod}$	$q = \overline{obs}/\overline{mod}$
Schönau	4.00	5.22	0.76
Höllgraben	2.90	5.00	0.57
Kühroint	4.48	7.20	0.62
Hinterseeau	4.04	7.35	0.55
Königsberg (Pegel)	4.65	6.94	0.66
Schapbach	3.35	7.20	0.46
Kühroint	4.63	7.20	0.64
Lahneralm	4.41	7.20	0.61
St.Bartholomä	3.74	7.20	0.51
Wimbachschloss	4.27	7.20	0.59
Brunftbergtiefe	4.94	7.35	0.67
Bindalm	4.93	6.86	0.72
Lahnwaldfütterung	4.57	7.35	0.62
Halsalm	5.33	5.78	0.92
Brunftbergtiefe	5.13	7.35	0.70
Auf dem Gries	4.29	8.71	0.49
Eckau	3.94	7.20	0.55
Mittereis	4.74	7.35	0.64

Table 6.2: Mean daily precipitation values for the observation stations and the respective RCM model grid cells in the period 1989-2000 and ratio between observed and modeled means.

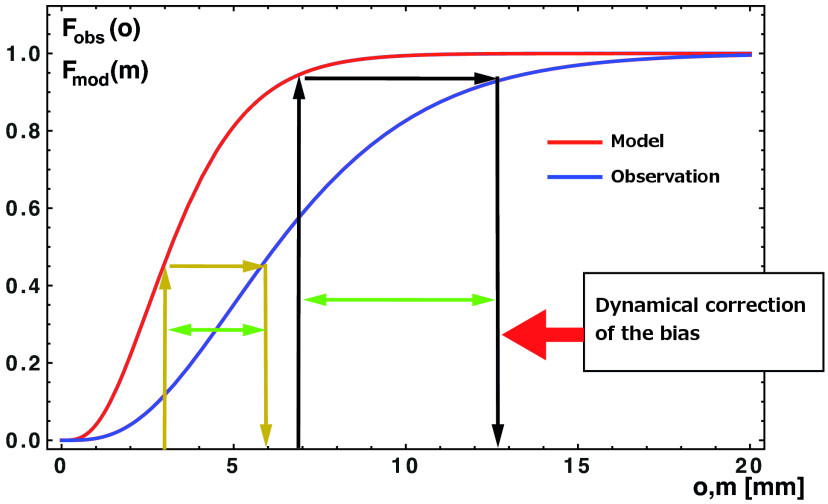

Figure 6.3: Schematic representation of the Quantile Mapping approach to correct the RCM model bias (Vogl & Kunstmann (2013), modified).

and observations $obs(t_1), ..., obs(t_n)$, the corrected model value is

$$mod_{cor}(t) = F_{obs}^{-1}(F_{mod}(mod(t))). \tag{6.1}$$

In this study, only precipitation is bias corrected, as this parameter is the most significantly biased one, and is - at the same time - the most important forcing variable for the HM. The HM is highly sensitive to amount and timing of precipitation input. Temperature, relative humidity, wind speed, and global radiation are used as calculated by the RCM.

Appropriate pairs of modeled and observed time series have to be determined. For a given meteorological station, the RCM model cell is identified that is positioned next to the station. The position of the observing stations and the surrounding RCM grid cells in the investigated area are shown in Fig. 6.2. As multiple stations are situated within a RCM model cell, there are multiple relevant observation time series $obs_1(t), ..., obs_k(t)$ that may be used to correct a modeled series $mod(t)$. Therefore, k bivariate time series $(mod(t), obs_k(t))$ can be analyzed to determine possible correction functions between modeled and observed time series. For the QM approach, the stations were chosen that show the closest agreement with the respective RCM model cell regarding precipitation data. Observed time series $obs_k(t)$ were compared to reanalysis forced RCM output $mod(t)$. Model values smaller than 0.1 mm daily precipitation have to be regarded as numerical artifacts and lie within the measurement uncertainty of the precipitation gauges. They were therefore set to zero. (Vogl & Kunstmann, 2013)

As most of the observing stations that were already measuring during the RCM control and reanalysis run period (1971-2000) record daily precipitation totals (Tab. 3.1), the bias correction and location refinement is done using daily accumulated values. The corrected daily values are consequently disaggregated to hourly values before forcing the HM as described in the following section.

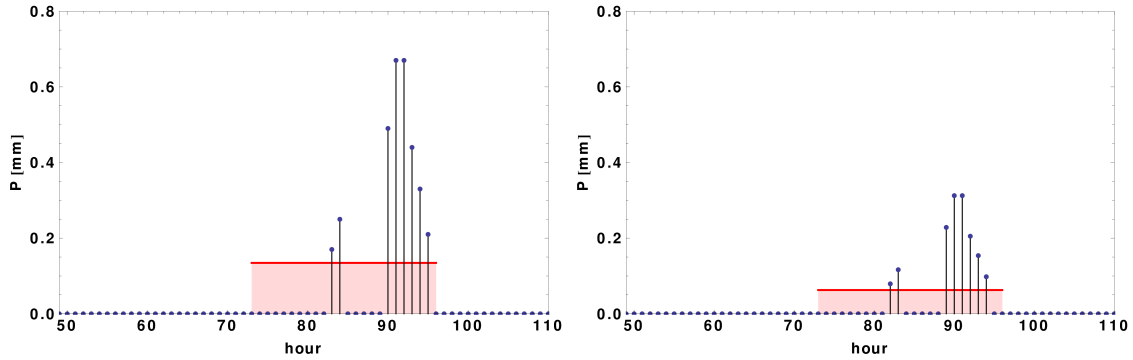

Figure 6.4: Precipitation event illustrating the procedure for the disaggregation of daily RCM data to hourly values using hourly recorded station data. The observed hourly values are shown on the left with the daily mean indicated in red. The disaggregated daily RCM data are shown on the right with the original daily value indicated in red (Vogl & Kunstmann (2013), modified).

6.2.2 Disaggregation of Daily RCM Precipitation

The corrected daily RCM fields are disaggregated to hourly fields to keep a consistent time resolution in forcing and running the model. The method used here is similar to the disaggregation method applied in Sec. 3.2, when the daily measurements of the manually operated stations were disaggregated to hourly values using the high-resolution measurements of the automatic stations.

The portions of the single hours on the daily totals of the original data is used to disaggregate the respective corrected daily totals. For a day d of the uncorrected RCM precipitation data with hourly values P_{hi} for hours $i = 1, ..., 24$, the daily precipitation P_d is

$$P_d = \sum_{i=1}^{24} P_{hi}. \tag{6.2}$$

$P_{hi}/P_d \cdot 100\%$ of the daily precipitation occurs during the hour i of the day. Accordingly, for the corresponding bias corrected time series, which exists on a daily basis with the daily precipitation total $P_{d_{corr}}$, the hourly time series is calculated as

$$P_{hi_{corr}} = \frac{P_{hi}}{P_d} \cdot P_{d_{corr}}. \tag{6.3}$$

Fig. 6.4 illustrates the approach using an exemplary precipitation event. Hourly

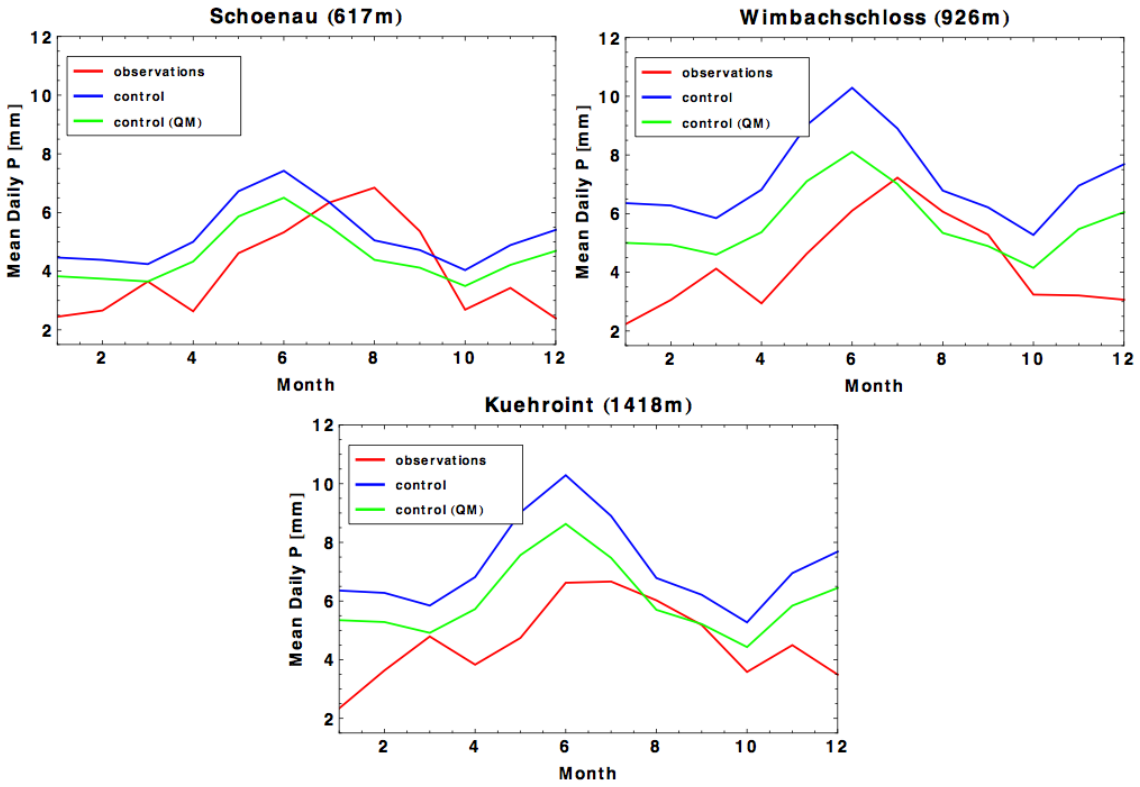

Figure 6.5: Mean monthly precipitation (daily totals) in the period 1989-2000 for the stations *Schönau* (617 m MSL), *Wimbachschloss* (926 m MSL), *Kühroint* (1418 m MSL), and the matching RCM grid points. Shown are values for uncorrected reanalysis forced RCM output, observed values, and corrected precipitation amounts (Vogl & Kunstmann, 2013).

precipitation values of the WRF model run for three days are presented (Fig. 6.4, left). The first day is dry, hourly and daily totals are zero. The second day, precipitation occurs during 7 hours which amounts up to 3.32 mm in total. For each hour with precipitation, a certain portion on the daily total precipitation is calculated. The bias corrected daily sum is disaggregated in the following using these portions of the uncorrected RCM data. Fig. 6.4 (right) shows the corrected time series after applying the disaggregation procedure. The daily variations of the uncorrected, original data are reproduced. These corrected, hourly time series are used to force the HM as presented in the following.

6.2.3 Corrected Forcing Data

Fig. 6.5 presents the results of of the QM approach for three stations in the catchment. Shown are mean monthly precipitation amounts in mm. Generally, the annual cycle in precipitation is apparent in RCM simulations and observations with a maximum during summer months, and a minimum in winter. RCM results show a slight shift of maximum precipitation to earlier months, the absolute maximum value consistently occurring in June, whereas the maximum observed values appeared in July and August. The QM approach is not able to correct this time shift. Comparing absolute values of uncorrected RCM grids and observations, a consistent large overestimation is obvious. This behavior can be explained partly by the described wet bias of the RCM simulations, but is also caused by the different area the grid cell is representing. In the complex terrain of the catchment, a 7 km grid cell of the RCM spans large terrain variations, and includes valley as well as peak regions (Fig. 6.2). This results in a mean elevation of the cell that is generally larger than the elevation of the point where the respective meteorological stations are located (Fig. 6.5). The stations that capture precipitation are predominantly situated in lower elevations (Fig. 3.1 and Tab. 3.1). The QM approach therefore corrects not only for a bias, but at the same time, the RCM grid values are downscaled to the elevation of the respective station (Fig. 6.5).

Uncorrected and corrected annual precipitation amounts in the control period are shown in Fig. 6.6. Spatial minimum, maximum, and mean value of annual precipitation are reduced according to the correction of the wet bias. The corrected values range from 1290 mm to 2836 mm with a spatial mean of 1969 mm precipitation per year (1971-2000). These values are slightly higher than during the observational period 2001-2010. These differences can originate either from the different climatological period or represent a remaining bias in the data.

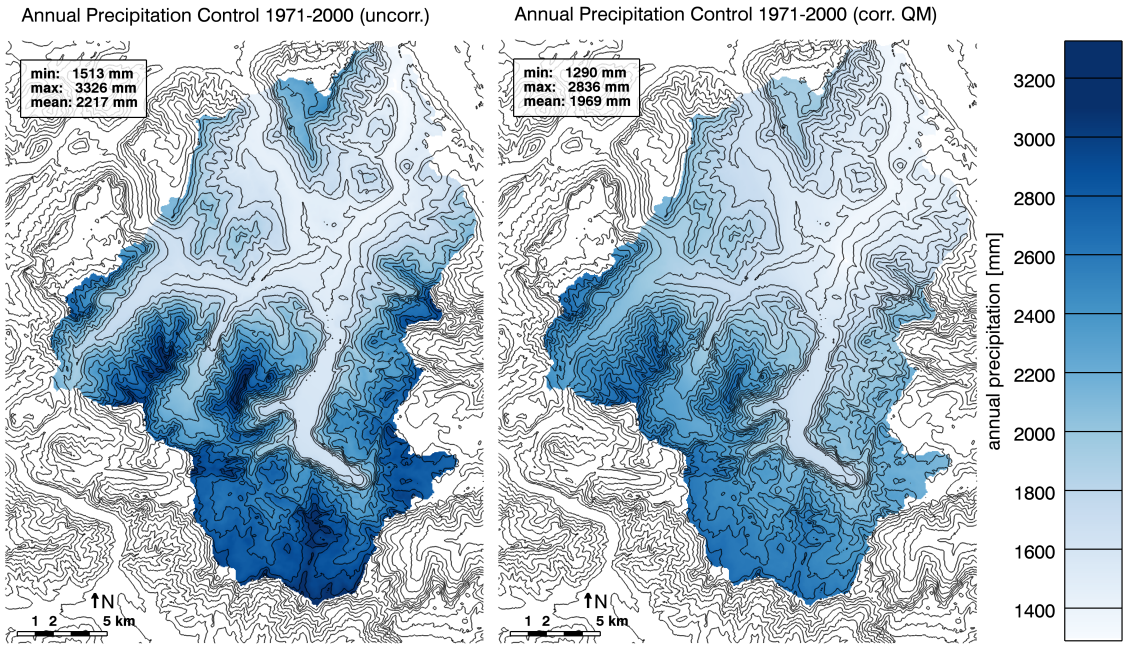

Figure 6.6: Annual precipitation 1971-2000. RCM field interpolated to the 50 m HM model grid, uncorrected (left) and bias corrected using a QM approach (right).

6.3 Benefits of the Model Extensions in Climate Runs

To illustrate the necessity for the developed snow model approaches in long-term climate change impact model runs, an exemplary comparison for a 30 year climate control run (1971-2000) is presented in the following. Fig. 6.7 shows mean snow cover period in 1971-2000 modeled using the temperature index approach and for comparison by the energy balance calculation including lateral redistribution processes. In summary, the effects that are introduced by the new snow model approaches explained in detail in Sect. 5.2 are even more pronounced when performing long-term model runs. There is a particular problem when using the temperature index approach without lateral redistributions that becomes very distinct in the 30 year simulation. Large amounts of snow build up in high elevations that are not melting because of the low air temperatures (Fig. 6.7, left). Over 30 years, large areas develop with perennial snow coverage. In reality, the influence of radiation in the exposed peak regions and - even more important - the impact of wind- and gravitational redistribution reduce the snow amounts (compare Sect. 5.2). When

simulating these processes using the developed approaches (Fig. 6.7, right), the large areas with unrealistically long snow cover durations disappear. The lateral processes move the locations of highest snow cover durations from the exposed peak regions to the foot of shaded, northern oriented, steep faces as explained in Sect. 5.2.

This result can also be observed when inspecting the according frequency histograms of mean annual snow coverage as shown in Fig. 6.8. There is a large decrease in frequencies with annual snow coverage higher than 250 days when using the energy balance approach and simulating lateral snow processes. Especially regions with 365 days of snow coverage and unrealistically large amounts of snow vanish.

Additionally, as the energy balance approach does not need any parameters to be calibrated, it is an approach that is ideally suited to be used in climate change impact assessment studies. In contrast, temperature index methods are not able to adapt to changing systems because of their need for calibration and are highly sensitive to temperature change. Therefore, the detailed climate change impact analysis in the following sections is solely based on model runs using the newly developed and implemented snow model approaches (energy balance calculation including lateral snow processes).

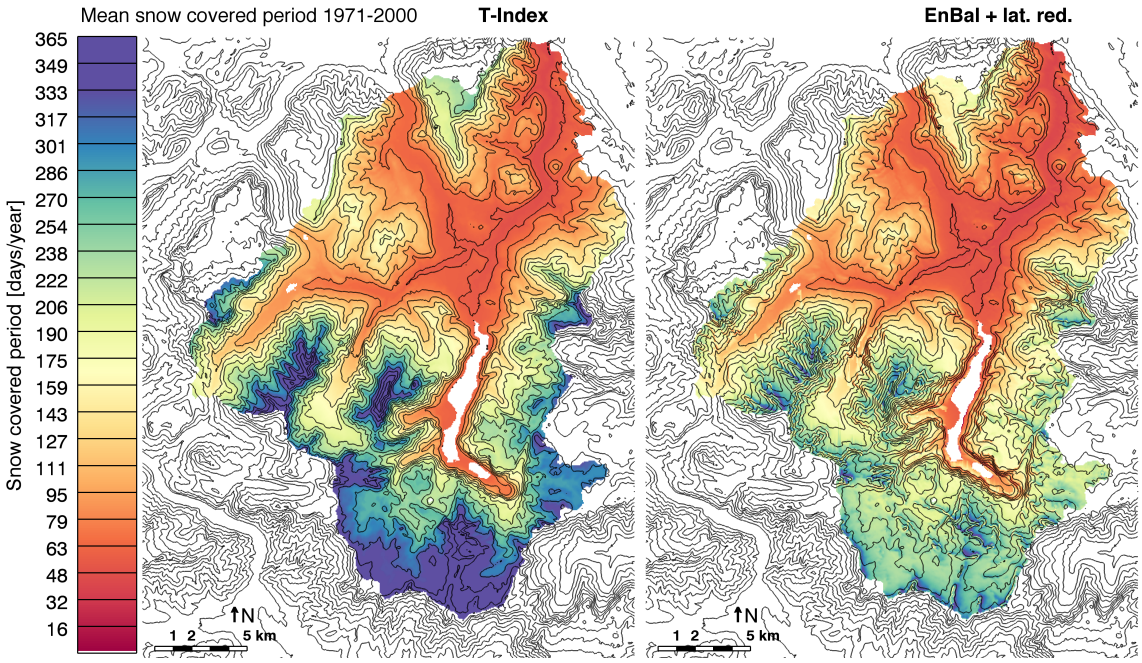

Figure 6.7: Spatial distribution of mean annual snow covered period 1971-2000 modeled by the HM WaSiM-ETH forced by the RCM WRF (control run). Snow cover was modeled using the T-Index approach (left) and the energy balance method including lateral redistribution processes (right).

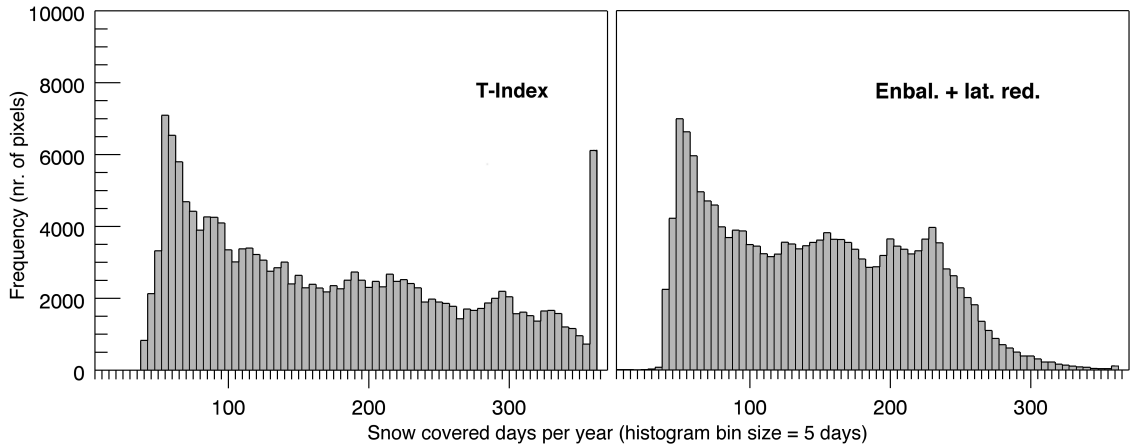

Figure 6.8: Frequency histogram of mean annual snow cover period 1971-2000 modeled by the HM WaSiM-ETH forced by the RCM WRF (control run). Snow cover was modeled using the T-Index approach (left) and the energy balance method including lateral redistribution processes (right).

6.4 Climate Change Signal

The climate change signal that is propagated to finally force the HM after the applied coupling and correction procedures is presented in the following. Fig. 6.9 (left) shows projected changes in the spatial distribution of mean 2 m air temperature. Projected temperature changes range from 0.81 $°C$ in the lower elevations to 1.02 $°C$ in the high elevated regions and are projected to increase by 0.94 $°C$ to 5.68 $°C$ on average (Tab. 6.3). The spatial distribution of annual precipitation is presented in Fig. 6.9 (right). Precipitation is projected to slightly increase by 25 mm (1.3 %) to 2032 mm on average. Similar to temperature changes, the largest precipitation increases (max. 34 mm) are located at higher elevations, whereas increases at lower regions are expected to be smaller in absolute values (min. 15 mm). Regarding the modeled partitioning of precipitation into liquid and solid precipitation, a very significant effect is revealed (Fig. 6.10). Rainfall is increasing for the whole catchment, with a maximum increase in the highest peak regions. The smallest increases are projected to occur in medium range elevations (800 to 1300 m). In contrast, snow precipitation decreases for the whole catchment with a maximum of absolute decrease in the medium range elevations, and a minimal decrease in the peak regions (Fig. 6.10, right). Relative changes in annual snowfall (not presented here) range from -2.4 % in the peak regions to -25.7 % in the valleys. Summarizing, the decrease in snowfall of -25.7 % in the valley regions is large, whereas snowfall remains nearly unchanged in the high elevations. The overall increase in annual precipitation (+25mm / +1.3%, Tab. 6.3) and particularly in rainfall (+75mm / +6.1%, Tab. 6.3) is relatively small.

6.5 Hydrological Impact

To assess potential impacts of a changing future climate on the regional hydrology, HM runs were performed and analyzed for the control period 1971-2000 and the scenario period 2021-2050 using the data preprocessing and coupling strategy described in the previous sections. For each model run, one year initialization runs were performed to simulate proper starting state variables and remove effects of model spin-up in the impact analysis. Results of this comparison focusing on snow related processes are presented in the following section.

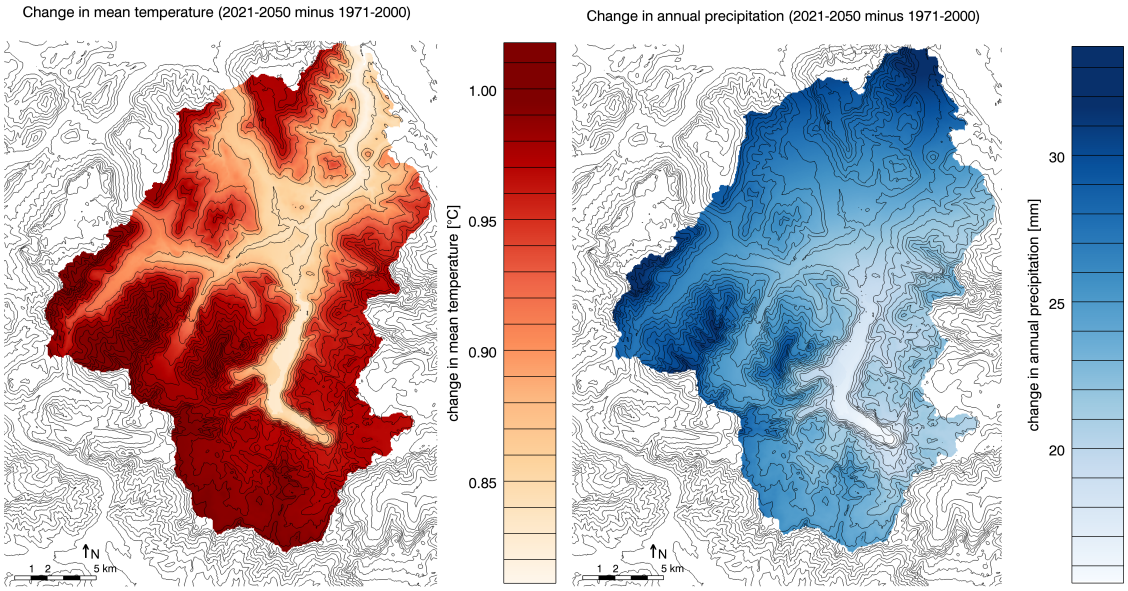

Figure 6.9: Climate change signal propagated to the hydrological model (HM). Spatial distribution of projected changes in mean temperature (left) and mean annual precipitation (right) between 1971-2000 and 2021-2050 based on the SRES scenario A1B driven GCM ECHAM5, downscaled to a spatial resolution of 7 km using the RCM WRF, and interpolated to the HM grid (50 m).

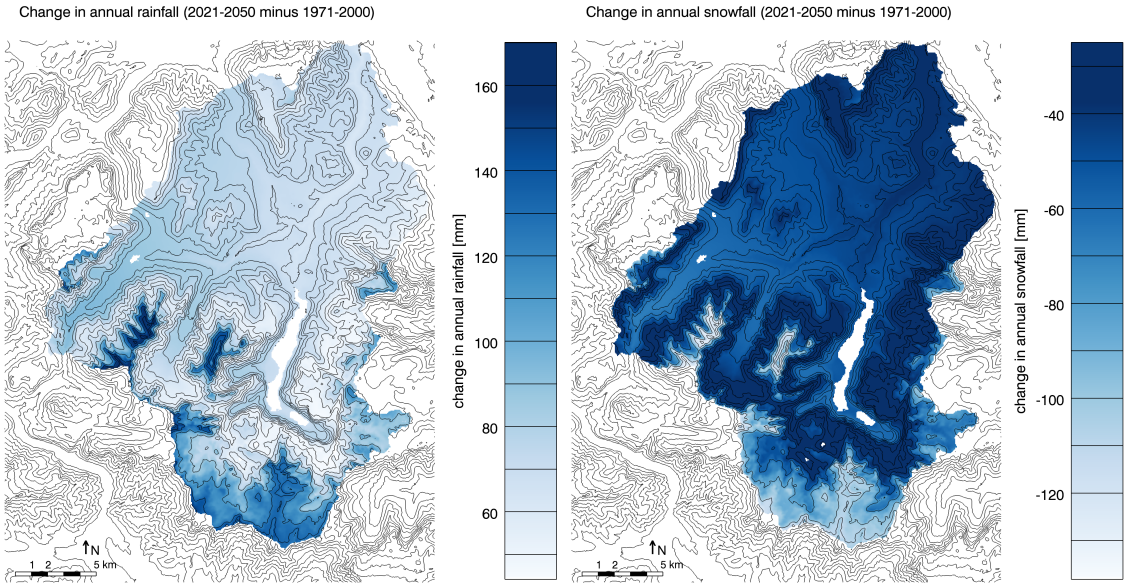

Figure 6.10: Spatial distribution of projected changes in annual rainfall (left) and annual snowfall (right) between the control (1971-2000) and the scenario period (2021-2050) based on the SRES scenario A1B driven GCM ECHAM5, downscaled to a spatial resolution of 7 km using the RCM WRF.

6.5.1 Snow Cover Duration

This section presents climate change impact analysis results regarding snow coverage and melt timing in the catchment. Fig. 6.11 (left) shows projected absolute changes in mean annual snow covered period in days per season between the control period 1971-2000 and the scenario period 2021-2050. The results show a significant, elevation-dependent decreasing trend in snow cover duration. Values range from -6 to -30 days decrease in snow cover duration per year. Maximum decrease is located in mid-elevation ranges and in zones where snow cover duration is high due to large accumulation rates by lateral processes, and that are at the same time low-elevated. These are the zones that are referred to in section 5.2. This fact underlines the necessity to account for processes of lateral snow redistribution and radiation impacts on ablation in high resolution impact studies. The minimum absolute decreases are on the one hand located at high-elevated regions, where snowfall is not expected to change significantly (section 6.4) and future ablation conditions despite the changes being high, e.g. a large temperature increase (Fig. 6.9), are still cold enough for long snow cover durations. On the other hand, absolute changes are small on southern aspected, wind-exposed, or very steep slopes, where the duration has already been short. The spatial distribution of relative changes in annual snow cover duration is shown in Fig. 6.11 (left). The field shows a clear terrain-following pattern with larges decreases of (-33 %) in the valleys and a decrease in relative decline with increasing elevation down to -2 %. Fig. 6.12 visualizes this dependency by showing absolute (top) and relative (bottom) snow cover duration and respective elevation for all pixels in the HM simulation domain. The band of maximum decreases in the elevation ranges of 800 m to 1300 m is clearly visible. The smaller decreases in the lower elevations can be explained by less possible occurring snow covered days that could be shortened. This finding is underlined by the relative changes (Fig. 6.12, bottom) having their maxima in the lowest elevations. The relative changes show an impressively sharp relative minimum at -6 to -7 % above elevations of 1500 m.

6.5.2 Changes in Snowmelt and Discharge

The projected changes in mean monthly snowmelt totals between the control period 1971-2000 and 2021-2050 are presented in Fig. 6.13. Snowmelt is projected to

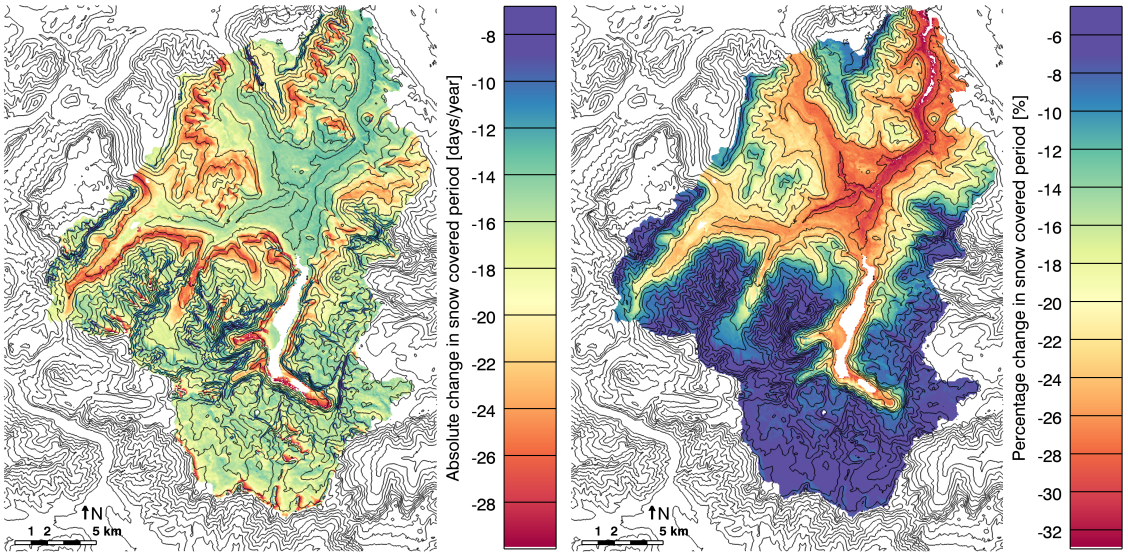

Figure 6.11: Projected changes in mean annual snow covered period between the control (1971-2000) and the scenario period (2021-2050). Absolute (left) and relative changes (right) based on the SRES scenario A1B driven GCM ECHAM5, downscaled to a spatial resolution of 7 km using the RCM WRF, and interpolated to the model grid (50 m).

increase noticeably in late autumn (November), during the mid-winter months January and February, as well as in May, when generally the largest snowmelt amounts occur. From June to October, snowmelt amounts decrease consistently because of the projected reduced snow cover duration (see Sec. 6.5.1). Whereas relative values show large decreases in snowmelt amounts of up to -40 % in August, the absolute changes are projected to be small. Fig. 6.14 shows the respective projected absolute and relative changes in mean monthly runoff values. The maximum value of MQ in June is significantly reduced in the scenario period due to the decreases in snowmelt. The maximum is shifted to May according to the respective changes in snowmelt amounts. Runoff values are projected to increase in May due to the shift in the snowmelt regime. The decrease of runoff values in July can be explained by the reduced projected snow cover duration and therefore less remaining snow to provide melt water in summer time. From August to April, the expected increases in rainfall amounts (see Sec. 6.4) cause small increases in mean monthly runoff. Besides the clear reduction of runoff amounts in June, absolute changes in seasonal snowmelt and runoff amounts are projected to remain relatively small.

Fig. 6.15 shows the frequency histogram of hourly discharge values for the control

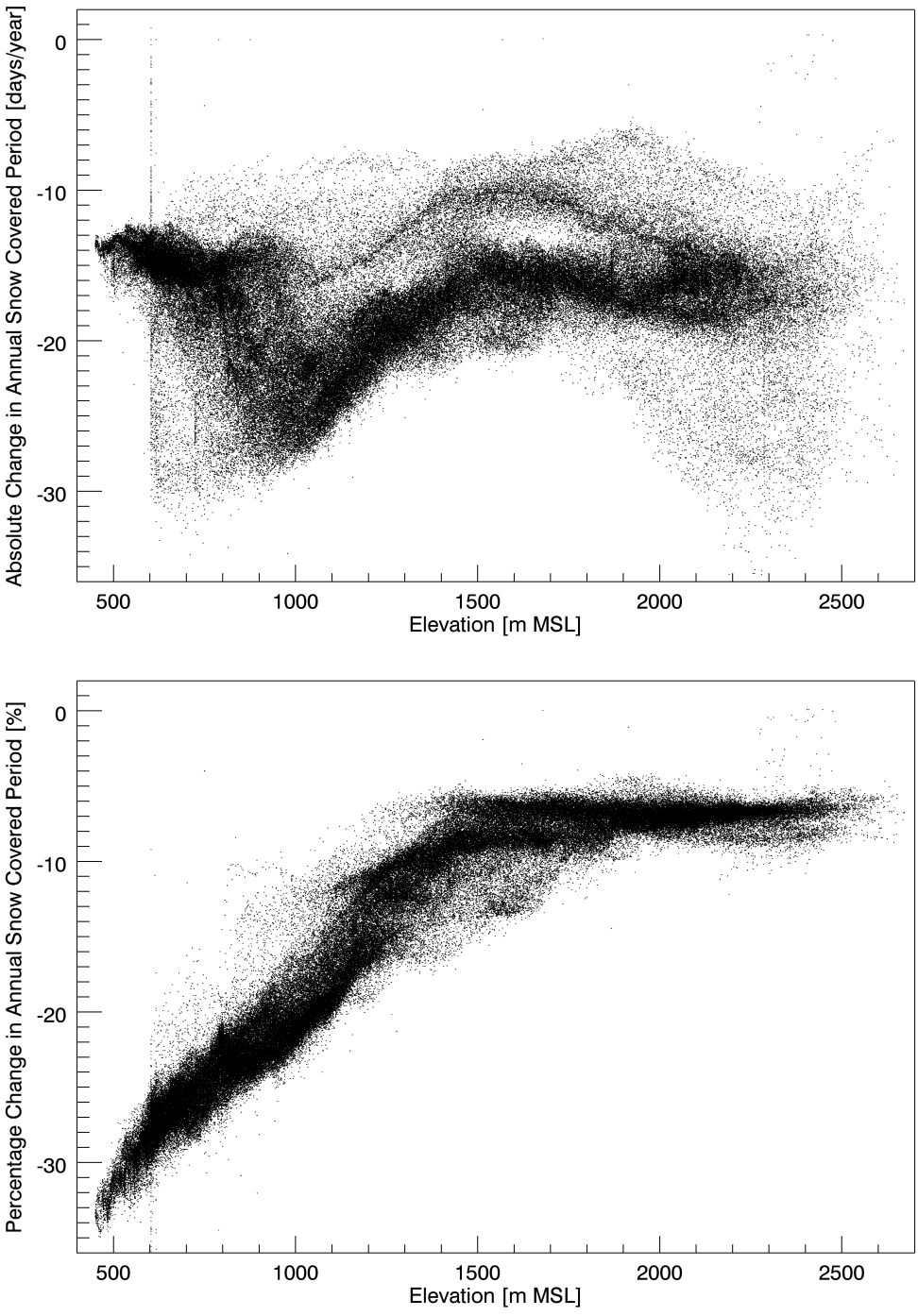

Figure 6.12: Dependence of absolute (top) and relative (bottom) changes in annual snow cover duration on terrain elevation. Shown are projected changes between the control (1971-2000) and the scenario period (2021-2050) based on the SRES scenario A1B driven GCM ECHAM5, downscaled to a spatial resolution of 7 km using the RCM WRF, and interpolated to the model grid (50 m). Plotted are the 172959 model grid cells of the HM.

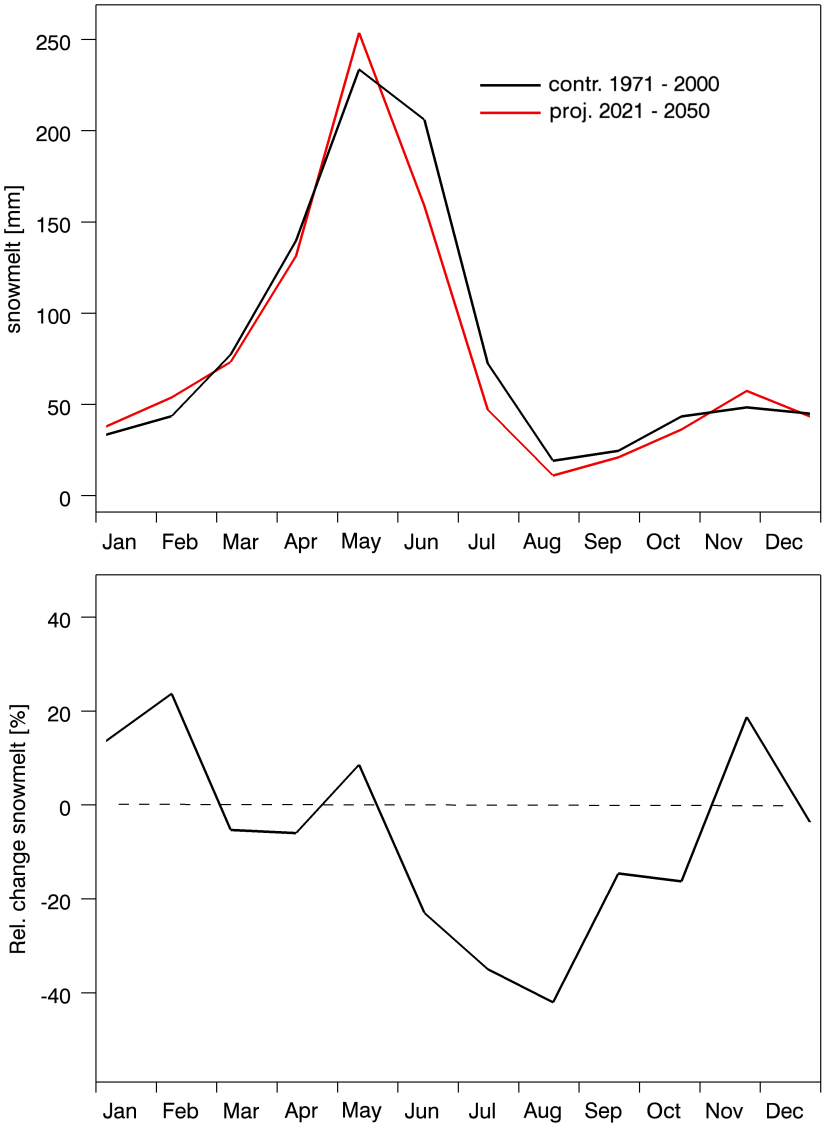

Figure 6.13: Projected changes in snowmelt regime between the control (1971-2000) and the scenario period (2021-2050). Absolute (top) and relative changes (bottom) based on the SRES scenario A1B driven GCM ECHAM5, downscaled to a spatial resolution of 7 km using the RCM WRF.

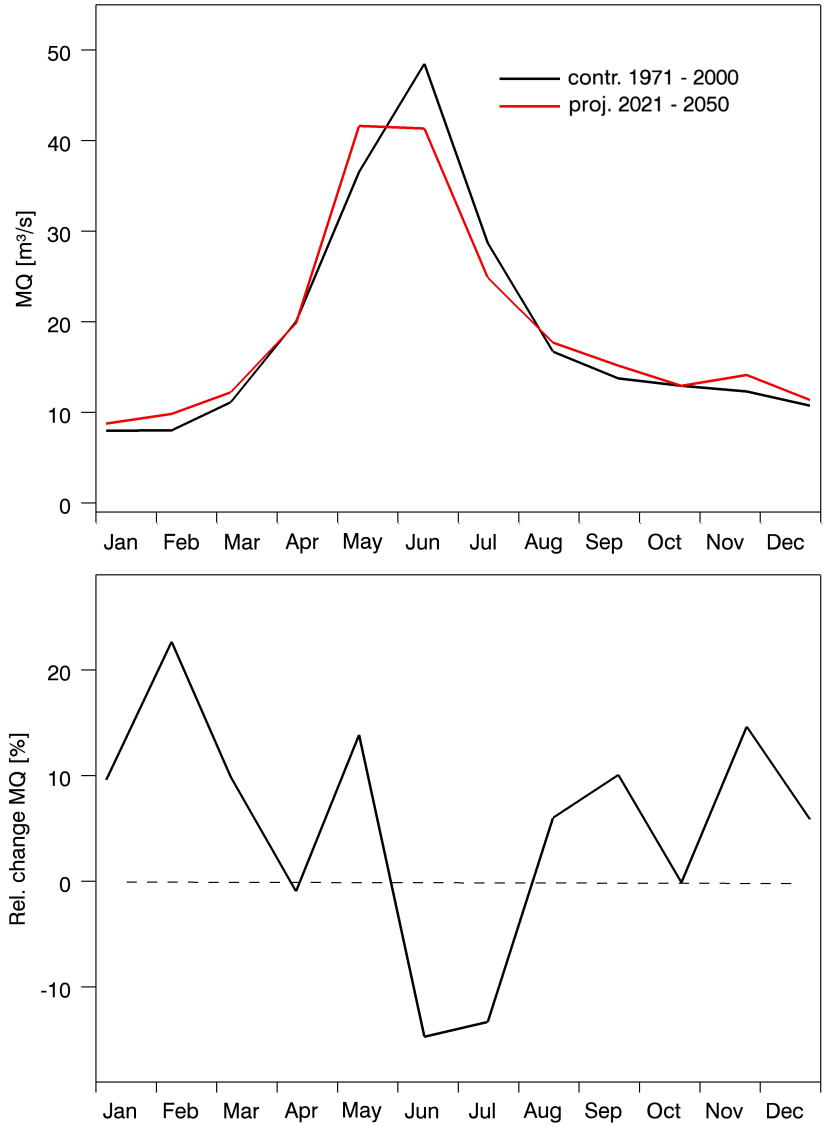

Figure 6.14: Projected changes in mean monthly discharge between the control (1971-2000) and the scenario period (2021-2050). Absolute (top) and relative changes (bottom) based on the SRES scenario A1B driven GCM ECHAM5, downscaled to a spatial resolution of 7 km using the RCM WRF.

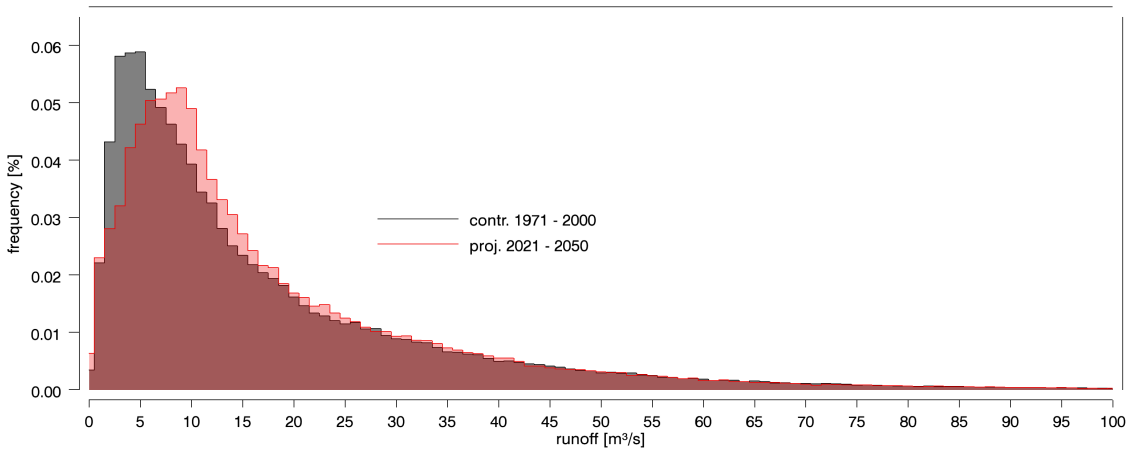

Figure 6.15: Frequency histogram of hourly discharge at the gauge *St. Leonhard* for the control (1971-2000) and the scenario period (2021-2050). The relative frequencies are plotted for increasing value classes with an increment of 1 $m^3 \cdot s^{-1}$.

and the scenario period at the outlet gauge *St. Leonhard*. Plotted are the relative frequencies for mean values of hourly discharge with an increment of 1 $m^3 \cdot s^{-1}$. The comparison of the histogram for the control period 1971-2000 and the future scenario 2021-2050 reveals an increase of events with very small runoff amounts (1 to 2 $m^3 \cdot s^{-1}$). The mid-range hourly runoff rates of 3 to 7 $m^3 \cdot s^{-1}$, representing the most frequent range in the control period, show a large decrease in their projected frequency. Values larger than 8 $m^3 \cdot s^{-1}$ generally show a slight increase in their occurrence with significant higher frequencies at values from 8 to 18 $m^3 \cdot s^{-1}$. This shows a significant, however not dramatic regional trend to an intensification and accumulation of extreme runoff rates at the expense of mid-range river discharge rates.

6.5.3 Changes in the Water Balance Budgets

Tab. 6.3 presents the main compartments of the regional water balance, their quantities during the control and the scenario period, as well as projected absolute and relative changes. The values for temperature, precipitation, rainfall, and snowfall reflect the meteorological changes discussed in Sect. 6.4. The projected rise in mean temperature of 0.94 $°C$, is accompanied by an increase in precipitation of 25 mm (+1.3 %). This increase in precipitation is valid only for rainfall (+75 mm / +6.1

Table 6.3: Differences in the spatial distributions of meteorological variables and water cycle compartments between the control period 1971-2000 and the scenario period 2021-2050. Minima, maxima, and means for the spatial distribution in the model domain.

	Contr. period 1971-2000			Scen. period 2021-2050			Scen. - Contr.	Scen. - Contr.
Mean annual	min	max	mean	min	max	mean	mean diff.	diff. %
Air temperature [$°C$]	-4.57	10.26	4.74	-3.56	11.07	5.68	+0.94 $°C$	-
Precipitation [mm]	1281	3059	2007	1307	3086	2032	+25 mm	+1.3 %
Rainfall [mm]	492	1772	1229	608	1867	1304	+75 mm	+6.1 %
Snowfall [mm]	125	2530	778	94	2441	727	-51 mm	-6.6 %
Snowf./prec. ·100 [%]	9	83	35	7	79	32	-3 %	-8.6 %
Snowmelt [mm]	126	8698	1000	107	8805	938	-62 mm	-8.2 %
Snow cover dur. [d]	36	365	148	23	365	129	-19 d	-12.8 %
Evapotransp. [mm]	51	2022	617	67	1915	625	+7.9 mm	+2.4 %
Runoff [mm]	75	8629	1415	55	8740	1433	+17.5 mm	+2.8 %

%), whereas snowfall is projected to decrease (-51 mm / -6.6 %). This change in precipitation characteristics is the main driver for the consequent changes in the regional hydrology. Snow cover duration decreases significantly (-19 d / -12.8 %, see also Sec. 6.5.1). Consequently, snowmelt amounts are projected to decrease by 62 mm (-8.2 %). The high maximum snowmelt values in the spatial distribution (8698 mm in the control / 8805 mm in the scenario period) characterize the implementation of the new lateral snow redistribution processes. These large snowmelt values occur at spatially very limited zones of high snow accumulation, and are distinctive for the steep terrain of the catchment. The processes are described in detail in Sect. 5.2. Mean annual evapotranspiration is projected to slightly increase (+7.9 mm / +2.4 %). However, one has to consider that in this application, vegetation characteristics are implemented with intraannual dynamics that represent a seasonal cycle, but are interannually stationary. Possible future changes in vegetation and general land use are not considered here. Despite the compensating increase in evapotranspiration, mean annual runoff is projected to increase by 17.5 mm (+2.8 %) due to the increases in rainfall amounts.

7

Conclusion and Outlook

This study was aimed at investigating effects of complex snow process descriptions on the performance of a hydrological model system in high Alpine terrain. Several high Alpine-specific snow modeling methods were implemented in a distributed hydrological model. The resulting changes in modeled spatial snow cover and runoff dynamics were discussed. The enhanced hydrological model system was consequently forced with atmospheric scenario data to assess possible climate change impacts on the regional hydrology of the investigated catchment.

7.1 Snow Cover and Runoff Dynamics

The implemented approach for calculating the energy balance of the snow cover was validated using point measurements of SWE and snow depths. The model has proven to work stable in reproducing seasonal snow cover development over a wide range of elevations. This was holding true despite there were several sources of uncertainty included, in particular the measurement and interpolation of the meteorological forcing. The analysis of the contributing energy fluxes to the ablation of

the snow cover revealed a realistic simulation of the single terms.

Regarding the spatial snow distribution on the catchment scale, the energy balance calculation scheme produces topography-dependent snow dynamics. The considering of short- and longwave radiation, turbulent energy fluxes, advective energy by precipitation, and soil heat flux in the simulation of the snow cover evolution leads to a distribution that depends on exposure, slope and shading effects. The simulation of lateral snow transport consists of two processes: the snow sliding down steep slopes driven by gravitation and the redistribution of snow caused by wind. The gravitational snow transport module generally removes snow from very steep faces and leads to large snow accumulations at the base of these slopes. This process and the following snow distribution can well be observed in the remote sensing datasets. This redistribution of snow within the single subcatchments is mandatory to simulate a realistic pattern of snow accumulation and in the following a correct timing of snow ablation and consequently runoff. However, a full quantitative validation should be subject of future research. The parameterization of wind-driven snow redistribution based on a terrain analysis redistributes snow from exposed to sheltered areas. The process interacts with the gravitational transport scheme, as snow is redistributed to leeward slopes and consequently transported downslope by gravitation. The losses in modeled snow cover duration by the introduction of lateral processes can be found at high elevated, exposed, steep ridge sites that are oriented to the main wind direction. These areas are blown free of snow by wind and lose snow masses by gravitational slides. The maximal gains in snow-covered days are located at leeward ridge sites and at the foot of steep faces, where snow is transported to by the implemented snow slide algorithm.

The model's performance on the catchment scale was evaluated using satellite-based remote sensing data. A classification of snow coverage at the end of three different winter seasons was done by analyzing Landsat-ETM+ scenes. The model was able to reproduce the general pattern and most of the fine details of snow coverage. Spatial numerical performance indices showed a satisfying result.

In the complex terrain of the catchment, the integration of the energy balance-based

approach to determine snowmelt combined with the simulation of lateral snow transport results in large changes in the simulated spatial distribution of snow cover duration compared to a temperature index based simulation. These large differences lead to relatively small, but still significant changes in the simulated dynamics of runoff. The diurnal variations in discharge due to snowmelt peaks at daytime are simulated more realistically by introducing the energy balance approach. Furthermore, the seasonal distribution of snowmelt rates and subsequent runoff generation are modeled more accurately. Accounting for gravitational snow transport increases runoff model performance regardless of the catchment, time period, and melt module. When assessing wind-driven redistribution of snow, model performance for runoff decreases noticeably when gravitational slides are neglected. As a consequence, accounting for gravitational snow transport is a prerequisite for the simulation of wind-driven snow redistribution in this catchment. This might hold for any kind of simulation of lateral wind-driven snow transport in complex, high Alpine terrain. The simulation of wind-driven redistribution increases Nash-Sutcliffe coefficients for discharge in the Alpine headwater catchments, whereas regarding the entire catchment, changes are small.

7.2 Climate Change Impact

To assess possible impacts of a changing climate on the hydrology and water balance of the region, dynamically downscaled climate simulations were used. The RCM data have shown to be wet-biased specifically in the region of interest. They were consequently bias-corrected using a standard Quantile-Mapping approach. The data was further downscaled by interpolation to the 50 m HM model grid using the methods employed in the previous model setup development. The enhanced HM was run for a control period (1971-2000) and for a near future scenario period (2021-2050). The model application reveals a significant, elevation-dependent decreasing trend in snow cover duration. The absolute largest decrease of about 30 days less snow coverage per winter season are projected to be located in mid-elevations (800 to 1300 m MSL). The largest relative decreases of 33 % less snow covered days per season are located in the lower elevations whereas the decrease is small in the highest

altitudes (-2%).
Snowmelt values are slightly increased in January and February, as well as during its maximum in May. Snowmelt is projected to decrease consistently from June to October. This leads to a decrease in runoff in early summer (June and July). The maximum in runoff is shifted from June to May, due to the shift in snowmelt amounts. From August to April, the expected increases in rainfall amounts cause small increases in mean monthly runoff. The absolute changes in seasonal snowmelt and runoff amounts are projected to remain relatively small. The frequency histogram of hourly discharge rates reveals a future intensification and accumulation of extreme runoff rates on both sides of the spectrum (low and high flow events) at the expense of mid-range river discharge rates.
Regarding impacts on the regional water balance components, there are some significant projected changes on the catchment scale. A mean rise in air temperature of $+0.94\ ^{\circ}C$ is accompanied by a slight increase in precipitation by +1.3 %. This increase in precipitation is valid only for rainfall (+6.1 %), whereas snowfall is projected to decrease significantly (-6.6 %). The decrease in snowfall amounts is elevation-dependent, ranging from nearly unaltered values in the peak regions (-2.4 %) to large decreases in the lowest elevations of up to -25.7 %. This change in precipitation characteristics is the main driver for the consequent changes in the regional hydrology. Snow cover duration decreases significantly (-19 d/year). Consequently, snowmelt amounts are projected to decrease by -8.2 %. Mean annual evapotranspiration is projected to increase by +2.4 %. Despite this finding, the mean annual runoff is projected to increase as well by +2.8 % due to the increases in rainfall amounts.

7.3 Future Research Demand and Potential

Modeling snow processes Regarding the fine scale snow cover evolution, some other processes still have not been taken into account so far, e.g. the interaction between snow and vegetation, particularly tree canopy. Interception, sublimation, melt unload, and changes in micrometeorology play a significant role in snow cover development beneath a canopy. Strasser *et al.* (2011) show the influence of tree canopy processes on snow cover development in the region. An interesting model-

ing enhancement would be the calculation of advective lateral exchange of sensible and latent heat between snow-covered and snow-free ground as that is known to be an important process for snowmelt timing in spring when the snow cover becomes patchy (Pohl & Marsh, 2006; Mott *et al.*, 2011a).
Another process which should be investigated and included into the presented models is the reflection of incoming solar radiation from steep slopes onto opposing hillsides. This effect is limited to narrow and steep terrain shapes but can can produce a multiplied radiative income for certain locations. This effect is particularly pronounced when the reflecting slopes are covered in snow and therefore have high albedos.
The introduced method to dynamically parameterize wind-driven snow redistribution is used in a very simple way and can be seen as a basis for further development. The field of the correction factor is implemented using one main winter wind-direction in this study. In general, it is a very open method, as the correction factor can be calculated for different wind direction sectors, and be dynamically changed every time-step or for a certain period of time, e.g. daily or monthly main wind-directions. Such an implementation strongly depends on the respective availability of information about the wind field. Depending on the study region and application such wind field information could be e.g. weather type classifications of atmospheric conditions, main wind-directions extracted from RCM data, or representative and transferable measurements. Another interesting extension of the method would be to use the wind correction factor field to modify the simulated turbulent fluxes. The computation of turbulent mass and energy fluxes strongly depends on the current wind speed. This wind speed could e.g. be scaled for each grid cell using the wind correction factors that are used for the correction of precipitation. Consequently, the sensible and latent fluxes are wind-adjusted according to the principle of the lateral snow redistribution procedure.

Potential of future observation and validation techniques Besides these specific ideas to enhance this work, future research must focus on measurement techniques to capture temporal dynamics of spatial snow cover distribution. Laser scan measurements - airborne or terrestrial - would be an ideal validation source for modeled snow accumulation and ablation processes (Prokop *et al.*, 2008; Prokop,

2008; Dadic *et al.*, 2010a,b; Grünewald *et al.*, 2010; Mott *et al.*, 2011b). Such data would be highly useful for validating this work. Another validation method would be measurements of stable isotopes in stored and flowing water compartments allowing to determine the contribution of snowmelt to total measured runoff.

Bibliography

Anderson, E. (1973). National Weather Service river forecast system–snow accumulation and ablation model. Technical Memorandum NWS HYDRO-17, Nov. 1973, 217pp.

Aronica, G., Bates, P. & Horritt, M. (2002). Assessing the uncertainty in distributed model predictions using observed binary pattern information within GLUE. *Hydrol. Processes* **16**, 2001–2016.

Bavay, M., Lehning, M., Jonas, T. & Löwe, H. (2009). Simulations of future snow cover and discharge in Alpine headwater catchments. *Hydrol. Processes* **23**, 95–108.

Berg, P., Wagner, S., Kunstmann, H. & Schädler, G. (2013). High resolution regional climate model simulations for Germany: part I – validation. *Clim. Dyn.* **40**, 401–414. 10.1007/s00382-012-1508-8.

Bernhardt, M., Liston, G. E., Strasser, U., Zängl, G. & Schulz, K. (2010). High resolution modelling of snow transport in complex terrain using downscaled MM5 wind fields. *The Cryosphere* **4**, 99–113.

Bernhardt, M. & Schulz, K. (2010). SnowSlide: A simple routine for calculating gravitational snow transport. *Geophys. Res. Lett.* **37**, L11502.

Bernhardt, M., Schulz, K., Liston, G. & Zängl, G. (2012). The influence of lateral snow redistribution processes on snow melt and sublimation in alpine regions. *J. Hydrol.* **424**, 196–206.

Blöschl, G. & Kirnbauer, R. (1992). An analysis of snow cover patterns in a small alpine catchment. *Hydrol. Processes* **6**, 99–109.

Braun, L. (1985). Simulation of snowmelt-runoff in lowland and lower alpine regions of Switzerland. Zürcher Geopgraphische Schriften, Heft 21, Geographisches Institut ETH Zürich, 166 pp.

CORRIPIO, J. (2003). Vectorial algebra algorithms for calculating terrain parameters from DEMs and solar radiation modelling in mountainous terrain. *Int. J. Geogr. Inf. Sci.* **17**, 1–23.

DADIC, R., CORRIPIO, J. & BURLANDO, P. (2008). Mass-balance estimates for Haut Glacier d'Arolla, Switzerland, from 2000 to 2006 using DEMs and distributed mass-balance modeling. *Ann. Glaciol.* **49**, 22–26.

DADIC, R., MOTT, R., LEHNING, M. & BURLANDO, P. (2010a). Parameterization for wind-induced preferential deposition of snow. *Hydrol. Processes* **24**, 1994–2006.

DADIC, R., MOTT, R., LEHNING, M. & BURLANDO, P. (2010b). Wind influence on snow depth distribution and accumulation over glaciers. *J. Geophys. Res.* **115**, F01012.

DOZIER, J. (1989). Spectral signature of alpine snow cover from the Landsat Thematic Mapper. *Remote Sens. Environ.* **28**, 9–22.

DUROT, K. (1999). Modélisation hydrologique distribuée du bassin versant nivo-pluvial de Sarennes. Validation des données d'entrée et développement d'un module de fonte nivale sous forêt. Ph.D. dissertation, Institut National Polytechnique de Grenoble, 332 pp.

ETCHEVERS, P., MARTIN, E., BROWN, R., FIERZ, C., LEJEUNE, Y., BAZILE, E., BOONE, A., DAI, Y., ESSERY, R., FERNANDEZ, A. *et al.* (2004). Validation of the energy budget of an alpine snowpack simulated by several snow models (SnowMIP project). *Ann. Glaciol.* **38**, 150–158.

FIERZ, C., RIBER, P., ADAMS, E., CURRAN, A., FOHN, P., LEHNING, M. & PLUSS, C. (2003). Evaluation of snow-surface energy balance models in alpine terrain. *J. Hydrol.* **282**, 76–94.

FISCHER, K. (2005). Geomorphologie der Berchtesgadener Alpen. Berchtesgaden Natl. Park Res. Rep. 50, Berchtesgaden. ISSN 0172-0023. ISBN 3-922325-35-X.

FRANZ, H., BAIER, R., GERECKE, R., GRAB, J., HOFMANN, G., HUBER, D., KONNERT, V., KRALLER, G., KUNSTMANN, H., KÜNZL, M., LOTZ, A., STRASSER, U., VOGEL, M. & WARSCHER, M. (2012). Global Change in Mountain Sites (GLOCHAMOST) - Coping strategies for Mountain Biosphere Reserves.

Implementing the GLOCHAMORE Research strategy into the Biosphere Reserve Berchtesgadener Land. Global change in Mountain Regions (GLOCHAMORE) a Project of the UNESCO's Man and Biosphere Programme. UNESCO, http://www.unesco.org/new/en/natural-sciences/environment/ecological-sciences/specific-ecosystems/mountains/glochamost.

GAREN, D. C. & MARKS, D. (2005). Spatially distributed energy balance snowmelt modelling in a mountainous river basin: estimation of meteorological inputs and verification of model results. *J. Hydrol.* **315**, 126–153.

GRUBER, S. (2007). A mass-conserving fast algorithm to parameterize gravitational transport and deposition using digital elevation models. *Water Resour. Res.* **43**, W06412.

GRÜNEWALD, T., SCHIRMER, M., MOTT, R. & LEHNING, M. (2010). Spatial and temporal variability of snow depth and ablation rates in a small mountain catchment. *The Cryosphere* **4**, 215–225.

GURTZ, J., ZAPPA, M., JASPER, K., LANG, H., VERBUNT, M., BADOUX, A. & VITVAR, T. (2003). A comparative study in modelling runoff and its components in two mountainous catchments. *Hydrol. Processes* **17**, 297–311.

HALL, D., RIGGS, G. & SALOMONSON, V. (1995). Development of methods for mapping global snow cover using moderate resolution imaging spectroradiometer data. *Remote Sens. Environ.* **54**, 127–140.

HOCK, R. (2003). Temperature index melt modelling in mountain areas. *J. Hydrol.* **282**, 104–115.

HUNTER, N., BATES, P., HORRITT, M., DE ROO, A., WERNER, M. *et al.* (2005). Utility of different data types for calibrating flood inundation models within a GLUE framework. *Hydrol. Earth Syst. Sci.* **9**, 412–430.

JASPER, K., CALANCA, P., GYALISTRAS, D. & FUHRER, J. (2004). Differential impacts of climate change on the hydrology of two alpine river basins. *Clim. Res.* **26**, 113–129.

KIRNBAUER, R., BLÖSCHL, G. & GUTKNECHT, D. (1994). Entering the era of distributed snow models. *Nord. Hydrol.* **25**, 1–24.

KLEMES, V. (1990). The modelling of mountain hydrology: the ultimate challenge. *IAHS Publ.* **190**, 29–43.

KOBIERSKA, F., JONAS, T., ZAPPA, M., BAVAY, M., MAGNUSSON, J. & BERNASCONI, S. (2013). Future runoff from a partly glacierized watershed in Central Switzerland: a two-model approach. *Adv. Water Resour.* **55**, 204–214.

KONNERT, V. (2004). Standortkarte Nationalpark Berchtesgaden. Natl. Park Res. Rep. 49, Berchtesgaden. ISSN 0172-0023. ISBN 978-3-922325-52-1.

KRALLER, G., STRASSER, U. & FRANZ, H. (2011). Effect of Alpine karst on the hydrology of the Berchtesgadener Ache basin: a comprehensive summary of karst research in the Berchtesgaden Alps. *eco.mont - Journal on Protected Mountain Areas Research* **3**, 19–28.

KRALLER, G., WARSCHER, M., KUNSTMANN, H., VOGL, S., MARKE, T. & STRASSER, U. (2012). Water balance estimation in high Alpine terrain by combining distributed modeling and a neural network approach (Berchtesgaden Alps, Germany). *Hydrol. Earth Syst. Sci.* **16**, 1969–1990.

KRAUSE, P., BOYLE, D. & BÄSE, F. (2005). Comparison of different efficiency criteria for hydrological model assessment. *Adv. Geosci.* **5**, 89–97.

KUCHMENT, L. & GELFAN, A. (1996). The determination of the snowmelt rate and the meltwater outflow from a snowpack for modelling river runoff generation. *J. Hydrol.* **179**, 23–36.

KUNSTMANN, H., KRAUSE, J. & MAYR, S. (2006). Inverse distributed hydrological modelling of Alpine catchments. *Hydrol. Earth Syst. Sci.* **10**, 395–412.

KUNSTMANN, H., SCHNEIDER, K., FORKEL, R. & KNOCHE, R. (2004). Impact analysis of climate change for an Alpine catchment using high resolution dynamic downscaling of ECHAM4 time slices. *Hydrol. Earth Syst. Sci.* **8**, 1031–1045.

KUNSTMANN, H. & STADLER, C. (2005). High resolution distributed atmospheric-hydrological modelling for Alpine catchments. *J. Hydrol.* **314**, 105–124.

KUNSTMANN, H., SUPPAN, P., HECKL, A. & RIMMER, A. (2007). Regional climate change in the middle east and impact on hydrology in the upper jordan catchment. In: *Proceedings of the Symposium Quantification and Reduction of*

Predictive Uncertainty for Sustainable Water Resources Management, Perugia, Italy, July 2007. IAHS Press.

LANGENSCHEIDT, E. (1981). Die Geologie zwischen Fagstein und Königssee in den Berchtesgadener Alpen. Unpublished Diploma Theses at the Philipps-University Marburg, Germany.

LAUX, P., VOGL, S., QIU, W., KNOCHE, H. R. & KUNSTMANN, H. (2011). Copula-based statistical refinement of precipitation in RCM simulations over complex terrain. *Hydrol. Earth Syst. Sci.* **15**, 2401–2419.

LEHNING, M., LÖWE, H., RYSER, M. & RADERSCHALL, N. (2008). Inhomogeneous precipitation distribution and snow transport in steep terrain. *Water Resour. Res.* **44**.

LEHNING, M., VÖLKSCH, I., GUSTAFSSON, D., NGUYEN, T., STÄHLI, M. & ZAPPA, M. (2006). ALPINE3D: a detailed model of mountain surface processes and its application to snow hydrology. *Hydrol. Processes* **20**, 2111–2128.

LI, H., SHEFFIELD, J. & WOOD, E. (2010). Bias correction of monthly precipitation and temperature fields from Intergovernmental Panel on Climate Change AR4 models using equidistant quantile mapping. *J. Geoph. Res.* **115**, D10.

LISTON, G. & ELDER, K. (2006). A distributed snow-evolution modeling system (SnowModel). *J. Hydrometeorol.* **7**, 1259–1276.

LISTON, G. & STURM, M. (1998). A snow-transport model for complex terrain. *J. Glaciol.* **44**, 498–516.

LOTZ, A. (2006). Alpine Habitat Diversity - HABITALP - Project Report 2002-2006. EU Community Initiative INTERREG III B Alpine Space Programme. Nationalpark Berchtesgaden.

MARKE, T., STRASSER, U., KRALLER, G., WARSCHER, M., KUNSTMANN, H., FRANZ, H. & VOGEL, M. (2013). The Berchtesgaden National Park (Bavaria, Germany): a platform for interdisciplinary catchment research. *Env. Earth Sci.* **69**, 679–694.

MARKS, D., DOMINGO, J., SUSONG, D., LINK, T. & GAREN, D. (1999). A spatially distributed energy balance snowmelt model for application in mountain basins. *Hydrol. Processes* **13**, 1935–1959.

MARSH, P. (1999). Snowcover formation and melt: recent advances and future prospects. *Hydrol. Processes* **13**, 2117–2134.

MARX, A., MAST, M., KNOCHE, R. & KUNSTMANN, H. (2008). Global climate change and regional impact on the water balance - Case study in the German alpine area. *Wasserwirtschaft* **98 (9)**, 12–16.

MOTT, R., EGLI, L., GRÜNEWALD, T., DAWES, N., MANES, C., BAVAY, M. & LEHNING, M. (2011a). Micrometeorological processes driving snow ablation in an Alpine catchment. *The Cryosphere* **5**, 1083–1098.

MOTT, R., FAURE, F., LEHNING, M., LOWE, H., HYNEK, B., MICHLMAYER, G., PROKOP, A. & SCHONER, W. (2008). Simulation of seasonal snow-cover distribution for glacierized sites on Sonnblick, Austria, with the Alpine3D model. *Ann. Glaciol.* **49**, 155–160.

MOTT, R., SCHIRMER, M., BAVAY, M., GRÜNEWALD, T. & LEHNING, M. (2010). Understanding snow-transport processes shaping the mountain snow-cover. *The Cryosphere* **4**, 545–559.

MOTT, R., SCHIRMER, M. & LEHNING, M. (2011b). Scaling properties of wind and snow depth distribution in an Alpine catchment. *J. Geophys. Res.* **116**, D6.

NAKIĆENOVIĆ, N., ALCAMO, J., DAVIS, G., DE VRIES, B., FENHANN, J., GAFFIN, S., GREGORY, K., GRÜBLER, A., JUNG, T., KRAM, T. *et al.* (2000). IPCC special report on emissions scenarios (SRES).

NASH, J. & SUTCLIFFE, J. (1970). River flow forecasting through conceptual models part I - a discussion of principles. *J. Hydrol.* **10**, 282–290.

OKE, T. (1987). *Boundary layer climates, 2nd Edition.* Routledge, London and New York.

PACHAURI, R. & REISINGER, A. (2007). Climate Change 2007: Synthesis Report. Contribution of Working Groups I, II and III to the Fourth Assessment Report of the Intergovernmental Panel on Climate Change. Intergovernmental Panel on Climate Change.

PENMAN, H. (1948). Natural evaporation from open water, bare soil and grass. *P. Roy. Soc. Lond. A Mat.* **193**, 120–145.

Pohl, S. & Marsh, P. (2006). Modelling the spatial–temporal variability of spring snowmelt in an arctic catchment. *Hydrol. Processes* **20**, 1773–1792.

Pomeroy, J., Gray, D., Shook, K., Toth, B., Essery, R., Pietroniro, A. & Hedstrom, N. (1998). An evaluation of snow accumulation and ablation processes for land surface modelling. *Hydrol. Processes* **12**, 2339–2367.

Prasch, M., Strasser, U. & Mauser, W. (2007). Validation of a physically based snow model for the simulation of the accumulation and ablation of snow (ESCIMO). Proceedings : AlpineSnowWorkshop, Berchtesgaden Natl. Park Res. Rep. 53, 78Ű-91. ISSN 0172-0023. ISBN 978-3-922325-60-4. EAN-Code 9783922325604.

Prokop, A. (2008). Assessing the applicability of terrestrial laser scanning for spatial snow depth measurements. *Cold Reg. Sci. Technol.* **54**, 155–163.

Prokop, A., Schirmer, M., Rub, M., Lehning, M. & Stocker, M. (2008). A comparison of measurement methods: terrestrial laser scanning, tachymetry and snow probing for the determination of the spatial snow-depth distribution on slopes. *Ann. Glaciol.* **49**, 210–216.

Raderschall, N., Lehning, M. & Schär, C. (2008). Fine-scale modeling of the boundary layer wind field over steep topography. *Water Resour. Res.* **44**, W09425.

Richards, L. (1931). Capillary conduction of liquids through porous mediums. *J. Appl. Phys.* **1**, 318–333.

Rigon, R., Bertoldi, G. & Over, T. (2006). GEOtop: A distributed hydrological model with coupled water and energy budgets. *J. Hydrometeorol.* **7**, 371–388.

Röckner, E., Bäuml, G., Bonaventura, L., Brokopf, R., Esch, M., Giorgetta, M., Hagemann, S., Kirchner, I., Kornblueh, L., Manzini, E., Rhodin, A., Schlese, U., Schulzweida, U. & Tompkins, A. (2003). The atmospheric general circulation model ECHAM 5. PART I: Model description. Technical report, MPImet/MAD Germany.

Rutter, N., Essery, R., Pomeroy, J., Altimir, N., Andreadis, K., Baker, I., Barr, A., Bartlett, P., Boone, A., Deng, H. *et al.* (2009). Evaluation of forest snow processes models (SnowMIP2). *J. Geophys. Res* **114**, D06111.

SCHULLA, J. & JASPER, K. (2007). Model Description WaSiM-ETH. Model Description WaSiM-ETH, Inst. for Atmos. and Clim. Sci., Swiss Fed. Inst. of Technol., Zürich.

SEVRUK, B. (1985). Systematischer Niederschlagsmessfehler in der Schweiz. *Geol. Schweiz Hydrol.* **31**, 65–75.

SIEBECK, O. (1982). Der Königssee - eine limnologische Projektstudie. Berchtesgaden National Park research report Nr. 5, Berchtesgaden. ISSN 0172-0023. ISBN 3-922325-04-1.

SKAMAROCK, W., KLEMP, J., DUDHIA, J., GILL, D. & BARKER, D. (2008). A description of the Advanced Research WRF version 3. NCAR Tech. Note NCAR/TN-475+ STR.

SMIATEK, G., KUNSTMANN, H. & HECKL, A. (2011). High-resolution climate change simulations for the Jordan River area. *J. Geoph. Res.* **116**, D16.

SMIATEK, G., KUNSTMANN, H., KNOCHE, R. & MARX, A. (2009). Precipitation and temperature statistics in high-resolution regional climate models: Evaluation for the European Alps. *J. Geoph. Res.* **114**, D19.

STMLU (2001). Nationalparkplan. Nationalpark Berchtesgaden. StMLU (Bayerisches Staatsministerium fü Landesentwicklung und Umweltfragen). http://www.nationalparkplan.de (2013-04-09).

STRASSER, U. (2008). Modelling of the mountain snow cover in the Berchtesgaden National Park. Berchtesgaden Natl. Park Res. Rep. 55, Berchtesgaden. ISSN 0172-0023. ISBN 978-3-922325-62-8. EAN-Code 9783922325628.

STRASSER, U., BERNHARDT, M., WEBER, M., LISTON, G. E. & MAUSER, W. (2008). Is snow sublimation important in the alpine water balance? *The Cryosphere* **2**, 53–66.

STRASSER, U., CORRIPIO, J., PELLICCIOTTI, F., BURLANDO, P., BROCK, B. & FUNK, M. (2004). Spatial and temporal variability of meteorological variables at Haut Glacier d'Arolla (Switzerland) during the ablation season 2001: measurements and simulations. *J. Geophys. Res* **109**, 10–1029.

STRASSER, U., ETCHEVERS, P. & LEJEUNE, Y. (2002). Inter-comparison of two

snow models with different complexity using data from an alpine site. *Nord. Hydrol.* **33**, 15–26.

STRASSER, U. & MARKE, T. (2010). ESCIMO.spread – a spreadsheet-based point snow surface energy balance model to calculate hourly snow water equivalent and melt rates for historical and changing climate conditions. *Geosci. Model Dev.* **3**, 643–652.

STRASSER, U. & MAUSER, W. (2001). Modelling the spatial and temporal variations of the water balance for the Weser catchment 1965-1994. *J. Hydrol.* **254**, 199–214.

STRASSER, U., WARSCHER, M. & LISTON, G. (2011). Modeling Snow Canopy Processes on an Idealized Mountain. *J. Hydrometeorol.* **12**, 663–677.

SUSONG, D., MARKS, D. & GAREN, D. (1999). Methods for developing time-series climate surfaces to drive topographically distributed energy- and water-balance models. *Hydrol. Processes* **13**, 2003–2021.

VAN GENUCHTEN, M. (1980). A closed-form equation for predicting the hydraulic conductivity of unsaturated soils. *Soil Sci. Soc. Am. J.* **44**, 892–898.

VERBUNT, M., GURTZ, J., JASPER, K., LANG, H., WARMERDAM, P. & ZAPPA, M. (2003). The hydrological role of snow and glaciers in alpine river basins and their distributed modeling. *J. Hydrol.* **282**, 36–55.

VOGL, S. & KUNSTMANN, H. (2013). Lokale Verfeinerung und Bias-Korrektur von regionalen Klimaszenarien. Abschlussbericht StMUG Projekt VH-ID: 32722/TUF01UF-32722.

WAGNER, S. (2008). Water balance in a poorly gauged basin in West Africa using atmospheric modelling and remote sensing information. Dissertation, Institut für Wasserbau der Universität Stuttgart.

WAGNER, S., BERG, P., SCHÄDLER, G. & KUNSTMANN, H. (2013). High resolution regional climate model simulations for Germany: Part II – projected climate changes. *Clim. Dyn.* **40**, 415–427. 10.1007/s00382-012-1510-1.

WARSCHER, M., STRASSER, U., KRALLER, G., MARKE, T., FRANZ, H. & KUNSTMANN, H. (2013). Performance of complex snow cover descriptions in a

distributed hydrological model system: A case study for the high alpine terrain of the berchtesgaden alps. *Water Resour. Res.* **49**, 2619–2637.

WEBER, M. (2008). Mikrometeorologische Prozesse bei der Ablation eines Alpengletschers. Verlag der Bayerischen Akademie der Wissenschaften.

WINSTRAL, A. & MARKS, D. (2002). Simulating wind fields and snow redistribution using terrain-based parameters to model snow accumulation and melt over a semi-arid mountain catchment. *Hydrol. Processes* **16**, 3585–3603.

ZAPPA, M., POS, F., STRASSER, U., WARMERDAM, P. & GURTZ, J. (2003). Seasonal Water Balance of an Alpine Catchment as Evaluated by Different Methods for Spatially Distributed Snowmelt Modelling. *Nord. Hydrol.* **34**, 179–202.

A

Appendix

A.1 C++ Source Code Energy Balance Calculation

In the following, excerpts from the modified C++ source code (snowmod.cc) of the WaSiM-ETH snow module describing the energy balance calculation are listed. This source code is part of the snow module (snowmod.cc) and uses grids of global radiation and cloudiness calculated in the evapotranspiration module (etpetr.cc). Some new runtime and output grids were defined e.g. for snow pack temperature (snotnpb50.grd) and snow surface temperature (surtnpb50.grd). Additionally, several new runtime variables were defined ($Ebal$, $Radflux$, $Sensflux$, $Latflux$, $Adflux$, $Soilflux$, $Mass\_lat$, $boltz\_clouds$, $LWin$, $LWout$, $SurfaceTemperature$, $SnowTemperature$, $AirTemperature$, $PresAir$, $PresSnow$, $AirPres$, $WindCorr$, $nr\_iterations$) and some constants were hard-coded (Boltzmann, specific heat capacities, etc.).

```
  // Initialize variables
  M=0.0;
  Mneg=0.0;
  Mass_lat=0.0;
  SnowTemperature = SNOWTEMP[i][j];
  AirTemperature=temperatur+273.16;
  Soilflux=2.0;
  RLF = gridinfo[getindex(_Luftfeuchte_)].pointer;
  U = gridinfo[getindex(_Windgeschwindigkeit_)].pointer;
  RGEX = gridinfo[getindex(_AspectCorrectedGlobalRadiation_)].pointer;
  CL = gridinfo[getindex(_Bewoelkungsgrad_)].pointer;
```

…

```
//new energy balance calculation
if (methode == 5 || methode == 6 || methode == 7 || methode == 11)

      {if (SSNOW[i][j] > 0.0)
      {
      if (SLIQ[i][j] > 0.0)
      {
      SurfaceTemperature = 273.16;
      SnowTemperature = 273.16;
      if (AirTemperature > 273.16)
      {
      PresAir = 6.1078 * exp((17.08085*(AirTemperature-
      273.16))/(234.175+(AirTemperature-273.16)))*RLF[i][j];
      }
      else
      {
      PresAir = 6.1071 * exp((22.4429*(AirTemperature-
      273.16))/(172.44+(AirTemperature-273.16)))*RLF[i][j];
      }
      PresSnow = 6.1071 * exp((22.4429*(SurfaceTemperature-
      273.16))/(172.44+(SurfaceTemperature-273.16)))*1.0;
      LWout= -0.0000000567*0.99*pow(SurfaceTemperature,4.0F);
      if (P[i][j] == 0.0) {
            boltz_clouds = 0.17;
            if (CL[i][j] <= 0.2) {boltz_clouds = 0.08;}
            if (CL[i][j] >= 0.6) {boltz_clouds = 0.20;}
      }
      else {boltz_clouds = 0.24;}
      LWin =
      0.0000000567*pow(AirTemperature,4.0F)*(0.610+0.050*pow(PresAir,0.5F))*(1
      .0+boltz_clouds*pow(CL[i][j],2.0F));
      Radflux=((1.0-Albedo[i][j])*RGEX[i][j]) + LWin + LWout ;
      Sensflux=18.85*(0.18+0.098*U[i][j])*(AirTemperature-SurfaceTemperature);
      Latflux=32.82*(0.18+0.098*U[i][j])*(PresAir-PresSnow);
      Adflux=((4180.0 * (AirTemperature-273.16)) *
      P_RAIN[i][j]/(InV*60.0))+((2100.0 * (AirTemperature-273.16)) *
      P_SNOW[i][j]/(InV*60.0));
      Ebal=Radflux+Sensflux+Latflux+Adflux+Soilflux;

      Mneg = -(Ebal*(InV*60.0))/337500.0;

      Mass_lat=(Latflux*(InV*60.0))/2835500.0;
```

```
SSNOW[i][j] = SSNOW[i][j] + Mass_lat;
SSTO[i][j] = SSNOW[i][j]+ SLIQ[i][j];

if (Mneg > 0.0)
{
if (Mneg <= SLIQ[i][j])
      {
  SLIQ[i][j] = SLIQ[i][j] - Mneg;
  SSNOW[i][j] = SSNOW[i][j] + Mneg;
      }
      else
      {
  SSNOW[i][j] += SLIQ[i][j];
SnowTemperature=SnowTemperature-((((Mneg-
SLIQ[i][j])*337500.0))/(SSNOW[i][j]*2100.0));

if (SSNOW[i][j] <= 3.0 && (AirTemperature - SnowTemperature) >= 5.0)
      {
        SnowTemperature=SurfaceTemperature;
      }
SLIQ[i][j] = 0
      }

SSTO[i][j] = SSNOW[i][j]+ SLIQ[i][j];
SURFTEMP[i][j] = SurfaceTemperature;
SNOWTEMP[i][j] = SnowTemperature;
if (SSTO[i][j] <= 0.0) {SNOWTEMP[i][j]=0.0;}
if (SSTO[i][j] <= 0.0) {SURFTEMP[i][j]=0.0;}
}
}


else
{
nr_iterations =0;
if (AirTemperature > 273.16)
{
PresAir = 6.1078 * exp((17.08085*(AirTemperature-
273.16))/(234.175+(AirTemperature-273.16)))*RLF[i][j];
}
else
{
PresAir = 6.1071 * exp((22.4429*(AirTemperature-
273.16))/(172.44+(AirTemperature-273.16)))*RLF[i][j];
}
      for (SurfaceTemperature=AirTemperature+2.0;
SurfaceTemperature>AirTemperature-13.0;
SurfaceTemperature=SurfaceTemperature-0.1) {
nr_iterations++;
LWout= -0.0000000567*0.99*pow(SurfaceTemperature,4.0F);
if (P[i][j] == 0.0) {
boltz_clouds = 0.17;
if (CL[i][j] <= 0.2) {boltz_clouds = 0.08;}
if (CL[i][j] >= 0.6) {boltz_clouds = 0.20;}
}
else {boltz_clouds = 0.24;}
```

```
LWin =
0.0000000567*pow(AirTemperature,4.0F)*(0.610+0.050*pow(PresAir,0.5F))*(1
.0+boltz_clouds*pow(CL[i][j],2.0F));
PresSnow = 6.1071 * exp((22.4429*(SurfaceTemperature-
273.16))/(172.44+(SurfaceTemperature-273.16)))*1.0;
Radflux=((1.0-Albedo[i][j])*RGEX[i][j]) + LWin + LWout ;
Sensflux=18.85*(0.18+0.098*U[i][j])*(AirTemperature-SurfaceTemperature);
Latflux=32.82*(0.18+0.098*U[i][j])*(PresAir-PresSnow);
Adflux=((4180.0 * (AirTemperature-273.16)) *
P_RAIN[i][j]/(InV*60.0))+((2100.0 * (AirTemperature-273.16)) *
P_SNOW[i][j]/(InV*60.0));
Ebal=Radflux+Sensflux+Latflux+Adflux+Soilflux;
if (Ebal > 0.0) {break;}
}
if (SurfaceTemperature > 273.16) {SurfaceTemperature = 273.16;}
Sensflux=18.85*(0.18+0.098*U[i][j])*(AirTemperature-SurfaceTemperature);
PresSnow = 6.1071 * exp((22.4429*(SurfaceTemperature-
273.16))/(172.44+(SurfaceTemperature-273.16)))*1.0;
Latflux=32.82*(0.18+0.098*U[i][j])*(PresAir-PresSnow);
Ebal=0.0;
if (nr_iterations >= 150)
      {
      SurfaceTemperature = AirTemperature;
      Sensflux = 0.0;
      if (AirTemperature > 273.16)
      {
PresAir = 6.1078 * exp((17.08085*(AirTemperature-
273.16))/(234.175+(AirTemperature-273.16)))*RLF[i][j];
      }
      else
      {
            PresAir = 6.1071 * exp((22.4429*(AirTemperature-
273.16))/(172.44+(AirTemperature-273.16)))*RLF[i][j];
      }
PresSnow = 6.1071 * exp((22.4429*(SurfaceTemperature-
273.16))/(172.44+(SurfaceTemperature-273.16)))*1.0;
      Latflux=32.82*(0.18+0.098*U[i][j])*(PresAir-PresSnow);
}
if (nr_iterations == 1 && SurfaceTemperature > 273.16)
      {
      SurfaceTemperature = 273.16;
            Sensflux=18.85*(0.18+0.098*U[i][j])*(AirTemperature-
SurfaceTemperature);
      if (AirTemperature > 273.16)
      {
PresAir = 6.1078 * exp((17.08085*(AirTemperature-
273.16))/(234.175+(AirTemperature-273.16)))*RLF[i][j];
      }
      else
      {
PresAir = 6.1071 * exp((22.4429*(AirTemperature-
273.16))/(172.44+(AirTemperature-273.16)))*RLF[i][j];
      }
PresSnow = 6.1071 * exp((22.4429*(SurfaceTemperature-
273.16))/(172.44+(SurfaceTemperature-273.16)))*1.0;
      Latflux=32.82*(0.18+0.098*U[i][j])*(PresAir-PresSnow);
}
if ((AirTemperature-SurfaceTemperature) > 3.0 )
```

```
      {
      SurfaceTemperature = AirTemperature -3.0;
      if (AirTemperature > 273.16)
            {
      PresAir = 6.1078 * exp((17.08085*(AirTemperature-
      273.16))/(234.175+(AirTemperature-273.16)))*RLF[i][j];
            }
            else
            {
      PresAir = 6.1071 * exp((22.4429*(AirTemperature-
      273.16))/(172.44+(AirTemperature-273.16)))*RLF[i][j];
            }
      PresSnow = 6.1071 * exp((22.4429*(SurfaceTemperature-
      273.16))/(172.44+(SurfaceTemperature-273.16)))*1.0;
      Latflux=32.82*(0.18+0.098*U[i][j])*(PresAir-PresSnow);
      }


      Mass_lat=(Latflux*(InV*60.0))/2835500.0;


      SSNOW[i][j] = SSNOW[i][j] + Mass_lat;
      SSTO[i][j] = SSNOW[i][j]+ SLIQ[i][j];
      SURFTEMP[i][j] = SurfaceTemperature;
      SNOWTEMP[i][j] = SnowTemperature;
      if (SSTO[i][j] <= 0.0) {SNOWTEMP[i][j]=0.0;}
      if (SSTO[i][j] <= 0.0) {SURFTEMP[i][j]=0.0;}
      }
      }
      }
  }
      else
      {


// CALCULATE MELT

if (methode == 5 || methode == 6 || methode == 7 || methode == 11)
          {
            SurfaceTemperature = 273.16;
            if (AirTemperature > 273.16)
            {
            PresAir = 6.1078 * exp((17.08085*(AirTemperature-
            273.16))/(234.175+(AirTemperature-273.16)))*RLF[i][j];
            }
            else
            {
            PresAir = 6.1071 * exp((22.4429*(AirTemperature-
            273.16))/(172.44+(AirTemperature-273.16)))*RLF[i][j];
            }
            PresSnow = 6.1071 * exp((22.4429*(SurfaceTemperature-
            273.16))/(172.44+(SurfaceTemperature-273.16)))*1.0;
            LWout= -0.0000000567*0.99*pow(SurfaceTemperature,4.0F);
            if (P[i][j] == 0.0) {
                  boltz_clouds = 0.17;
                  if (CL[i][j] <= 0.2) {boltz_clouds = 0.08;}
                  if (CL[i][j] >= 0.6) {boltz_clouds = 0.20;}
```

```
        }
        else {boltz_clouds = 0.24;}
                    LWin =
        0.0000000567*pow(AirTemperature,4.0F)*(0.610+0.050*pow(PresAir,0.5
        F))*(1.0+boltz_clouds*pow(CL[i][j],2.0F));
        Radflux=((1.0-Albedo[i][j])*RGEX[i][j]) + LWin + LWout;
        Sensflux=18.85*(0.18+0.098*U[i][j])*(AirTemperature-
        SurfaceTemperature);
        Latflux=32.82*(0.18+0.098*U[i][j])*(PresAir-PresSnow);
        Adflux=((4180.0 * (AirTemperature-273.16)) *
        P_RAIN[i][j]/(InV*60.0))+((2100.0 * (AirTemperature-273.16)) *
        P_SNOW[i][j]/(InV*60.0));
        Mass_lat=(Latflux*(InV*60.0))/2835500.0;
        SSNOW[i][j] = SSNOW[i][j] + Mass_lat;
        SSTO[i][j] = SSNOW[i][j]+ SLIQ[i][j];
        Ebal=Radflux+Sensflux+Latflux+Adflux+Soilflux;



        if (SLIQ[i][j] > 0.0)
        {
        SnowTemperature=SnowTemperature+(((SSNOW[i][j]/SSTO[i][j])*Ebal*(I
        nV*60.0))/(SSNOW[i][j]*2100.0))+(((SLIQ[i][j]/SSTO[i][j])*Ebal*(In
        V*60.0))/(SLIQ[i][j]*4180.0));
        }
        else
        {
        SnowTemperature=SnowTemperature+((Ebal*(InV*60.0))/(SSNOW[i][j]*21
        00.0));
        }
        if (SSTO[i][j] <= 3.0 && (AirTemperature - SnowTemperature) >=
        5.0)
        {
          SnowTemperature=SurfaceTemperature;
        }
        if (SnowTemperature > 273.16)
        {
          M=(SnowTemperature-273.16)*2100.0*SSNOW[i][j]/337500.0;
          SnowTemperature = 273.16;
        }


        SURFTEMP[i][j] = SurfaceTemperature;
        SNOWTEMP[i][j]=SnowTemperature;
        if (SSTO[i][j] <= 0.0) {SNOWTEMP[i][j]=0.0;}
        if (SSTO[i][j] <= 0.0) {SURFTEMP[i][j]=0.0;}
           }
              }
              }
              }
              }
return M * Anteil;
}
```

A.2 C++ Source Code Lateral, Gravitational Snow Transport

Excerpts from the modified C++ source code of the WaSiM-ETH snow module describing lateral, gravitational snow transport are shown below. In principle, it is a 4-neighbor-routing routine. The program uses preprocessed input grids for the flow fractions of the 4 neighboring cells (sld1npb50.grd, sld2npb50.grd, sld3npb50.grd, sld4npb50.grd), a grid for maximum deposition (depmnpb50.grd), and two grids for describing the elevation order in row and column coordinates (elornpb50.grd, elocnpb50.grd). The computation of these grids is done using the code in appendix A.4. Additionally, three runtime and output grids are defined for input mass (inmanpb50.grd), mobile mass (momanpb50.grd), and depostion (deponpb50.grd).

```
if (methode > 5 && methode < 10)

{
float Flow1, Flow2, Flow3, Flow4, liq, liq1, liq2, liq3, liq4;
int row, col;

SL = gridinfo[getindex(_Gefaelle_)].pointer;

for (i=1;i<=nrows;i++)
  {

      for (j=FirstLastCol[i].First;j<=FirstLastCol[i].Last;j++)
    {
      if (zn[i][j]!=nodata)
{
  DEPOSITION[i][j]=0.0;
  INPUT_MASS[i][j]=0.0;
  MOBILE_MASS[i][j]=0.0;
}
}
}
 for (i=nrows;i>=1;i--)
  {
      for (j=FirstLastCol[i].First;j<=FirstLastCol[i].Last;j++)
    {
      if (zn[i][j]!=nodata)
{
  row = ELEV_ORDER_ROW[i][j];
  col = ELEV_ORDER_COLUMN[i][j];

if (SSTO[row][col] > 0.0)
      {
      if (SL[row][col] >= 45.0)
      {
      INPUT_MASS[row][col]=(0.01*SSTO[row][col])+MOBILE_MASS[row][col];
      liq = SLIQ[row][col]/SSTO[row][col];
      SSTO[row][col] =  SSTO[row][col] - (0.01*SSTO[row][col]);
      SLIQ[row][col] = liq * SSTO[row][col];
      SSNOW[row][col]= SSTO[row][col] - SLIQ[row][col];
      }
      else {
      INPUT_MASS[row][col]=MOBILE_MASS[row][col];
      }
}
else {
INPUT_MASS[row][col]=MOBILE_MASS[row][col];
}


  Flow1 = SLIDEFRACTION1[row][col] * INPUT_MASS[row][col];
  Flow2 = SLIDEFRACTION2[row][col] * INPUT_MASS[row][col];
  Flow3 = SLIDEFRACTION3[row][col] * INPUT_MASS[row][col];
  Flow4 = SLIDEFRACTION4[row][col] * INPUT_MASS[row][col];


 if (DEPOSITION[row-1][col] + Flow1 <= DEPOSITION_MAX[row-1][col])
      {DEPOSITION[row-1][col] = DEPOSITION[row-1][col] + Flow1;
      }
```

```
  else      { MOBILE_MASS[row-1][col] = MOBILE_MASS[row-1][col] + Flow1 +
      DEPOSITION[row-1][col] - DEPOSITION_MAX[row-1][col];
        DEPOSITION[row-1][col] = DEPOSITION_MAX[row-1][col];
         }

 if (DEPOSITION[row][col-1] + Flow2 <= DEPOSITION_MAX[row][col-1])
      {DEPOSITION[row][col-1] = DEPOSITION[row][col-1] + Flow2;
      }
  else      {  MOBILE_MASS[row][col-1] = MOBILE_MASS[row][col-1] + Flow2 +
      DEPOSITION[row][col-1] - DEPOSITION_MAX[row][col-1];
      DEPOSITION[row][col-1] = DEPOSITION_MAX[row][col-1];
      }
 if (DEPOSITION[row+1][col] + Flow3 <= DEPOSITION_MAX[row+1][col])
      {DEPOSITION[row+1][col] = DEPOSITION[row+1][col] + Flow3;
      }
  else      { MOBILE_MASS[row+1][col] = MOBILE_MASS[row+1][col] + Flow3 +
      DEPOSITION[row+1][col] - DEPOSITION_MAX[row+1][col];
      DEPOSITION[row+1][col] = DEPOSITION_MAX[row+1][col];
      }
 if (DEPOSITION[row][col+1] + Flow4 <= DEPOSITION_MAX[row][col+1])
      {DEPOSITION[row][col+1] = DEPOSITION[row][col+1] + Flow4;
      }
  else      { MOBILE_MASS[row][col+1] = MOBILE_MASS[row][col+1] + Flow4 +
      DEPOSITION[row][col+1] - DEPOSITION_MAX[row][col+1];
      DEPOSITION[row][col+1] = DEPOSITION_MAX[row][col+1];
      }
      }
      }
      }


for (i=1;i<=nrows;i++)
  {
      for (j=FirstLastCol[i].First;j<=FirstLastCol[i].Last;j++)
    {
      if (zn[i][j]!=nodata)
      {
  if (SSTO[i][j] > 0.0 )
      {
  liq = SLIQ[i][j]/SSTO[i][j];
  SSTO[i][j] =  SSTO[i][j] + DEPOSITION[i][j];
  SLIQ[i][j] = liq * SSTO[i][j];
  SSNOW[i][j]= SSTO[i][j] - SLIQ[i][j];
      }
else
{ SSTO[i][j] = 0.0;
  SSTO[i][j] =  SSTO[i][j] + DEPOSITION[i][j];
  SLIQ[i][j] = 0.0;
  SSNOW[i][j]= SSTO[i][j];

}
}
}
}
}
```

A.3 C++ Source Code Lateral, Wind-driven Snow Redistribution

The following sections shows excerpts from the modified C++ source code of the WaSiM-ETH snow module describing lateral, wind-driven snow redistribution. It uses a preprocessed input grid with a deposition factor (depx.npb50.grd) and corrects the internal field of snow precipitation. The source code for the computation of the input grid is presented in appendix A.5.

```
// Correction wind redistribution
if (methode == 7 || methode == 9 || methode == 10 || methode == 11)
{
      DEPOINDEX = gridinfo[getindex(_depoindex_)].pointer;
      P[i][j] += (DEPOINDEX[i][j]*P_SNOW[i][j]);
      P_SNOW[i][j] = P_SNOW[i][j] + (DEPOINDEX[i][j]*P_SNOW[i][j]);
}
```

A.4 IDL Preprocessing Source Code Gravitational Transport

Below, the IDL preprocessing source code for calculating input grids for the simulation of gravitational transport is appended. It uses the digital elevation model and the grid for slope that is produced by the WaSiM-ETH preprocessing tool "Tanalys". The program calculates grids for the flow fractions of the 4 neighboring cells (sld1npb50.grd, sld2npb50.grd, sld3npb50.grd, sld4npb50.grd), a grid for maximum deposition (depmnpb50.grd), and two grids for describing the elevation rank of each pixel in row and column coordinates (elornpb50.grd, elocnpb50.grd).

```
pro snowslides

COMMON variables

;PREPROCESSING FOR GRAVITATIONAL SLIDES
;calculation of grids (FLOWFRACTION 1 - 4, ELEVATION_ORDER,MAXIMUM_DEPOSITION)

;read aspect and slope (calculated by TANALYS)
asp = REVERSE(READ_BINARY(input+'npb50.exp', DATA_DIMS=[900,900], DATA_TYPE=4,
DATA_START=48),2)
slp = REVERSE(READ_BINARY(input+'npb50.slp', DATA_DIMS=[900,900], DATA_TYPE=4,
DATA_START=48),2)

;set NaNs
dem_corr = dem
dem_corr(where(ezg EQ -9999))= 'NaN'


;-------------------------------------------------------------------------------
;calculate flow widths (GRUBER 2007)
L1 = cos(asp*!dtor)*resolution
L2 = -sin(asp*!dtor)*resolution
L3 = sin(asp*!dtor)*resolution
L4 = -cos(asp*!dtor)*resolution

;calculate height differences to 4 neighbouring cells
delta_z_1 = FLTARR(900,900)
delta_z_2 = FLTARR(900,900)
delta_z_3 = FLTARR(900,900)
delta_z_4 = FLTARR(900,900)

FOR i=0L, 899 DO BEGIN
 FOR j=0L, 898 DO BEGIN
  delta_z_1[i,j]=dem_corr[i,j]-dem_corr[i,j+1]
  ENDFOR
ENDFOR

FOR i=1L, 899 DO BEGIN
 FOR j=0L, 899 DO BEGIN
  delta_z_2[i,j]=dem_corr[i,j]-dem_corr[i-1,j]
  ENDFOR
ENDFOR

FOR i=0L, 899 DO BEGIN
 FOR j=1L, 899 DO BEGIN
  delta_z_3[i,j]=dem_corr[i,j]-dem_corr[i,j-1]
  ENDFOR
ENDFOR

FOR i=0L, 898 DO BEGIN
 FOR j=0L, 899 DO BEGIN
  delta_z_4[i,j]=dem_corr[i,j]-dem_corr[i+1,j]
  ENDFOR
ENDFOR

;set flow widths to zero where neighbouring cell is higher than actual cell
(no upward flow)
L1_corr=L1
```

```
L1_corr(where(delta_z_1 LE 0))=0
L1_corr(where(L1 LE 0))=0
L2_corr=L2
L2_corr(where(delta_z_2 LE 0))=0
L2_corr(where(L2 LE 0))=0
L3_corr=L3
L3_corr(where(delta_z_3 LE 0))=0
L3_corr(where(L3 LE 0))=0
L4_corr=L4
L4_corr(where(delta_z_4 LE 0))=0
L4_corr(where(L4 LE 0))=0

;calculate flow fractions (normalized flow widths)
L_sum = L1_corr + L2_corr + L3_corr + L4_corr

f1 = FLTARR(900,900)
f2 = FLTARR(900,900)
f3 = FLTARR(900,900)
f4 = FLTARR(900,900)

FOR i=0L, 899 DO BEGIN
 FOR j=0L, 899 DO BEGIN
  IF (L_sum[i,j] NE 0) THEN BEGIN
    f1[i,j]=L1_corr[i,j]/L_sum[i,j]
  ENDIF
  ENDFOR
ENDFOR
FOR i=0L, 899 DO BEGIN
 FOR j=0L, 899 DO BEGIN
  IF (L_sum[i,j] NE 0) THEN BEGIN
    f2[i,j]=L2_corr[i,j]/L_sum[i,j]
  ENDIF
  ENDFOR
ENDFOR
FOR i=0L, 899 DO BEGIN
 FOR j=0L, 899 DO BEGIN
  IF (L_sum[i,j] NE 0) THEN BEGIN
    f3[i,j]=L3_corr[i,j]/L_sum[i,j]
  ENDIF
  ENDFOR
ENDFOR
FOR i=0L, 899 DO BEGIN
 FOR j=0L, 899 DO BEGIN
  IF (L_sum[i,j] NE 0) THEN BEGIN
    f4[i,j]=L4_corr[i,j]/L_sum[i,j]
  ENDIF
  ENDFOR
ENDFOR

f1(where(ezg EQ -9999))=-9999
f2(where(ezg EQ -9999))=-9999
f3(where(ezg EQ -9999))=-9999
f4(where(ezg EQ -9999))=-9999

f1_rev=REVERSE(f1,2)
f2_rev=REVERSE(f2,2)
f3_rev=REVERSE(f3,2)
f4_rev=REVERSE(f4,2)
```

```
iimage, f1_rev
iimage, f2_rev
iimage, f3_rev
iimage, f4_rev


;-------------------------------------------------------------------------
;calculation of elevation orders (new grids with x and y values for pixel rank
regarding elevation)
dem_scan=dem
dem_scan(where(ezg EQ -9999)) = -9999
dummy=dem_scan(where(dem_scan NE -9999, count))
length=SIZE(dem_scan, /DIMENSIONS)
nr_pixels=length(0)*length(1)
index_column = FLTARR(length(0),length(1))
index_row= FLTARR(length(0),length(1))
list_coord_ezg = FLTARR(2,count)
k=0L

FOR j=0L, length(0)-1 DO BEGIN
FOR i=0L, length(1)-1 DO BEGIN

IF (dem_scan[i,j] NE -9999) THEN BEGIN
  list_coord_ezg[0,k] = i
  list_coord_ezg[1,k] = j
  k++
ENDIF

ENDFOR
ENDFOR

k=0L

FOR i=0L, count-1 DO BEGIN
x = where(dem_scan EQ max(dem_scan))
index_column[list_coord_ezg[0,k],length(0)-list_coord_ezg[1,k]-1] = (x(0) mod
length(0))+1
index_row[list_coord_ezg[0,k],length(1)-list_coord_ezg[1,k]-1] = length(1)-
(x(0)/length(1))
dem_scan[x(0) mod length(0),x(0)/length(1)]=0
k++
ENDFOR

iimage, index_column, VIEW_TITLE='columns'
iimage, index_row, VIEW_TITLE='rows'


;-------------------------------------------------------------------------
;calculation of grid for maximum possible deposition depending on slope
i_lim=55
D_lim=FLTARR(900,900)
D_lim[0:899,0:899]=1
D_max=FLTARR(900,900)
D_max[0:899,0:899]=1

slp(where(slp EQ -9999)) = 'NaN'
D_max=(1-(slp/i_lim))*D_lim
D_max(where(slp GE i_lim)) = 0
```

```
D_max(where(ezg EQ -9999)) = 'NaN'
D_max_rev=REVERSE(D_max,2)

iimage, D_max_rev

END
```

A.5 IDL Preprocessing Source Code Wind-driven Snow Redistribution

In the following, the IDL preprocessing source code for calculating the input grid for the simulation of wind-driven snow redistribution is shown. The code uses the digital elevation model and grids for slope and aspect that are produced by the WaSiM-ETH preprocessing tool "Tanalys".

```
pro windredistribution

COMMON variables

fromAngle=180.0
toAngle=270.0

FOR windDirNum = 0, numWindDirections - 1 DO BEGIN
  fromAngle = windDirections[0, windDirNum]

;Convert common used starting angle (0°=N, 90°=E,...) to an "internal angle"
IF fromAngle LT 180 THEN toAngleIntern = 180 - fromAngle ELSE toAngleIntern
= 540 - fromAngle
toAngle = windDirections[1, windDirNum]

  ;Convert common used ending angle (0°=N, 90°=E,...) to an "internal angle"
IF toAngle LE 180 THEN fromAngleIntern = 180 - toAngle ELSE fromAngleIntern
= 540 - toAngle
IF fromAngleIntern GT toAngleIntern THEN fromAngleIntern -= 360

anglesStr = STRING(fromAngle, '(I03)') + '-' + STRING(toAngle, '(I03)')
windCorrFile = imagesPath + 'WindCorr_' + anglesStr + '_' + domain + '_' +
STRTRIM(resolution, 2) + '.asc'

IF FILE_TEST(windCorrFile) THEN BEGIN
PRINT, 'Reading snow redistribution field for wind direction ' +
STRTRIM(fromAngle, 2) + '-' + STRTRIM(toAngle, 2) + '...'
struct = READ_ASCII_GRID(windCorrFile, /NaN)
windCorrField = REVERSE(struct.data, 2)
ENDIF ELSE BEGIN
PRINT, 'Calculating snow redistribution field for wind direction ' +
STRTRIM(fromAngle, 2) + '-' + STRTRIM(toAngle, 2) + '...'

;Use of "internal angle" to calculate factor field
azimStep = 1. > ((toAngleIntern - fromAngleIntern) / 10.) < 10. ;azimstep
between 1 and 10 degrees
svf = Calculate_Sky_View_Factor(dtm, resolution, MINAZIM = fromAngleIntern,
MAXAZIM = toAngleIntern, AZIMSTEP = azimStep)
ENDELSE
ENDFOR

svf=svf/max(svf)
dem_corr=dem/max(dem)
windcorr=dem_corr*(3.5*svf-1)+0.1

iimage, windcorr

end
```

```
;Uses a hillshading algorithm to compute skyview factor at regular azimuth and
elevation intervals
;Javier Corripio. May, 2000, modified November, 2001
;IDL version: Florian Hanzer, Feb 2010
;Florian Hanzer, Jul 2010: replace no-data pixels with the mean DTM height
while calculating the SVF

FUNCTION Calculate_Sky_View_Factor, dtm, dl, ELEVSTEP = elevStep, AZIMSTEP =
azimStep, MINAZIM = minAzim, MAXAZIM = maxAzim

IF N_ELEMENTS(elevStep) EQ 0 THEN elevStep = -1 ;Elevation interval
IF N_ELEMENTS(azimStep) EQ 0 THEN azimStep = 10 ;Azimuth interval
IF N_ELEMENTS(minAzim)  EQ 0 THEN minAzim  = 0
IF N_ELEMENTS(maxAzim)  EQ 0 THEN maxAzim  = 360 - azimStep

z = dtm
dims = SIZE(dtm, /DIMENSIONS)
cols = dims[0]
rows = dims[1]

;Set no-data pixels to the mean DTM height
noDataPixels = WHERE(~FINITE(z), noDataCount)
IF noDataCount GT 0 THEN z[noDataPixels] = MEAN(z[WHERE(FINITE(z))])

PRINT, 'Azimuth interval is ' + STRTRIM(azimStep, 2) + ', elevation interval
is ' + STRTRIM(elevStep, 2)

CellGradient    = DBLARR(cols, rows, 3)
NodeGradient    = DBLARR(cols, rows, 3)
area            = DBLARR(cols, rows)
SkyViewCell     = DBLARR(cols, rows)
skvFactor       = DBLARR(cols, rows)
SunVector       = DBLARR(3)

;Normal vector:
CellGradient[    *,        *,    *] = 1.
CellGradient[0:cols-2, 0:rows-2, 0] = .5 * dl * (z[0:cols-2, 0:rows-2] +
z[0:cols-2, 1:rows-1] - z[1:cols-1, 0:rows-2] - z[1:cols-1, 1:rows-1])
CellGradient[0:cols-2, 0:rows-2, 1] = .5 * dl * (z[0:cols-2, 0:rows-2] -
z[0:cols-2, 1:rows-1] + z[1:cols-1, 0:rows-2] - z[1:cols-1, 1:rows-1])
CellGradient[    *,        *,    2] = dl^2.

NodeGradient[*, *, *] = 1.
FOR i = 0, 2 DO NodeGradient [1:cols-1, 1:rows-1, i] = $
                (CellGradient[1:cols-1, 1:rows-1, i] + $
                 CellGradient[0:cols-2, 0:rows-2, i] + $
                 CellGradient[0:cols-2, 1:rows-1, i] + $
                 CellGradient[1:cols-1, 0:rows-2, i]   $
                ) / 4.
area[*, *] = SQRT(NodeGradient[*, *, 0]^2. + NodeGradient[*, *, 1]^2. +
NodeGradient[*, *, 2]^2.)
FOR i = 0, 2 DO NodeGradient[*, *, i] /= area[*, *]

maxSlope = FIX(ACOS(MIN(NodeGradient[1:cols-3, 1:rows-3, 2])) / !DTOR)
PRINT, 'Maximum slope is ' + STRTRIM(maxslope, 2)

;Scanning at azimuth intervals from 0 to max slope
SkyViewCell[*, *] = 0.
```

```
FOR azim = minAzim, maxAzim, azimStep DO BEGIN
  skvFactor[*, *] = maxSlope
  azimuth = azim * !DTOR

  FOR elev = maxSlope, 1, elevstep DO BEGIN
    elevation = elev * !DTOR
    PRINT, 'Computing sky visibility from ' + STRTRIM(azim, 2) + ' azimuth, '
   + STRTRIM(elev, 2) + ' elevation'

    SunVector[0] = SIN(azimuth) * COS(elevation)
    SunVector[1] = -COS(azimuth) * COS(elevation)
    SunVector[2] = SIN(elevation)

    shadowField = CALCULATE_SHADOWS(z, SunVector, dl)
    pos = WHERE(shadowField EQ 1, count)
    IF count GT 0 THEN skvFactor[pos] = elev
  ENDFOR

  ;Next gives the sum of minimum visibility angles (degs) for all scanning
  ;Directions. Needs to be averaged according to number of azimuth steps
  skvFactor = COS(skvFactor * !DTOR)^2. * azimStep / 360.
  SkyViewCell = SkyViewCell + skvFactor
ENDFOR

;Correct first/last two rows/colums
SkyViewCell[   0,         *   ] = SkyViewCell[   2,         *   ]
SkyViewCell[   1,         *   ] = SkyViewCell[   2,         *   ]
SkyViewCell[cols - 2,     *   ] = SkyViewCell[cols - 3,     *   ]
SkyViewCell[cols - 1,     *   ] = SkyViewCell[cols - 3,     *   ]
SkyViewCell[   *,         0   ] = SkyViewCell[   *,         2   ]
SkyViewCell[   *,         1   ] = SkyViewCell[   *,         2   ]
SkyViewCell[   *,     rows - 2] = SkyViewCell[   *,     rows - 3]
SkyViewCell[   *,     rows - 1] = SkyViewCell[   *,     rows - 3]

;Write no-data values where they were before:
IF noDataCount GT 0 THEN SkyViewCell[noDataPixels] = !VALUES.F_NAN

RETURN, SkyViewCell

END
```